

---

Nucleation of calcium silicate hydrate in aqueous solution and  
the influence of biomolecules on cement hydration.

---

**Dissertation**

Erlangung des akademischen Grades  
,Doktor der Naturwissenschaften‘

am Fachbereich Chemie,  
Pharmazie und Geowissenschaften der

Johannes Gutenberg-Universität Mainz



**Nina Krautwurst**  
geboren in Mainz

Mainz, Juni 2017

Dekanin: Prof. Dr. Angelika Kühnle

Gutachter/in: 1. Prof. Dr. Wolfgang Tremel

2. Priv. Doz. Ute Kolb

3. Prof. Dr. Karl W. Klinkhammer

## **Declaration**

Hereby, I declare that I have composed this work on my own and using exclusively the quote references and resources. Literally or correspondingly adapted material has been marked accordingly.

## **Erklärung**

Hiermit erkläre ich, dass ich die vorliegende Arbeit selbstständig und nur mit den angegebenen Quellen und Hilfsmitteln angefertigt habe. Wörtlich oder sinngemäß übernommenes Gedankengut habe ich als solches kenntlich gemacht.

---

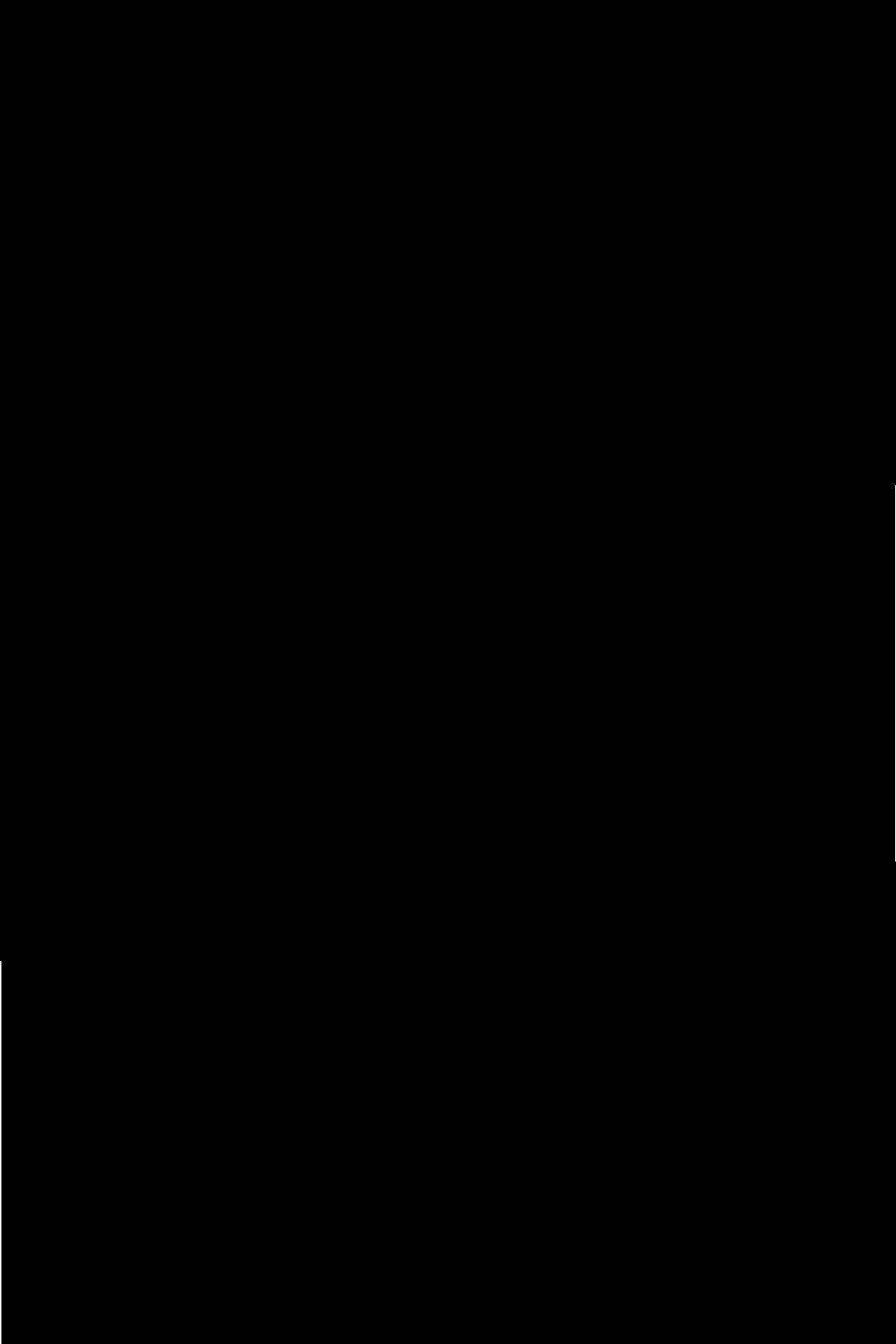
Ort, Datum

---

Nina Krautwurst

*To my family.*

Preface/Acknowledgement



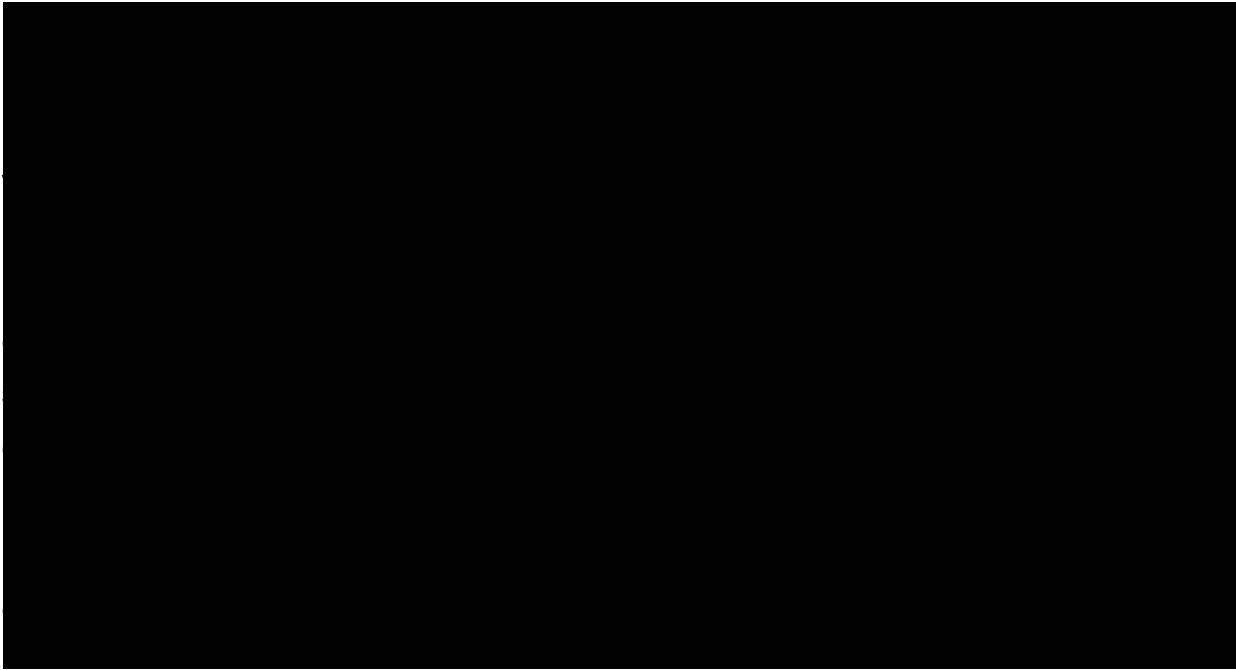


# Table of Contents

<b>1</b>	<b>List of abbreviations</b> .....	<b>13</b>
<b>2</b>	<b>General background</b> .....	<b>15</b>
2.1	Introduction and scope .....	16
2.2	Classical and non-classical crystallization .....	20
2.2.1	Classical nucleation theory .....	20
2.2.2	Two-step nucleation .....	22
2.2.3	Heterogeneous nucleation .....	24
2.2.4	Experimental methods .....	25
2.3	Biosilification .....	27
2.4	Fundamentals of cement chemistry .....	29
2.4.1	The different mineral phases of ordinary portland cement .....	29
2.4.2	The hydration of ordinary portland cement .....	31
2.4.3	The nanostructure of C-S-H .....	33
2.4.4	Accelerating admixtures .....	37
2.4.5	Optimum sulphate level .....	37
2.4.6	Biocement .....	38
2.5	Potentiometric measurement .....	40
2.5.1	Potentiometry .....	40
2.5.2	Ion-sensitive electrode .....	42
2.6	Turbidity measurement .....	43
<b>3</b>	<b>Nucleation of C-S-H and the impact of polymers</b> .....	<b>46</b>
3.1	Nucleation of C-S-H .....	47
3.1.1	Objectives .....	47
3.1.2	Results and Discussion .....	49
3.1.3	Conclusion and outlook .....	57
3.2	Influence of polymers .....	63
3.2.1	Objectives .....	63
3.2.2	Data evaluation .....	64
3.2.3	Results and discussion .....	65
3.2.4	Conclusion .....	74
<b>4</b>	<b>Influence of biomolecules on cement hydration</b> .....	<b>75</b>
4.1	Enzyme screening .....	76
4.1.1	Objectives .....	76
4.1.2	Results and discussion .....	77
4.1.3	Conclusion and outlook .....	81
4.2	The effect of the cysteine protease papain .....	83

4.2.1	Objectives .....	83
4.2.2	Results and discussion .....	84
4.2.3	Conclusion and outlook.....	90
<b>5</b>	<b>Conclusion and Outlook .....</b>	<b>92</b>
<b>6</b>	<b>Authors contributions.....</b>	<b>95</b>
<b>7</b>	<b>Appendix.....</b>	<b>96</b>
<b>8</b>	<b>References.....</b>	<b>120</b>
<b>9</b>	<b>List of Figures .....</b>	<b>124</b>
<b>10</b>	<b>List of Tables.....</b>	<b>128</b>



## Summary

The present work studied the formation of calcium silicate hydrate (C-S-H), the main binding phase of hydrated cement, to provide a deeper understanding of the underlying mechanisms, which are mostly unexplored.

In the first part of the thesis, the C-S-H precipitation from homogeneous solution conditions was investigated using time-resolved potentiometry and turbidimetry combined with dynamic light scattering, small angle X-ray scattering with synchrotron radiation and cryo-TEM. The results in the present work showed that C-S-H formation proceeds *via* a complex two-step pathway under these conditions. In the first step, amorphous and dispersed spheroids are formed, whose composition is depleted in calcium compared to  $\beta$ -C-S-H and also charge compensated with sodium. In the second step these amorphous spheroids crystallize to form a tobermorite-type  $\beta$ -C-S-H. This crystallization is accompanied by a sodium/calcium cation exchange and an aggregation.

The impact of cationic polymers of different charge densities was additionally investigated in the same experimental setup. With increasing positive charge density, a strong stabilizing effect on the primary nucleated particles was observed, which resulted in a second nucleation point during the nucleation process. The stabilizing effect of the first formed species examined in presence of the highly charged copolymers in this study can be explained by the exchange of calcium ions against the polymer as counterions. For a given pH, there is a considerable change in surface charge density where the valence of the counterions and thus the effect of the polymers decrease.

The second part of the thesis addresses the influence of certain biomolecules on the cement hydration process. As biomolecules, proteins with silica activity were analysed with focus on their potential of accelerating silicate/C-S-H formation under conditions as in the cement environment, with an extremely basic pH and high salinity on a laboratory level. The hydration of ordinary Portland cement was analysed *via* isothermal calorimetry (IC). In a large enzyme screening, among the various serine and cysteine proteases analysed, papain was the only additive that caused a small accelerating effect on the hydration process. In contrast, the protease bromelain had a retarding effect on the hydration process. The active site residue of papain was blocked and the effect of the modified enzyme was observed. After the inhibition of the papain, a decrease in the protease activity of the papain was observed *via* the coomassie assay. The coomassie blue dye binding was used to determine

the protease activity of the active and inactivated papain. *Via* IC, the accelerating effect of papain after inhibition decreased in contrast to the effect of the active enzyme. This is a strong indication that the active side residue is involved and furthermore responsible and important for the accelerating effect on the hydration process.

## Zusammenfassung

Die vorliegende Arbeit untersucht die Bildung von Calcium-Silikat-Hydraten (C-S-H), die Hauptbindephasen in Zement, um ein besseres Verständnis der zugrundeliegenden Mechanismen zu erzielen, die bislang zum Großteil unerforscht sind.

Im ersten Teil der Arbeit wurde die C-S-H Fällung aus einem homogenen Lösungszustand mittels zeitaufgelöster Potentiometrie und Turbidimetrie, kombiniert mit dynamischer Lichtstreuung, Röntgenstreuung sowie cryo-Transmissionselektronenmikroskopie untersucht. Es konnte gezeigt werden, dass die Bildung von C-S-H über einen komplexen zwei-Stufen-Prozess abläuft. In einem ersten Schritt bildet sich eine gelöste, amorphe Zwischenstufe, deren Zusammensetzung in Calcium verarmt ist verglichen mit der finalen  $\beta$ -C-S-H Phase. Ausgeglichen wird die Ladungsbilanz durch Ergänzung an Natrium Ionen in der Struktur. In einem zweiten Schritt kristallisiert diese amorphe Zwischenstufe zur der dem Tobermorite ähnlichen  $\beta$ -C-S-H Phase. Während der Kristallisation und Aggregation findet ein Austausch der Natrium Ionen gegen Calcium Ionen statt.

Der Einfluss kationischer polymer verschiedener Oberflächenladung wurde im selben experimentellen Aufbau untersucht. Mit steigender positiver Ladung wurde eine Stabilisierung der ersten gebildeten Zwischenstufen während des Nukleationsprozesses festgestellt. Hieraus resultierte ein zweites Nukleationsevent zu späterem Zeitpunkt. Abhängig vom pH-Wert variiert die Oberflächenbeladung der gebildeten Calcium-Silikat-Hydrat-Phase und in Folge dessen der Einfluss der kationischen polymere auf die Stabilisierung der Zwischenstufe.

Der zweite Teil der Arbeit befasst sich mit dem Einfluss verschiedener Bioadditive auf den Zementhydratationsprozess. Als Bioadditive wurde Proteinen mit Silikat-Aktivität, wie Silicatein, analysiert in Hinblick auf deren Potential den Hydratationsprozess zu beschleunigen. Die größte Herausforderung stellte hierbei das Zementmilieu mit stark basischen pH-Wert sowie hoher Salinität dar. Untersucht wurde der Einfluss auf den Zementhydratationsprozess mittels Wärmekalorimetrie. Die Protease papain zeigte eine beschleunigende Wirkung. Die Protease bromelain, welche eine deutlich niedrigerer pH resistenz besitzt im Vergleich zu papain, zeigte hingegen einen verzögernden Effekt. Um ein besseres Verständnis für die Wechselwirkung der Proteasen zu generieren, wurde am Beispiel von papain der Einfluss des stark basischen pH-Wertes sowie hoher Salinität auf die Reaktivität des aktiven Zentrums untersucht. Der Enzymaktivitätstest coomassie Blue Assay

wurde verwendet. Es zeigte sich eine deutliche Verringerung der Aktivität nach Inkubation in basischer bzw. salzhaltiger Lösung. Ebenfalls konnte die Deaktivierung des aktiven Zentrums der Protease erfolgreich nachgewiesen werden. Nach Deaktivierung der Protease konnte der beschleunigende Effekt auf den Zementhydratationsprozess nicht reproduziert werden mittels Wärmekalorimetrie. Dies deutet stark auf eine Wechselwirkung und Beteiligung des aktiven Zentrums am beobachteten Effekt.

# List of abbreviations

## Physical quantity

$T$ (°C)	temperature
$U$ (mV)	potential
$R$ (JK <sup>-1</sup> mol <sup>-1</sup> )	gas constant
$F$ (Cmol <sup>-1</sup> )	Faraday constant
$R_{H,app}$ (nm)	hydrodynamic radius
$R_g$ (nm)	gyration radius
$c$ (mol/L)	concentration
$\zeta$ (V)	zeta-Potential
$P$ (W)	power
$t$ (min)	time
$a_i$ (mol/L)	activity
$n$ (mol)	amount of substance
$m$ (g)	mass

## Abbreviation

SO <sub>3</sub>	sulfur trioxide
A = Al <sub>2</sub> O <sub>3</sub>	aluminium oxide
at.-%	atom fraction
C = CaO	calcium oxide
C/S	calcium to silicon ratio
C <sub>2</sub> S	belite Ca <sub>2</sub> SiO <sub>4</sub>
C <sub>3</sub> A	aluminate Ca <sub>3</sub> Al <sub>2</sub> O <sub>6</sub>
C <sub>3</sub> S	alite Ca <sub>3</sub> SiO <sub>5</sub>
C <sub>4</sub> AF	ferrit Ca <sub>4</sub> Al <sub>2</sub> Fe <sub>2</sub> O <sub>10</sub>
CNT	classical nucleation theory
CS	calcium sulphate
C-S-H	calcium silicate hydrate
DADMAC	diallyldimethylammoniumchlorid
DLS	dynamic light scattering
EDTA	ethylenediaminetetraacetic acid
F = Fe <sub>2</sub> O <sub>3</sub>	iron oxide
FTIR	fourier transform infrared spectroscopy
H = H <sub>2</sub> O	water
$H_{max}$	main heat flow event
$HoH$	heat of hydration
IAP	ion activity product
IC	isothermal calorimetry
ICP-OES	inductively-Coupled Plasma Optical Spectroscopy
ISE	ion-sensitive electrodes
m	mono
$m_1$	pre-nucleation slope
$m_2$	post-nucleation slope
MICP	microbiologically induced calcite precipitation
NEM	n-ethylmaleimide

$n_{max}$	the amount of free calcium in solution
OPC	ordinary Portland cement
PAGE	polyacrylamide gel electrophoresis
PCE	polycarboxylate ether
PCN	prenucleation cluster
PTFE	polytetrafluoroethylene
PVDF	polyvinylidenefluorid
$S = SiO_2$	silicium dioxide
SAXS	small angle X-ray scattering
SDS	sodium dodecyl sulphate
SI	saturation index
SLS	static light scattering
t	tri
TEM	transmission electron microscopy
TEMED	tetramethylethylenediamine
$t_{max}$	time of the nucleation point
w.-%	mass fraction
$C_6\bar{A}S_3H_{32}$	ettringite
$C_2\bar{A}H_8$	metastable calcium aluminate hydrates
$C_4\bar{A}SH_{12}$	cubic hydrates
$Q^{0,1,2,3,4}$	notation used in $^{29}Si$ -NMR spectroscopy for Si with four oxygens attached; the numbers 0–4 denote the number of ‘Si’ units attached through the oxygen to an individual silicon atom.
T-based	tobermorite based
J-based	jennit based

## **General background**

## 2.1 Introduction and scope

Despite a millenary history and the ubiquitous presence of cement in everyday life the molecular processes underlying its hydration like the formation of calcium-silicate-hydrate (C-S-H), the binding phase of concrete, are mostly unexplored. The key reaction in cement production is the endothermic breakdown of calcium carbonate into calcium oxide and CO<sub>2</sub> – there is a high CO<sub>2</sub> production in making cement. As cement production is responsible for 5 percent of annual global CO<sub>2</sub> production, where is much interest in predicting and improving the performance of its hardening process. (1)

The production of cement releases greenhouse gas emissions both directly and indirectly: the heating of limestone releases CO<sub>2</sub> directly, while the burning of fossil fuels to heat the kiln indirectly results in CO<sub>2</sub> emissions. The direct emissions of cement occur through a chemical process called calcination. Calcination occurs when limestone, which is made of calcium carbonate, is heated, breaking down into calcium oxide and CO<sub>2</sub>. (2) Reducing emissions from the calcination process means looking to a material other than limestone. Blended cement replaces some of the limestone-based clinker with other materials, primarily coal fly ash and blast furnace slag. Indirect emissions are produced by burning fossil fuels to heat the kiln. Kilns are usually heated by coal, natural gas, or oil, and the combustion of these fuels produces additional CO<sub>2</sub> emissions, just as they would in producing electricity. One promising line of attack involves finding ways to reduce the roasting temperature during clinker production and thus reducing the fuel consumption. Indirect emissions from burning fossil fuels to heat the kiln can be reduced by switching to alternative fuels, including natural gas, biomass and waste-derived fuels such as tires, sewage sludge and municipal solid wastes. The main targets phases during clinker production are the calcium silicate phases alite and belite, that transform into calcium silicate hydrate (C-S-H), the main binding phase in cement, during hydration.



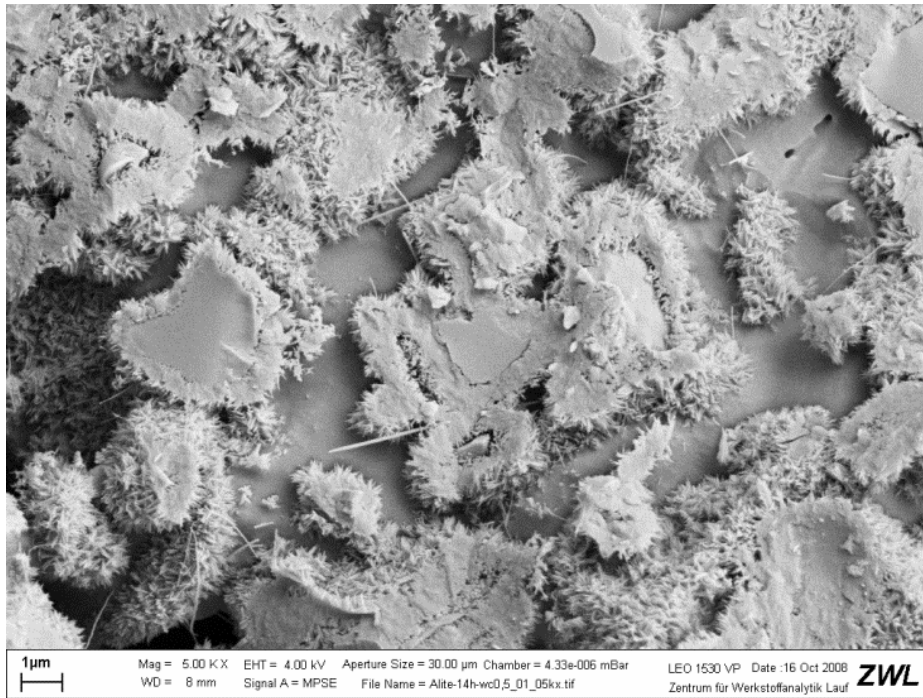


**Figure 1.** Typical SEM micrograph of the alite phase in ordinary Portland cement with calcium silicate hydrate needles after x hours of hydration.

Pellenq et al. investigated whether some belite crystal structures might be as reactive as alite yet still formed at lower kiln temperatures and thus saving fuel. Because the answer to that question depends on atomic-scale details such as the distribution of electrons in the crystal, they carried out quantum-mechanical calculations of how the structure was affected.<sup>(3)</sup> Another way is to substitute some of the concrete with supplementary cementitious materials (SCMs). SCMs are typically by-products from large-scale industrial processes, such as slag and fly ash, which is ecologically beneficial. Another means is the development of new concrete additives which could produce stronger, more workable material whilst reducing the amount of cement required. Most of the additives used in cement are added to control the properties of concretes and mortars at the early stage, and almost all of them influence the hydration of anhydrous cement phases. In particular, the role of admixtures on nucleation and growth of C-S-H is poorly understood. Except for the work of Garrault et al. <sup>(4)</sup>, which uses solution conductimetry that has been conducted and interpreted with the classical nucleation theory (CNT) precepts, the nucleation of C-S-H has never been experimentally studied under the light of the most advanced techniques. The past 25 years have witnessed major improvements in our understanding of nucleation processes,<sup>(5)</sup> and many 'new' chemical pathways, significantly differing from the classical nucleation theory (CNT), have emerged from experimental data sets. The majority of comprehensive studies first focused on minerals of geological interest, and foremost on calcium carbonate species.<sup>(6)</sup> Besides calcium carbonate, other inorganic materials of large industrial

relevance have been so far less investigated, with one exception which is the thorough study on calcium sulphates done by van Driessche.<sup>(7)</sup> The first part of this work examines in detail the nucleation of calcium silicate hydrate (C-S-H), which is the hydrated phase gluing the cement grains together and thus giving the mechanical properties to cement-based materials for example in concrete or mortar applications.

The precipitation of C-S-H around the cement grains is the first remarkable physical transformation of the cement suspension during the hardening process. The  $C_3S$  to C-S-H conversion is the key reaction that determines the strength development after the cement has set. Typically, first C-S-H particles appear on the surface of anhydrous silicate grains (or other substrates if present) and further develop by an aggregation process. Even if the C-S-H nucleation is clearly a heterogeneous process in application conditions, the first part of this work focuses on the investigation of the homogeneous nucleation from supersaturated solutions in order to constitute a first solid reference foundation for further studies. In contrast to the work of Garrault et al., the dissolution process was decoupled from the precipitation process of the C-S-H formation in order to provide an increased insight into the early stages of nucleation by starting from a supersaturated solution. Several different experimental approaches have been employed to understand the mechanism of the crystal nucleation from solution. Cryo-Transmission electron microscopy (Cryo-TEM) techniques provided two-dimensional snapshots of the nucleation events. Various scattering methods, as dynamic and static light scattering (DLS and SLS) in addition with small angle X-ray scattering (SAXS), were examined as macroscopic measurements to perform an ensemble average. They provided information about a large number of independent nucleation events for a whole set of rather small configurations of the nucleation system. It is general consensus that the C-S-H precipitating during cement hydration belongs to the family of inosilicates, however its structure in detail is still not fully understood. Mostly it is thought to be a defect variant of the natural 14 Å tobermorite structure that consists of calcium sheets flanked on each side by linear silicate “dreierketten” chains. The stoichiometry of C-S-H, i.e., the calcium to silicon ratio (C/S) and the number of water molecules, is variable mainly according to the concentration of calcium hydroxide in solution.<sup>(8)</sup> In the course of this work, the characterization of the synthesized calcium silicate hydrates *via* the atomic ratios was investigated *via* STEM-EDX (Scanning Transmission Electron Microscopes-Energy-dispersive X-ray spectroscopy) analysis. In addition, Fourier transform infrared spectroscopy (FTIR) was carried out to identify possible reaction products as calcium carbonate or portlandite appearing typically during the formation of C-S-H. This work highlights the points that differ from the classical vision of the

nucleation and provides a new insight into the morphology of the first formed species and possible intermediates during the reaction pathway. In addition to this, the experimental data was encompassed in the classical treatment of nucleation kinetics. The ability to control or manipulate the material at the atomic scale provides a deeper understanding of the process and enables the active interference with the hydration processes of C-S-H in terms of hardening benefits and mechanical performance.

In the further course of this work, the influence of polymers used as cement additives was examined in the designed reaction system. A large variety of additives was investigated by using a combination of turbidimetry with parallel monitoring of ion concentrations with an ion-selective electrode. The setup reduces the amount of complicated and time intensive sample preparation procedure and decreases the analysis time of each polymer. A fast comparison of the interaction of polymers with different functionalities with the early hydrated phases provides a new route towards the control of mechanical properties and a deeper understanding of the working mechanism of cement additives. A variation of positive charge density of cationic polymers was analysed. In the course of improving the mechanical properties by addition of certain additives, the so-called “biocement” has demonstrated its effectiveness in enhancing mechanical properties and durability of cementitious materials.<sup>(9)</sup> Microbial metabolic activities often contribute to selective cementation by producing relatively insoluble organic and inorganic compounds intra- and extracellularly; such a compound can serve as a cementitious material – the term used is ‘biocement’. Being an economic and eco-friendly biomaterial, biocement has a huge potential to improve the durability of building materials. There is still much research to be done in the area of biocement and it is highly desirable to find further bio-additives with the potential to improve concrete’s properties. So far, proteins catalysing silica formation have inspired innovative high-performance composites for construction applications. The aim of this last part of the study is to verify whether proteins with silica activity, like silicatein, can also reach their potential of accelerating silicate-condensation under less physiological conditions, such as the cement-environment with an extremely basic pH and high salinity on a laboratory level. Several proteins popular from the field of silica mineralisation were added to the hydration process and the influence was analysed *via* isothermal calorimetry (IC). Using only small amounts of proteins as additives with catalytic activity can reduce possible negative effects on the performance of ordinary Portland cement (OPC) by changing the typical composition.

## 2.2 Classical and non-classical crystallization

The past few decades have witnessed an impressive body of experimental work devoted to crystal nucleation. For instance, there are now novel techniques such as transmission electron microscopy at very low temperatures (cryo-TEM). Thanks to these, we are now able to peek in real time into the early stages of crystallization. A substantial effort has also been made to understand which materials, in the form of impurities within the liquid phase, can either promote or inhibit nucleation events. This is a common scenario known as heterogeneous nucleation. However, our understanding of crystal nucleation is far from being complete. This is because the molecular (or atomistic) details of the process are largely unknown because of the very small length scale involved (nanometers). It is thus exceptionally challenging to probe in real time even with state-of-the-art measurements.

### 2.2.1 Classical nucleation theory

Classical nucleation theory (CNT) was formulated 90 years ago in the contributions of Volmer and Weber,<sup>(10)</sup> Farkas,<sup>(11)</sup> Becker and Doring,<sup>(12)</sup> and Zeldovich.<sup>(13)</sup> These were based on the pioneering ideas of none other than Gibbs himself.<sup>(14)</sup> CNT was derived to describe the condensation of supersaturated vapours into the liquid phase. However, most of the concepts can also be applied to the crystallization of supercooled liquids and supersaturated solutions. According to CNT, clusters of crystalline atoms (or particles or molecules) of any size are treated as macroscopic objects. These are homogeneous chunks of a crystalline phase separated from the surrounding liquid by a vanishingly thin interface. This apparently trivial assumption is known as the capillarity approximation, which encompasses most of the strengths and weaknesses of the theory. According to the capillarity approximation, the interplay between the interfacial free energy,  $\gamma_s$ , and the difference in free energy between the liquid and the crystal,  $\Delta\mu_v$ , fully describes the thermodynamics of crystal nucleation. In three dimensions, the free energy of formation,  $\Delta G_N$ , for a spherical crystalline nucleus of radius  $r$  with the volume per molecule,  $\Omega$ , can thus be written as the sum of a surface term and a volume term

$$\Delta G_N = 4\pi r^2 \gamma_s - \left(\frac{4}{3}\pi r^3 / \Omega\right) \mu_v \quad (1)$$

This function displays a maximum corresponding to the critical nucleus size  $r^*$

$$r^* = \frac{32\rho_c \gamma_s}{3 \Delta\mu_v^3} \quad (2)$$

where  $\rho_c$  is the number density of the crystalline phase. The critical nucleus size represents the number of atoms that must be included in the crystalline cluster for the free energy difference,  $\Delta\mu$ . This is done to match the free energy cost due to the formation of the solid–liquid interface. Clusters of crystalline atoms occur within the supercooled liquid by spontaneous, infrequent fluctuations, which eventually lead the system to overcome the free energy barrier for nucleation can be determined by substituting (2) into (1) to get:

$$\Delta G_N^* = \left(\frac{16}{3}\right)\pi\gamma_S^3 \left(\frac{\Omega}{k_B T \sigma}\right)^2 \quad (3)$$

with the supersaturation,  $\sigma$ , which is defined as  $\ln(IAP/K_{sp})$ , the ratio of the activity product of reactants,  $IAP$ , and the value of the equilibrium constant,  $K_{sp}$ . The kinetics of crystal nucleation is typically addressed by assuming that no correlation exists between successive events increasing or decreasing the number of constituents of the crystalline nucleus. In other words, the time evolution of the nucleus size is presumed to be a Markov process. In this process, atoms in the liquid either order themselves one by one in a crystalline fashion or dissolve one by one into the liquid phase. In addition, we state that every crystalline nucleus lucky enough to overcome the critical size  $r^*$  quickly grows to macroscopic dimensions on a time scale much smaller than the long time required for that fortunate fluctuation to come about. If these conditions are met, the nucleation rate, that is, the probability per unit time per unit volume of forming a critical nucleus does not depend on time. This leads to the following formulation of the so-called steady-state nucleation rate  $J$

$$J = J_o \exp\left(\frac{-\Delta G_N^*}{k_B T}\right) \quad (4)$$

where  $k_B$  is the Boltzmann constant and  $J_o$  is a prefactor that is discussed later. The steady-state nucleation rate is the central quantity in the description of crystallization kinetics, as much as the notion of critical nucleus size captures most of the thermodynamics of nucleation. All quantities specified up to now depend on pressure and, most notably, temperature. In most cases, the interfacial free energy,  $\gamma_S$ , is assumed to be linearly dependent on temperature, whereas the free energy difference between the liquid and solid phases,  $\Delta\mu$ , is proportional to the supercooling,  $\Delta T = T_M - T$  (or the supersaturation). Several approximations exist to treat the temperature dependence of  $\gamma_S$ , and  $\mu_V$ . In any case, it follows from that the free energy barrier for nucleation,  $\Delta G_N^*$  decreases with supercooling. In other words, the farther one is from the melting temperature  $T_M$ , the larger the thermodynamic driving force for nucleation is. Some other quantities, such as the size of the critical cluster, depend in many cases rather strongly on the degree of supercooling. This is

the case, for example, for the critical nucleus size  $n^*$ , which can easily span 2 orders of magnitude in just 10 °C of supercooling. (15)

### 2.2.2 Two-step nucleation

Given with time, it is no surprise that substantial efforts have been devoted to extending and/or improving its original theoretical framework. The most relevant modifications possibly concern the issue of two-step nucleation. Many excellent works have reviewed this subject extensively (15-17) so that only the essential concepts will be provided here. In the original formulation of CNT, the system has to overcome a single free energy barrier, corresponding to a crystalline nucleus of a certain critical size, as depicted in Figure 3. When dealing with crystal nucleation from the melt, it is rather common to consider the number of crystalline particles within the largest connected cluster,  $n$ , as the natural reaction coordinate describing the whole nucleation process. In many cases, the melt is dense enough that local density fluctuations are indeed not particularly relevant. Moreover, the slow degree of freedom is, in fact, the crystalline ordering of the particles within the liquid network. However, one can easily imagine that, in the case of crystal nucleation of molecules in solutions, for example, the situation can be quite different. Specifically, in a realistically supersaturated solution, a consistent fluctuation of the solute density (concentration) could be required just to bring a number  $n_p$  of solute molecules close enough to form a connected cluster. Assuming that the molecules involved in such a density fluctuation will also order themselves in a crystalline fashion on exactly the same timescale is rather counterintuitive. In fact, the formation of crystals from molecules in solution often occurs according to a two-step nucleation mechanism that has no place in the original formulation of CNT. In the prototypical scenario depicted in Fig.1, a first free energy barrier,  $\Delta n_p$ , *two-step\**, has to be overcome by means of a density fluctuation of the solute, such that a cluster of connected molecules of size  $n_p^*$  is formed. This object does not yet have any sort of crystalline order. Depending on the system under consideration, it can be either unstable or stable with respect to the supersaturated solution (see Figure 2).

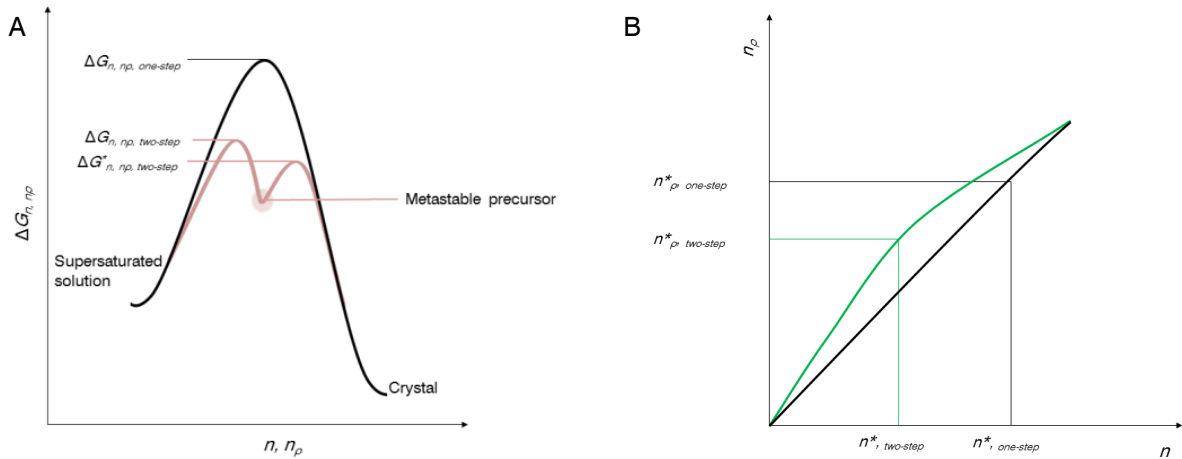


**Figure 2:** Schematic comparison of one-step versus two-step nucleation for a generic supersaturated solution.

(A) Sketch of the free energy difference  $\Delta G_{n, n\rho}$  as a function of the number of solute molecules in the largest “connected” cluster (they can be ordered in a crystalline fashion or not) ( $n\rho$ ) and of the number of crystalline molecules within the largest connected cluster ( $n$ ). The one-step mechanism predicted by CNT (black) is characterized by a single free energy barrier for nucleation,  $\Delta G_{n, n\rho, one-step}^*$ . In contrast, the two-step nucleation requires a free energy barrier,  $\Delta G_{n\rho, two-step}^*$ , to be overcome through a local density fluctuation of the solution, leading to a dense, but not crystalline-like, precursor (brown). Once this dense precursor has been formed, the second step consists of climbing a second free energy barrier,  $\Delta G_{n, two-step}^*$ . This corresponds to the ordering of the solute molecules within the precursor from a disordered state to the crystalline phase. (B) One-step (black) and two-step (brown) nucleation mechanisms visualized in the density ( $n\rho$ )–ordering ( $n$ ) plane. The one-step mechanism proceeds along the diagonal, as both  $n\rho$  and  $n$  increase at the same time in such a way that a single free energy barrier has to be overcome. In this scenario, the supersaturated solution transforms continuously into the crystalline phase. On the other hand, within a two-step nucleation scenario, the system has to experience a favourable density fluctuation along  $n\rho$  first. This forms a disordered precursor that, in a second step, orders itself in a crystalline fashion, moving along the ( $n$ ) coordinate and ultimately leading to the crystal.

Subsequently, the system has to climb a second free energy barrier,  $\Delta G_{n,two-step}^*$ , to order the molecules within the dense cluster in a crystalline-like fashion. In all of these cases, CNT, as it is formulated, is simply not capable of dealing with two-step nucleation. This is why, in the past few decades, a number of extensions and/or modifications of CNT have been proposed and indeed successfully applied to account for the existence of a two-step mechanism. The phenomenological theory of Pan et al. (18) who wrote an expression for the nucleation rate assuming a free energy profile similar to the one sketched in Fig.1. where dense metastable states are involved as intermediates on the path towards the final crystalline structure. The emergence of so-called prenucleation clusters (PNCs), namely, stable states within supersaturated solutions, was also recently fit into the framework of CNT by Hu et al. (19) PNC's are known to play a very important role in the crystallization of biominerals, for example. Hu et al. proposed a modified expression for the excess free energy of the nucleus, which takes into account the shape, size, and free energy of the PNCs as well as the possibility for the PNCs to be either metastable or stable with respect to the solution. It is worth noting that these extensions of CNT are mostly quite recent, as they were triggered by the overwhelming experimental evidence for two-step nucleation mechanisms.

### 2.2.3 Heterogeneous nucleation

CNT is also the tool of the trade for heterogeneous crystal nucleation, that is, nucleation that occurs on account of the presence of a foreign phase (Figure 2). In fact, nucleation in liquids occurs heterogeneously more often than not, as in some cases, the presence of foreign substances in contact with the liquid can significantly lower the free energy barrier  $\Delta G_N$ . Heterogeneous nucleation is customarily formulated within the CNT framework in terms of geometric arguments. (20) Specifically,

$$G_{N(heterogeneous)}^* = G_{N(homogeneous)}^* f(\theta) \quad (5)$$

where  $f(\theta) \leq 1$  is the shape factor, a quantity that accounts for the fact that three different interfacial free energies must be balanced:  $\gamma_{lc(liquid,crystal)}$ ,  $\gamma_{sc(foreign\ phase,crystal)}$  and  $\gamma_{ls(liquid,foreign\ phase)}$ .



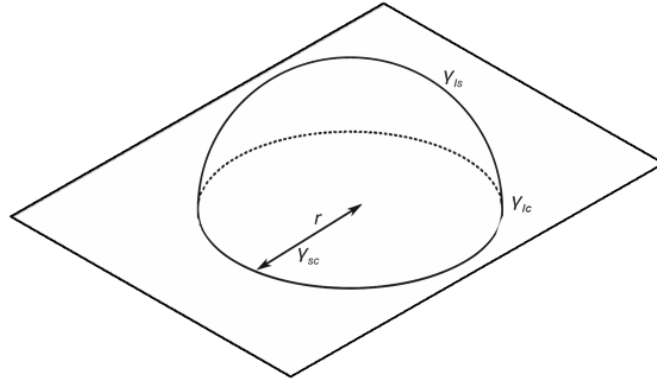


**Figure 3:** Heterogeneous formation of a hemispherical nucleus at a foreign substrate with the three different interfacial free energies  $\gamma_{sc}$ ,  $\gamma_{lc}$  and  $\gamma_{ls}$ .

For instance, considering a supercooled liquid nucleating on top of an ideal planar surface offered by the foreign phase, we obtain the so-called Young's relation

$$\gamma_{S(\text{liquid,foreign phase})} = \gamma_{S(\text{crystal,foreign phase})} + \gamma_{S(\text{crystal,liquid})} \cos\theta \quad (6)$$

where  $\theta$  is the contact angle, namely, a measure of the extent to which the crystalline nucleus wets the foreign surface. Thus, the contact angle determines whether and how much it could be easier for a critical nucleus to form in a heterogeneous fashion, as for  $0 \leq \theta < \pi$ . Here, the volume-to-surface energy ratio  $\Delta\mu_v/\gamma_s$  is larger for the spherical cap nucleating on the foreign surface than for the sphere nucleating in the liquid. This simple formulation is clearly only a rough approximation of what occurs in reality. In reality a foreign surface is not perfectly flat. At first, the contact angle is basically a macroscopic quantity of which the microscopic equivalent is in most cases ill-defined on the typical length scales involved in the heterogeneous nucleation process. In addition, in most cases, the nucleus will not be shaped like a spherical cap. To make things more complicated, many different nucleation sites with different morphologies typically exist on the same impurity.

## 2.2.4 Experimental methods

Several different experimental approaches have been employed to understand the thermodynamics and kinetics of crystal nucleation in liquids. As already stated, nucleation is a dynamical process usually occurring on very small time and length scales (nanoseconds and nanometres, respectively). Indeed, true microscopic insight has rarely been achieved. For instance, colloids offer a playground where simple microscopy can image the particles involved in the nucleation events. These events occur on such long time scales (seconds) that a full characterization in a time of the process has been achieved.<sup>(21)</sup> Specifically, confocal microscopy has led to the three-dimensional imaging of colloidal systems,

unravelling invaluable information about the critical nucleus size, for example.(22, 23) In a similar fashion, Sleutel et al. achieved molecular resolution of the formation of two-dimensional glucose isomerase crystals by means of atomic force microscopy.(24) This particular investigation featured actual movies showing both crystal growth and the dissolution of pre-critical clusters, as well as providing information about the influence of the substrate. In addition, cryo-TEM techniques have recently provided two-dimensional snapshots of nucleation events at very low temperatures. In selected cases, where the time scales involved are, again, in the order of seconds, dynamical details have been obtained, as in the cases of  $\text{CaCO}_3$ , (25) metal phosphate, and magnetite.(26) However, more often than not, crystal nucleation in liquids takes place within time windows too small (nanoseconds) to allow for a sequence of snapshots to be taken with high-spatial resolution instruments. In these cases, microscopic insights cannot be obtained, and many more macroscopic measurements have to be performed. In this context, several experimental approaches aim at examining a large number of independent nucleation events for a whole set of rather small configurations of the system, basically performing an ensemble average. For example, in droplet experiments, nucleation is characterized as a function of time or temperature. Freezing is identified for each nucleation event within the ensemble of available configurations by techniques such as femtosecond X-ray scattering,(27) optical microscopy,(28) and powder X-ray diffraction.(29, 30) From these data, the nucleation rate is often reconstructed by measuring either metastable zone widths.(30-32) This provides a solid connection to theoretical frameworks such as CNT. An essential technical detail within this class of measurements is that the volume available for each nucleation event has to be as small as possible to reduce the occurrence of multiple nucleation events within the same configuration. Another line of action focuses on the study of large, macroscopic systems. Freezing is detected by techniques such as differential scanning calorimetry,(33, 34) Fourier transform infrared spectroscopy (FTIR)(35, 36) and analytical ultracentrifugation. In this case, the frozen fraction of the overall system and/or the nucleation temperatures can be obtained, and in some cases, nucleation rates have been extracted. In addition to the already mentioned methods, Gebauer et al. combined the analytical ultracentrifugation with parallel monitoring of ion concentrations with the ion-selective electrode to evaluate the effect of various peptides on the nucleation of calcium carbonate.(6) In the course of this study, in addition to the well-known methods like cryo-TEM, DLS, SLS and FTIR, the potentiometric measurements were carried out and combined with a turbidity measurement to study the ongoing process in-situ.

## 2.3 Biosilification

In biological mineralizing systems, the formation of inorganic structures occurs in aqueous media at neutral pH by a set of biomolecules, such as proteins and polysaccharides. A prototypical case is provided by marine sponges and diatoms.<sup>(37)</sup> Organisms are able to synthesize a variety of inorganic materials (calcium carbonate, calcium phosphate, silica, iron oxide, etc.) from simple precursors under mild reaction conditions. This results in highly complex structures with several levels of hierarchy, ranging from the nano-level to the macro level (Figure 4).<sup>(38, 39)</sup>

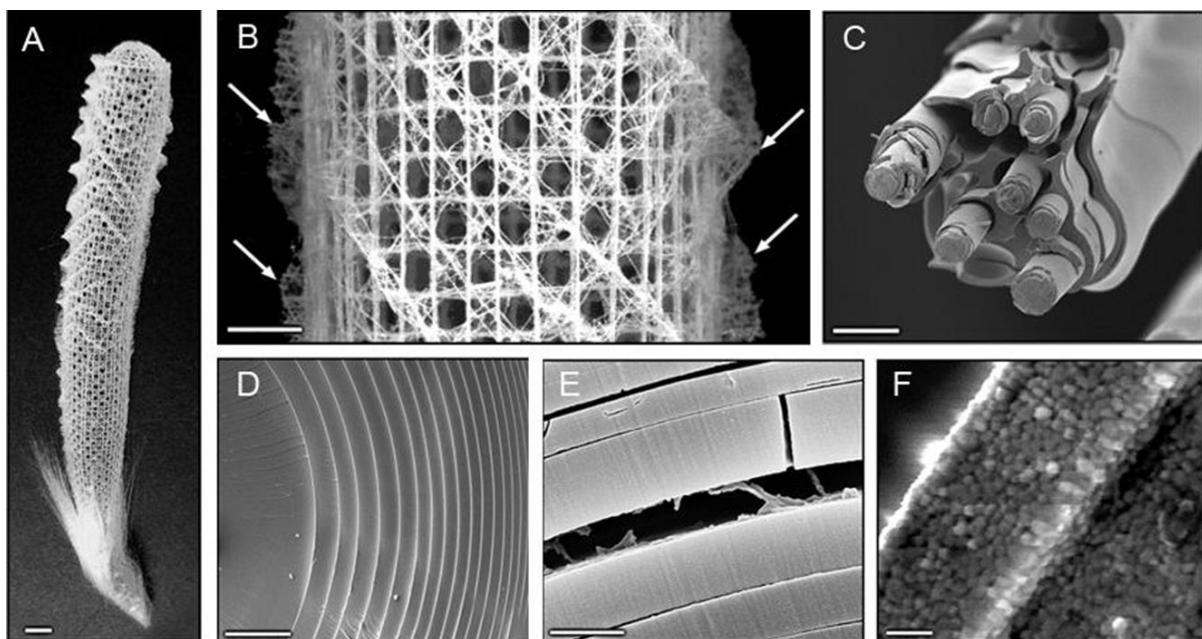


**Figure 4:** Several levels of hierarchy in the structure of the skeleton of the glass sponge *Euplectella*. **(A)** photograph of entire skeleton, scale bar: 1 cm; **(B)** Fragment of the cage structure showing the square-grid lattice, scale bar: 5 mm; **(C)** fractured and partially HF-etched single beam revealing its ceramic fibre-composite structure, scale bar: 20  $\mu\text{m}$ ; **(D)** cross section through a typical spicule in a strut, showing its characteristic laminated architecture, scale bar: 5  $\mu\text{m}$ ; **(E)** fractured spicule, revealing an organic interlayer, scale bar: 1  $\mu\text{m}$ ; **(F)** bleaching of biosilica surface revealing its consolidated nanoparticulate nature, Scale bar: 500 nm. (Science 2005, 8, 5732.)

These mineralized inorganic–bioorganic composite materials are formed either by controlled condensation in specific compartments or by regulating the concentration of the inorganic precursors with the help of enzymes. Diatoms<sup>(37)</sup> and sponges<sup>(40)</sup> provide classical examples of biosilification processes whereby complex and unique 3D structures are synthesized even with very low concentrations of silicon present in the surrounding environment. Great efforts have been made to isolate, purify and characterize proteins and

other biomolecules driving the mild synthetic route of silica polymerization in vivo. Prominent examples include long-chain polyamines and silafins from diatom shells and silicateins from marine sponges. The formation of silica spicules in marine sponges is of particular interest because of their hierarchical structures and the resulting properties. That is, the spicules have high mechanical strength and are excellent optical waveguides. Other examples are the hexactinellid sponge *Euplectella marshalli*, whose skeletal structure is composed of elaborate cylindrical structures with six hierarchical levels, (Figure 4). By emulating the chemistry behind natural mineralization pathways, the known biomineralization agents might be employed to fabricate materials with non-natural compositions and with a wide spectrum of properties.<sup>(38)</sup> The isolated biomolecules involved in silica formation, e.g. silaffins, siladicins, and silicateins, are also a source of inspiration for the use of other biomolecules. This includes, for example, synthetic polyamines, polypeptides, and a variety of polymers that mimic the active site of either silaffins or silicatein (e.g., diblock copolymers) to perform similar task.<sup>(41)</sup> The structures, compositions and molecular masses of the bioinspired polymers, as well as the experimental conditions used in the laboratory (e.g. buffer composition and pH), have been shown to significantly affect the kinetics of the condensation and precipitation processes. Also the shape of the formed silica colloids is affected, which can range from typical spherical shapes to hexagons or other more complex forms.<sup>(42, 43)</sup> For bioinspired silaffin-related silicification, the mechanism of silica formation from solutions containing such additives involves an electrostatic interaction between positively charged amines and negatively charged silica precursors. This facilitates the passive condensation of silica around the amine group. Additionally, the molecular backbone acts as a template for the structure of the deposited material. In contrast to other organisms that deposit silica in a passive, template controlled manner, marine sponges (phylum Porifera) show the singular ability to actively synthesize their siliceous skeleton enzymatically.<sup>(44, 45)</sup> The materials formed often exhibit crystalline polymorphs that normally require high temperatures or extreme pH conditions for preparation by classical synthetic methods.<sup>(46)</sup> This indicates that enzymes of the marine sponge-like silicateins have a relatively flexible active centre, and a very general mechanism can, therefore, be assumed to underlie their catalytic activity.

## 2.4 Fundamentals of cement chemistry

In this chapter, an overview of important concepts of cement chemistry is presented. (2)

Ordinary Portland cement consists of four major mineral phases (2)

Alite  $\text{Ca}_3\text{SiO}_5$  (50-79 weight %)

Belite  $\text{Ca}_2\text{SiO}_4$  (15-30 weight %)<sup>1</sup>

Aluminate  $\text{Ca}_3\text{Al}_2\text{O}_6$  (5-10 weight %)

Ferrite  $\text{Ca}_4\text{Al}_2\text{Fe}_2\text{O}_{10}$  (5-15 weight %)

Typical incorporation ions in the corresponding mineral phases include:

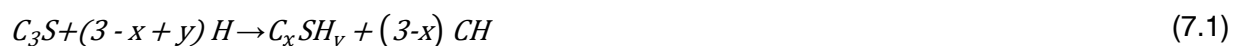
$\text{C}_3\text{S}/\text{C}_2\text{S}$ :  $\text{Mg}^{2+}$ ,  $\text{Al}^{3+}$ ,  $\text{Fe}^{3+}$

$\text{C}_3\text{A}$ :  $\text{Si}^{4+}$ ,  $\text{Fe}^{3+}$ ,  $\text{Na}^+$ ,  $\text{K}^+$

### 2.4.1 The different mineral phases of ordinary portland cement

#### Silicate reactions

The main silicate phases to be considered are  $\text{C}_3\text{S}$ ,  $\beta\text{-C}_2\text{S}$ ,  $\alpha\text{-C}_2\text{S}$ . These react to form C-S-H and CH.  $\beta\text{-C}_2\text{S}$  behaves like  $\text{C}_3\text{S}$  but it reacts slightly slower and forms more C-S-H and less CH.  $\gamma\text{-C}_2\text{S}$  reacts very slowly and is considered to be unreactive compared to  $\text{C}_3\text{S}$ . In general,  $\text{C}_3\text{S}$  and  $\beta\text{-C}_2\text{S}$  are reacted to 70% and 30%, respectively, after 28 days, and almost all and 90% after 1 year. C-S-H is an amorphous rigid hydrate which gives strength to the cement paste. There are many different forms of C-S-H that change over time and under many different environmental conditions. As the temperature increases, the density of the C-S-H increases. This increase in density explains the decrease in late age strengths due to the slowing of diffusion through the C-S-H which slows  $\text{C}_3\text{S}$  dissolution. The  $\text{C}_3\text{S}$  reaction can be described by

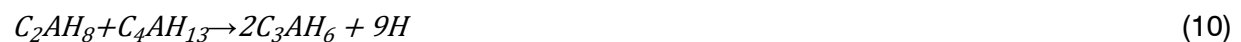


(with  $x = \text{C}/\text{S}$ ). Parameters that have an influence on the reaction rate can be the portlandite concentration, the water to solids ratio, particle size, and the temperature. The amorphous C-S-H can vary in the amounts of alumina and sulphate present in the crystalline structure

as silica replacements. Sulphate has been shown to substitute for Si in C-S-H, which is a function of the ratio of Ca/Si in the C-S-H, the S/Si ratio. Besides that, the pH and soluble alkalis have an influence on the reaction rate. The incorporation of alumina into C-S-H to form C-A-S-H has also been shown to affect the elastic modulus by nanoindentation. (47)

### Aluminate reactions

The amount of calcium sulphate has an influence on the hydration products of aluminate reactions. The hydration products of the aluminate reaction are ettringite (Aft)  $C_6\bar{A}\bar{S}_3H_{32}$ , monosulphate (AFm)  $C_4\bar{A}\bar{S}H_{12}$ , metastable calcium aluminate hydrates  $C_2AH_8$  and cubic hydrates  $C_3AH_6$ .



The  $C_3A$  reaction is diffusion controlled. Ettringite and monosulphate form when sulphate is available. The other hydrates will form when sulphate is not available. In pure  $C_3A$  systems, the amount of  $C_3AH_6$  formed depends on the temperature. With a higher temperature, the porosity decreases significantly. These hydrates form in the first few minutes of contact with water. There is no effect by the sulphate in the first few minutes on the cubic hydration. The formation of the metastable calcium aluminate hydrates and cubic hydrates at early ages is associated with flash set due to the lack of available sulphate. The decrease of available sulphate leads to an increase in  $C_3A$  dissolution and therefore to an increase in the exothermic ettringite formation. There is evidence that aluminate reactions are controlled to a greater extent when CH is present with sulphate because it slows the reaction rate of the  $C_3A$ . Sodium concentration will have an effect on the  $C_3A$  hydration changing the time of peak heat and the amount of heat evolved.

The sulphates are commonly found in AFt, AFm, in hydrated cement paste, but most sulphates are found in the AFt phase. The amount of sulphate incorporated is dependent on both, the environmental temperature and amount of carbonate. As the carbonate amount increases, the carboaluminate phase gets stabilized and more sulphate is incorporated into the ettringite. The amount of sulphate found in C-S-H-based phases was found to be dependent on the temperature of sorption, the Ca/Si ratio, the pH, and previous thermal treatment for C-A-S-H specifically. It was not dependent on the available sulphate level seen in most cement. Hydration of the  $C_3A$  in the first stage of hydration is commonly thought to

be controlled by pore diffusion through the thickening ettringite barrier. This can be controlled by varying and regulating the amount of water available for reaction with the  $C_3A$ . Researchers explain the mechanisms by the adsorption of calcium and sulphate ions onto the surface of  $C_3A$ , which blocks the dissolution sites of  $C_3A$ . This explains the high dissolution rate of  $C_3A$  when there are no sulphate ions in solution.

### Ferrite

Ferrite ( $(Al_xFe_{1-x}) Ca_2O_5$ ,  $C_4AF$ ) gives cement its grey colour. It forms products that are very similar to the products of aluminate. The reaction rate decreases with increasing F/A ratio. Aluminate and ferrite phases can cause a flash set, which is a strong evolution of heat and subsequently poor development of strength. As the aluminate reacts with calcium sulphate ( $CaSO_4 \cdot xH_2O$ ), it forms ettringite ( $C_6\bar{A}S_3H_{32}$ ).

### Calcium Carbonate

Calcium carbonate ( $CaCO_3$ ) has three crystalline anhydrous forms: calcite, aragonite and vaterite. Calcite is the thermodynamically stable form at normal atmospheric conditions. During the ageing of the concrete structure, the carbonation of OPC takes place, which changes the physical and chemical properties of the OPC. The carbonation can induce corrosion of steel, due to the reduction of alkalinity. This can cause damage to the structure.

## **2.4.2 The hydration of ordinary portland cement**

Isothermal calorimetry (IC) is one way to characterize the hydration of OPC. By IC, four stages of hydration can be characterized. The pre-induction period I, the induction period II, the acceleration period III, and the deceleration period IV. Figure 5 shows the IC of OPC with a focus on the silicate reaction and Figure 6 the IC of OPC with a focus on the aluminate reaction.

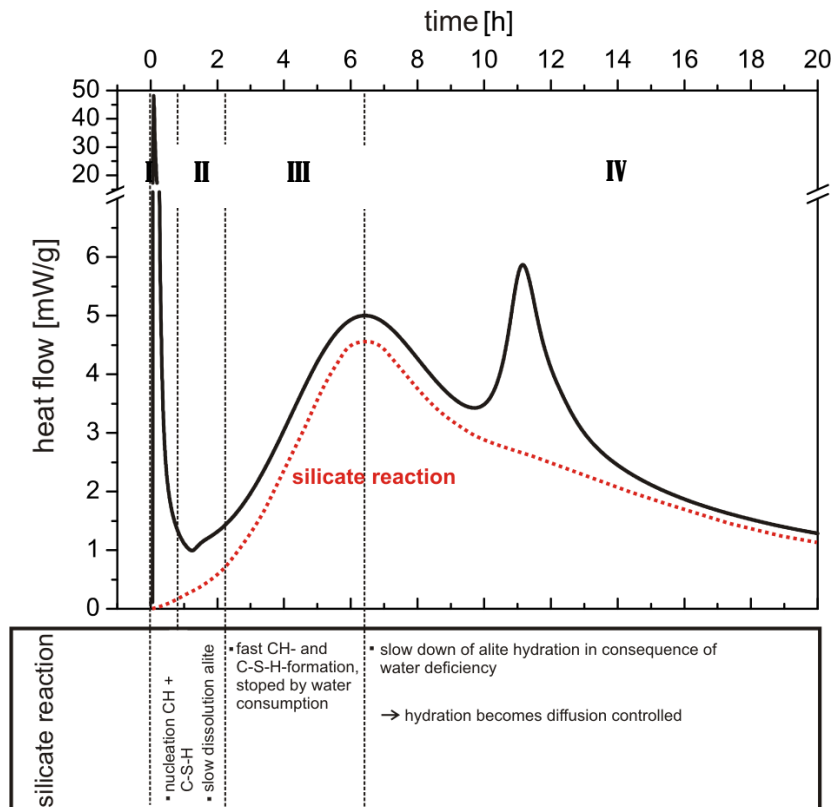


Figure 5. Isothermal calorimetry of OPC, heat flow versus time with focus on silicate reaction.

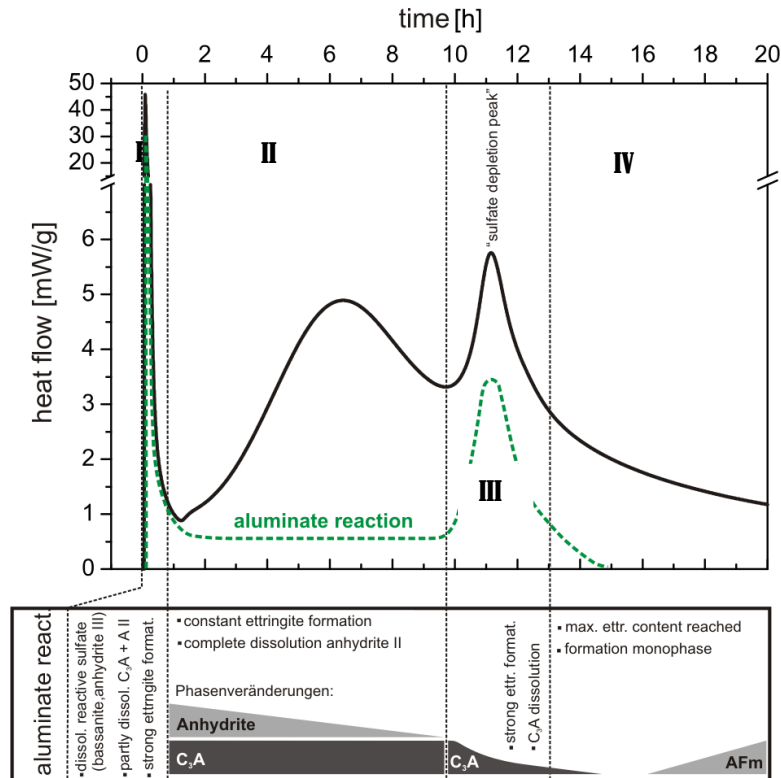


Figure 6. Isothermal calorimetry of OPC, heat flow versus time with a focus on aluminate reaction.



### Pre-induction period I

The first stage is the pre-induction period. Calcium ions, silicate and hydroxide ions are released into solution, and the calcium hydroxide dissolves from the alite. The wetting of ettringite contributes to the heat release. The dissolution reactions are followed by aluminate reactions, which lead to the formation of AFt phases which are exothermic and a small amount of C-S-H. The accepted view of the retardation mechanism of ettringite has been one of a physical coating barrier around the  $C_3A$ .

### Induction period II

The second stage is the induction period. The high solubility of  $C_3S$  is thought to be inhibited by a protective coating around the dissolution sites. The length of the induction period is strongly related to the sulphate and  $C_3A$  ratios. The lower the content of sulphates, the faster the  $C_3A$  dissolution will be. CH and C-S-H begin to precipitate at the end of the period.

### Acceleration period III

This third stage shows an acceleration of the exothermic reaction and a rapid precipitation of CH and C-S-H. The strong exothermic peak during this period is given by the reaction of  $C_3S$ . The formation and connection of the C-S-H growth sites are what leads to the increase in yield stress and a decrease in porosity.

### Deceleration period IV

During this stage, the reaction slows and starts to become diffusion controlled. The rate of C-S-H and CH formation is slowed down. In this period the formation of monosulphate starts. Another peak is seen in certain cases during this period and is labelled as the "sulphate depletion" peak in Figure 6. It was proposed that the time at which sulphate depletion occurs coincides with expansion caused by ettringite formation.

## **2.4.3 The nanostructure of C-S-H**

Given the importance of concrete to the Built Environment, a large number of models have been proposed for the nanostructure of C-S-H. The C-S-H present in hardened pastes of  $C_3S$  or neat Portland cement generally has a mean Ca/Si ratio of about 1.75, with a range of values within a given paste from around 1.2 to 2.1.

C-S-H belongs to the group of inosilicates. The inosilicates include two distinct groups, the single chain and double chain silicates. In the single chain group, the tetrahedras share two oxygens with two other tetrahedras and form a seemingly endless chain. The ratio of silicon to oxygen is thus 1:3. The tetrahedras alternate to the left and then to the right along the line formed by the linked oxygens although more complex chains seem to spiral. In cross section, the chain forms a trapezium and this shape produces the angles between the crystal faces and cleavage directions. In the double chain group, two single chains lie side by side so that all the right-sided tetrahedras of the left chain are linked by an oxygen to the left-sided tetrahedras of the right chain. The extra shared oxygen for every four silicones reduces the ratio of silicones to oxygen to 4:11. The double chain looks like a chain of six-sided rings that might remind someone of a child's clover chain. The cross section is similar in the double chains to that of the single chains except the trapezium are longer in the double chains. This difference produces a difference in angles. The cleavage of the two groups results between chains and does not break the chains thus producing prismatic cleavage. In the single chained silicates, the two directions of cleavage are at nearly right angles (close to 90 degrees) forming nearly square cross sections. In the double chain silicates, the cleavage angle is close to 120 and 60 degrees forming rhombic cross sections making a convenient way to distinguish double chain silicates from single chain silicates.<sup>2</sup> A summary of models for the nanostructure of C-S-H in hardened cement was presented by I. G. Richardson in 2008 where most of the models involve elements of the tobermorite-like structure. Five structural varieties are distinguished: Clinotobermorite, tobermorite-9 Å, tobermorite-10 Å, tobermorite-11 Å, and tobermorite-14 Å. The structural arrangement of tobermorite- 14 Å appears interesting as the crystal structure of tobermorite is related to the C-S-H phase in ordinary Portland cement. These three different phases -9 Å, -11 Å, and tobermorite-14 Å are characterized by basal spacing of 9.3, 11.3, and 14 Å. The 14 Å is the most hydrated of the group with a chemical composition of  $\text{Ca}_5\text{Si}_6\text{O}_{16}(\text{OH})_2 \cdot 7\text{H}_2\text{O}$ . It has a Ca-O sheet in the centre that has silicate chains on both sides, which are linked with a periodicity of three tetrahedral; the chains are called dreierketten, or wollastonite-like chains. The chemical composition of the complex layer is  $[\text{Ca}_4\text{Si}_6(\text{OH})_2(\text{H}_2\text{O})]^{2-}$ . The silicate chains that belong to adjacent layers are not condensed into double chains, but are shifted by  $b/2$  with respect to one another. The layers are also further apart, with the extra interlayer space occupied by  $\text{H}_2\text{O}$  molecules and  $\text{Ca}^{2+}$  ions in contrast to the tobermorite-11 Å (see Figure 7 for tobermorite-11 Å).<sup>(47)</sup>

B -2 [B 1 1 m] #8  
 a=6.735Å  
 b=7.385Å  
 c=22.487Å  
 $\alpha=90.000^\circ$   
 $\beta=90.000^\circ$   
 $\gamma=123.250^\circ$

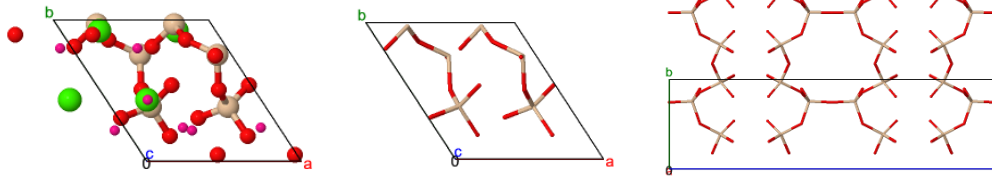


**Figure 7.** 3D crystal structure showing dreierketten chains present in 1.1 nm tobermorite projected (Ca= green, O= red, Si= brown, H= pink). (48)

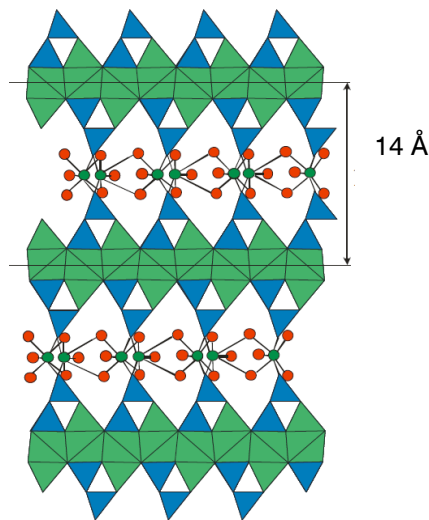


**Figure 8.** Schematic crystal structure of tobermorite-14 Å, as seen perpendicular to [010] according to Merlino and Bonaccorsi. (49) The layers of Ca polyhedral are drawn in green, whereas the silicate chains are in blue. Green circles in the complex layers represent the calcium ions and the red circles the water molecules.

The layer structure of tobermorite is illustrated in a high-resolution transmission electron micrograph. The crystal lost interlayer water under the electron beam, which resulted in a reduction in the layer spacing from 1.42 nm to 1.24 nm to 1.13 nm. This intermediate spacing of 1.24 nm is the same as the value of the basal spacing for semi-crystalline C-S-H in alkali-activated hardened cement and in many synthetic C-S-H preparations.

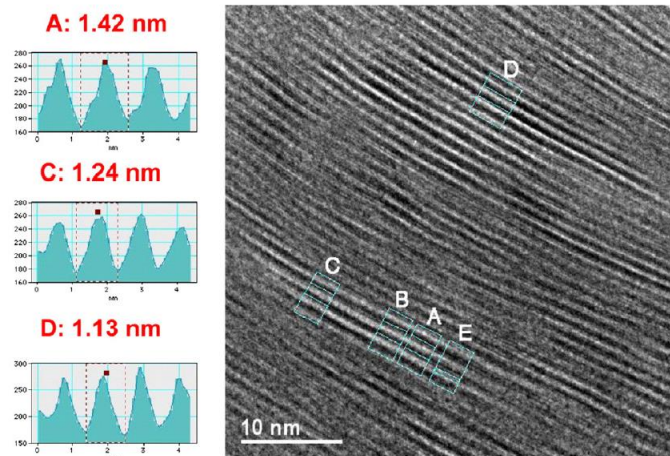


**Figure 9.** High-resolution transmission electron micrograph of 1.4 nm tobermorite from Crestmore, California, and the resulting profile plots. (3)

Another crystalline calcium silicate hydrate that has dreierketten silicate chains is jennite. It has a much higher Ca/Si ratio of 1.5 than tobermorite with a formula of  $\text{Ca}_9\text{Si}_6\text{O}_{18}(\text{OH})_6 \cdot 8\text{H}_2\text{O}$ . The structure of jennite is monoclinic (space group  $I 1 2/m 1$ ).

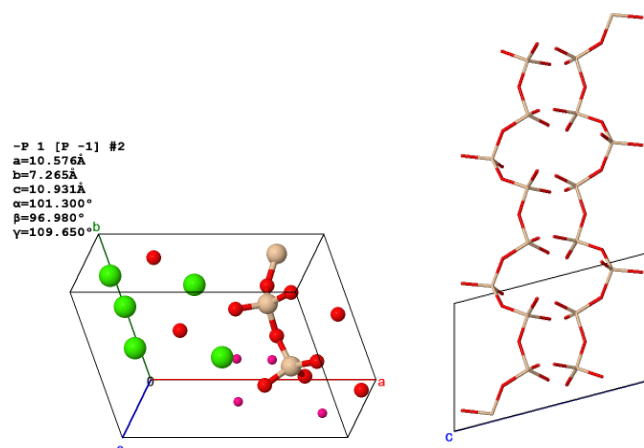


**Figure 10.** The 3D crystal structure of monoclinic jennite.

Several models for C-S-H consist of a tobermorite/jennite-based formulation for Ca/Si ratios  $\geq 1.5$ . Nonat incorporated a T/CH and T/J formulations, where one silicate bridging tetrahedra is replaced by  $\text{Ca}(\text{OH})_2$  or a non-bridging tetrahedra is replaced by OH. (50) Further insight into the transient silicate speciation and polymerization in the developing C-S-H structure was provided by solid-state  $^{29}\text{Si}$  NMR measurements of  $^{29}\text{Si}$ -enriched triclinic  $\text{Ca}_3\text{SiO}_5$ . The NMR results presented that non-hydrated  $\text{Ca}_3\text{SiO}_5$  particle surfaces predominantly consist of hydroxylated  $\text{Q}^0$  silicate species with negligible quantities of  $\text{Q}^1$  and  $\text{Q}^2$  hydration products. The onset of the hydration period corresponds to the formation of dimeric units in C-S-H. The results provided further information about the relative fractions in

the further course of hydration of  $Q^1$ ,  $Q^2$  and  $Q^{2L}$  species associated with C-S-H units of different chain lengths. The analysis yielded estimates of 20 mole%, 5 mole%, and 75 mole% for the octameric, pentameric, and dimeric units.

#### 2.4.4 Accelerating admixtures

The function of accelerating admixtures can be used either to increase the rate of stiffening/setting of the concrete or to increase the rate of hardening and early strength gain to allow earlier demoulding and handling. But most accelerators primarily achieve one rather than both of these functions. Set accelerators are a very effective way of controlling the setting time of such concretes but can reduce the later strength development when dosed in high amounts.<sup>(51)</sup> The most cost-effective accelerator for all OPC is calcium chloride. It provides both set and hardening acceleration. But its use is restricted to unreinforced concrete in the UK and in most other countries, due to its potential influence on the corrosion of embedded metal. Calcium nitrate and calcium nitrite are both effective set and hardening accelerators and are widely used commercially. Sodium salts are also effective, but not always acceptable due to the contribution of sodium ions to the overall alkali content of the concrete, causing an Alkali-Silica-Reaction "ASR". Triethanolamine are common accelerators for the  $C_3A$  reactions. The accelerating admixtures increase the rate of hydration of the tricalcium silicate ( $C_3S$ ) and tricalcium aluminate ( $C_3A$ ) phases of the cement. This leads to an earlier heat evolution and strength development. Other materials which work as nucleation seeds yield a faster setting and a high strength gain rate, such as Master X-SEED® commercialized by BASF.

#### 2.4.5 Optimum sulphate level

The optimum content of sulphates affects not only the setting time but also the strength development and the volume stability. The situation is complicated by that the amounts needed to optimize different properties, such as strength at various ages and drying shrinkage, are not necessarily the same. The most important factor is the rate at which the relevant ionic species like calcium sulphate, aluminate, and ferrite phases are made available on the surface of the cement grains. Factors like particle size distribution and the distribution in space are important for the availability. Increasing these factors accelerates the supply of  $Ca^{2+}$  and  $SO_4^{2-}$  ions. An increase in temperature has the same effect. Sulphate ions are also supplied by the clinker, especially as alkali sulphates or calcium langbeinite ( $K_2Ca_2(SO_4)_3$ ). The alkali sulphates provide a highly available source of  $SO_4^{2-}$  at early times. The higher the alkali content, the higher the optimum sulphate content. Furthermore, the

higher the alkali content, the higher the early strength, but the late strength can decrease. Some other properties, such as drying shrinkage, are affected, and the optimum sulphate content is increased. As already mentioned, sulphates have an influence on the dissolution of  $C_3A$ . In the presence of calcium sulphate, the amount of  $C_3A$  hydrated is reduced when compared to that consumed in the absence of sulphate. An excess in sulphate can cause expansion problems due to ettringite formation. The problems arise when ettringite continues to form after the paste matrix transitioned beyond the plastic state into the hardened state. A high sulphate content can lead to excessive ettringite formation, leading to volume instability. An increase in  $SO_3$  content beyond the minimum required can cause a false set. Due to that, a progressive decrease in the shrinkage is observed, which occurs in dry atmospheres, and a progressive increase in the expansion, which occurs in water (Taylor, 1990). The low sulphate content could drive strengths lower by limiting the calcium ions available for the nucleation of CH and C-S-H. Calcium sulphate additions probably affect both the quantities of products that are formed, especially at early stages, and the microstructure at all stages. For any particular clinker source of  $SO_3$ , there is an optimum content for early strength development.

#### **2.4.6 Biocement**

Biocement has demonstrated its effectiveness in enhancing the mechanical properties and durability of cementitious materials. It enhances the compressive strength of such materials by accelerating the calcium carbonate mineralisation in concrete. This calcium carbonate, based on microbiologically induced calcite precipitation (MICP), can fill the voids in concrete, decrease porosity, and improve the particle packing efficiency, thereby making the concrete dense and increasing the compressive strength, as described in the particle packing model.<sup>(52)</sup> Furthermore, MICP creates nucleation centres for calcium silicate hydrate (C-S-H) formation, which accelerates further calcium silicate hydrate formation to increase the compressive strength. Bacterial cell walls may accelerate the carbonation of concrete and alter the carbonation-related physicochemical properties of concrete and thus have the potential to form an admixture of concrete with benefits in enhancing not only mechanical performance but also other carbonation-related concrete properties. Permeation properties have principally been used for comparing the effectiveness of different surface treatments to enhance the durability of concrete. Biocement resulted in a decrease of water absorption and gas permeability as well as resistance to chloride penetration by the deposition of a layer of calcium carbonate on the surface of the specimens and microbial biomass.<sup>(53)</sup> In the case of reinforced concrete structures, MICP facilitates the formation of

a protective passive film around the steel and acts as a corrosion inhibitor by interrupting the transport process in such samples, thus reducing the corrosion rate.(54) Biocement has drawn much attention in recent decades worldwide owing to its eco-friendly nature; however, such research is still limited. The colonization of the entire surface of the stone by carbonate-producing bacteria, which is rapidly coated by the 'biocalcin' was observed.(55) The amino acid composition analysed of organic matrices, associated with calcium carbonate precipitates in microbialites, is built by different Phormidium species (cyanobacteria). Recently, *Sporosarcina pasteurii*, which is a well-known ureolytic bacterium, was used to enhance carbon capture and storage through the solubility- and mineral-trapping of carbon dioxide induced by bacterial ureolysis and carbonate formation. Some profound results for biocement have been obtained by researchers from the USA where a novel process for sand consolidation was developed using bacteria that actively precipitate calcium carbonate as a cementing agent. The results showed a 50% reduction in porosity, and permeability was reduced by up to 90% in the areas where cementation took place. To reduce their porosity, the process of microbiologically induced mineral precipitation can be employed as a method of selective cementation of highly permeable structures in rock formations. Furthermore, the physical and biochemical properties of calcium carbonate ( $\text{CaCO}_3$ ) precipitation induced by *B. pasteurii* (also known as *S. pasteurii*) was examined. The bacterium plugged a sand column based on MICP and contributed to the formation of 30.2% of calcite in the column. Scanning electron microscopy (SEM) results in crystals of distinct calcium carbonate precipitates grown between sand grains depicted along with embedded bacteria. A durability study on concrete beams exposed to alkaline, sulphate, and freeze–thaw environments was studied based on MICP. They quantified MICP by X-ray diffraction (XRD) analysis and visualised it by SEM. There was no development of micro-cracks in the concrete specimens with the bacteria, as they did not expand, quite unlike the control specimens when subjected to alkali-aggregate reactivity, sulphate attack, drying shrinkage, and freeze–thaw. Predominant calcite material was recorded in such specimens by XRD, while rod-shaped impressions, consistent with the dimensions of *B. pasteurii*, were found in the calcite crystals that formed on the surface of the specimens. A substantial cementation in loose sand structures through MICP was established by De Jong et al. Their SEM results verified the formation of a cemented sand matrix with a concentration of precipitated calcite forming bonds at particle–particle contacts, while X-ray compositional mapping confirmed that the observed cement bonds were composed of calcite. Biocement-related research carried out by Chinese researchers is profound, but localised. The major research work has been conducted by Qian and coworkers at the

School of Materials Science and Engineering, Southeast University, Nanjing. Qian probably initiated such research in 2005, when Wang et al. studied the microbiological precipitation of calcium carbonate. Later, Qian et al. investigated the influence of culture concentration, substrate concentration, the inoculation quantity of bacteria, and the crystal formation additive on the precipitation amount and the calcite yield. An innovative sand cementation method of bio-mineral carbonate formation in the sand spacing through urea hydrolysis inspired by microbial urease, was introduced in many studies. The major findings on biocement carried out by the Qian group were summarised by Rong and Qian. They concluded that biocement leads to the cementation of loose particles and restores defects or cracks of cement-based material. Sandstone cement based on MICP developed a high compressive strength and less porosity. The application of biocement is not only restricted to small samples but can also be applied at large scale. Furthermore, biocement can be applied to foundation reinforcement and desertification control. The laboratory results proved that MICP can greatly improve surface permeability resistance and resist the attack of the acid on the surface of cement-based materials by producing a protective layer. Further, results indicated that the calcium carbonate layer obtained under conditions of high bacterial activity, the appropriate concentration of  $\text{Ca}^{2+}$ , and adding  $\text{Ca}^{2+}$  before urea to the reaction mixture, could considerably improve the water penetration resistance of the specimen's surface. These researchers showed the potential of MICP to conserve and consolidate cement-based materials. There have been other reports on calcifying ureolytic bacteria with the potential for biocement formation. However, this group from Xinjiang Institute of Ecology and Geography, Chinese Academy of Sciences, mostly focused on the MICP technique for the remediation of heavy metals. Being of an economic and eco-friendly biomaterial, biocement has a huge potential to improve the durability of building materials, but the real challenge is to convert the results achieved in the laboratory into practical applications. (56)

## 2.5 Potentiometric measurement

### 2.5.1 Potentiometry

Potentiometry is an extremely versatile analytical method which allows rapid and simple analyses. The setup for potentiometric measurements consists of an indicator electrode and a reference electrode. The indicator electrode provides a potential which depends on the composition of the sample solution. The task of the reference electrode is to supply a



potential which is as independent as possible of the sample solution. The measured potential  $U$  is composed of individual potentials produced by the indicator and reference electrodes. Figure 10 shows a schematic representation of the situation using a pH glass electrode with a separate reference electrode. The potentiometric measurement is carried out practically currentless with a voltmeter with a high impedance measuring input. (57)

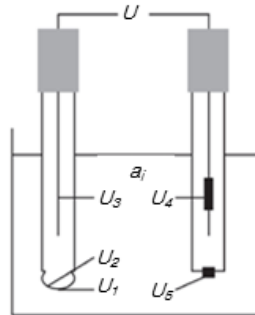


**Figure 11:** Setup for potentiometric measurements with  $U_1$ : Galvani potential of the indicator electrode relative to the sample solution,  $U_2$ : Galvani potential of the reference electrolyte relative to the glass membrane,  $U_3$ : Galvani potential of the internal reference electrode relative to the reference electrolyte,  $U_4$ : Galvani potential of the reference electrode and  $U_5$ : Diffusion potential at the diaphragm.

The individual potentials  $U_2$ ,  $U_3$ , and  $U_4$  are given by the electrode assembly and are thus constant for a specific electrode pair. The diffusion potential at the diaphragm  $U_5$  can be kept more or less constant and small through the use of suitable measures. In this way, that the potential measured between the two electrodes depends only on  $U_1$ , the potential between the indicator electrode and the sample solution. On the other hand, this potential depends on the activity  $a_i$  of the measuring ion. This relationship is described by the Nernst equation:

$$U = U_0 + \frac{2.303 \cdot RT}{z_i \cdot F} \cdot \log(a_i) = U_0 + U_N \cdot \log(a_i) \quad (11)$$

$U$ : Measured potential between indicator and reference electrode

$U_0$ : Standard potential of the measuring assembly, depends on its construction

R: Gas constant ( $8.31441 \text{ JK}^{-1} \text{ mol}^{-1}$ )

T: absolute temperature in K ( $T \text{ in } ^\circ\text{C} + 273.15 \text{ K}$ )

$z_i$ : Charge of measuring ion i (including sign)

F: Faraday constant ( $96\,484.56 \text{ Cmol}^{-1}$ )

$a_i$ : Activity of measuring ion

$U_N$ : Nernst slope

2.303 is the conversion factor for the natural logarithm to base ten.

The Nernst slope  $U_N$  specifies the theoretical electrode slope.  $U_N$  corresponds to the potential change caused by the change in  $a_i$  by the factor of ten. This depends on the

temperature and the charge  $z$  of the measuring ion. It is 59.16 mV at 25 °C for univalent, positively charged ions ( $z = +1$ ).

## 2.5.2 Ion-sensitive electrode

In 1945, Gerold Schwarzenbach discovered that aminocarboxylic acids form stable complexes with metal ions. On the basis of this discovery, he developed the complexometric titration technique, which became increasingly popular from 1950 onwards, particularly for determining water hardness. Soon, in addition to calcium and magnesium, other metal ions could also be titrated. The use of new metal indicators and masking agents also enabled determinations of metal ion mixtures. Nowadays, together with acid/base, redox, and precipitation titrations, complexometric titrations are the most frequently used volumetric methods and are recommended in many international standards and directives. The effective complex formation constants are generally lowered in the presence of protons (acids) because these compete with the metal ions in the reaction with the complexing agent, for example, by protonating the carboxyl group(s). Ion-sensitive electrodes (ISE) have a sensor element which can detect a specific ion in a mixture of ions as selectively as possible. The construction of ion-sensitive electrodes resembles that of pH glass electrodes:

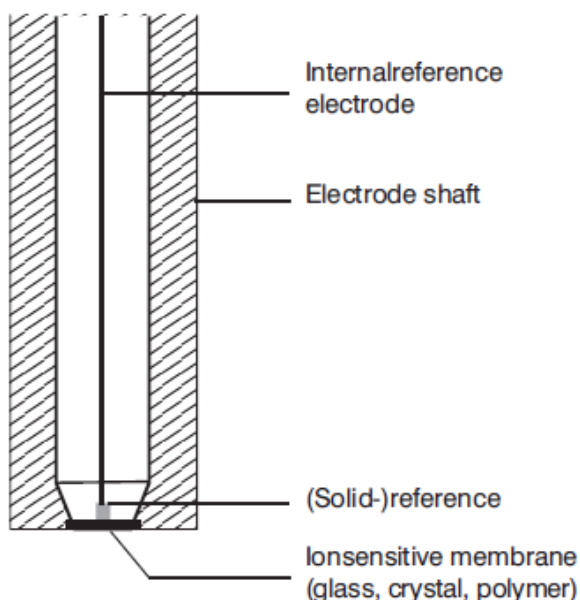


Figure 12. Construction of ion-sensitive electrodes.

At the interface of the ion-sensitive membrane/sample solution, a potential is developed which depends on the activity of the measuring ion in the sample solution. In practice, this is the concentration that is of interest. The activity  $a_i$  is related to the concentration  $c_i$  by:

$$a_i = \gamma_i \cdot c_i \quad (12)$$

with  $\gamma_i$  as the molar activity coefficient. The molar activity coefficient is a function of the total ionic strength of the solution and therefore not easily accessible over time. For very dilute solutions  $\gamma_i$  is approximately 1, i.e. the activity of the measuring ion is equal to its concentration. To make the desired ionic concentration accessible to the analyst through a simple potential measurement, special analysis techniques have been developed that make exact knowledge of the activity coefficient unnecessary: The ionic strength of the sample solution can be kept constant due to the addition of a solution with a high concentration of inert electrolyte. The reference electrode (usually Ag/AgCl) provides an electrode signal (reference potential) that is as independent as possible from the measuring solution. If a suitable measuring setup is used, the potential  $U$  measured between the two electrodes depends only on the measuring solution, or to be more precise, on the activity  $a_i$  of the measuring ion since only dissociated ions are measured. In the case of ISE measurements, this relationship is described by the Nernst equation (11).

## 2.6 Turbidity measurement

A liquid becomes turbid when the refractive index of a clear solvent and a particle in this solvent are different. The turbidity is a subjective perception and is not clearly defined like other physical parameters. In general, the turbidity of solutions is measured *via* scattered light. Common procedures are the 90° scattering and the forward light scatter.

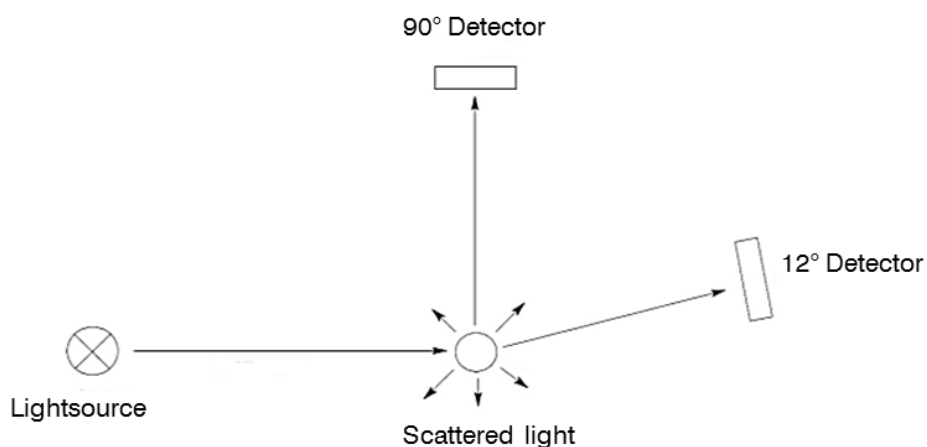


**Figure 13.** Schematic illustration of 90° and forward light scattering measurement.

In both procedures, a beam of light is directed through the solution. The particles in the solution are now scattering the light in all directions. The 90° procedure utilizes a detector at a 90° angle to the ingoing beam of light while the forward scattering procedure utilizes a detector at a 12° angle (III.2). For turbidity measurements, it is important that the used method is named, otherwise, it is impossible to compare or reproduce the results. This is due to that both procedures give different results for turbidity. The 90° scatter measurement, in general, is more sensitive to small particles while the forward scatter method is more sensitive to large particles. The reason for this effect is that small particles are more likely to scatter light at a 90° angle while larger particles scatter the light in a forward direction (Figure 14).<sup>(58)</sup> This effect is used to evaluate the particle size of a given solution by using a combination of both procedures. As an example, the average particle size of a formazine polymer is about 300 nm. In both procedures, the formazine solution developed the same intensity of scattered light. If the readings of the forward scatter detector are higher, then the particle size should be bigger than 300 nm, meaning that higher 90° scatter readings are the result of particles smaller than 300 nm. The turbidity over time is measured by an optical sensor which consists of a light source, two glass fibre (light) guides, a concave mirror and an amplifier. The monochromatic light from the first light guide passes through the solution where it is partially absorbed or scattered by the sample. A potential signal is finally produced in the amplifier and transmitted to the titrator *via* the electrode input.

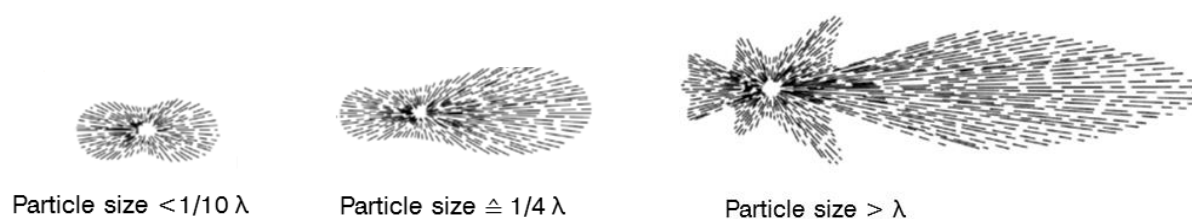


**Figure 14.** Schematic illustration of the light scattering properties of different particle sizes.

In our system, the turbidity is measured as the decrease of potential resulting from light scattering of the formed colourless C-S-H species. The system is a dilute solution with a particle concentration of  $\leq 0.1$  wt-%. The light scattering from dilute solutions is independent of the scattering angle, and the scattering from density fluctuations of the solvent itself is ignored.<sup>(59)</sup> The potential signal only depends on the scattering power of the dissolved particle and the mass concentration. LUDOX colloidal silica solutions (SM-30, AS-

30 and AS-40 by Sigma Aldrich) containing particles of distinctive sizes were analysed to test the lower limits and capabilities of the optical sensor (Figure 15).

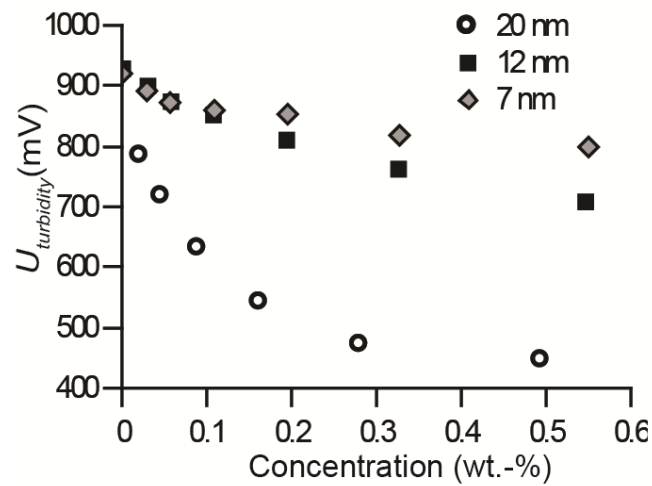


**Figure 15.** The turbidity of colloidal silica solutions over concentration.

A decreasing potential is produced by SM-30, AS-30, and AS-40 with increasing mass concentration. The optical sensor is able to detect colloidal silica particles with a small particle size of 7 nm with a concentration of 0.05 wt.-%. With increasing concentration ( $c > 0.1$  wt.-%), the transmitted intensity is not proportional to the particle mass squared, and the system reaches a region of multiple angle scattering.

## **Nucleation of C-S-H and the impact of polymers**

## 3.1 Nucleation of C-S-H

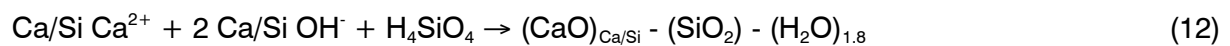
### 3.1.1 Objectives

Cement is the principal component of concrete, which is a ubiquitous material for the construction industry. With an annual consumption of 4 billion tons, this is the most consumed industrial product and is therefore tightly linked to the global economy.<sup>(1)</sup> Modern cement (i.e. Portland cement) is a reactive mixture of calcium silicates, aluminates and sulfates present as several anhydrous polymorphs stabilized by various alkali-metal ions. These phases react with water and form a complex suspension of hydrated amorphous and crystalline phases.<sup>(2)</sup> During the reaction with water (hydration), a percolating network of hydration products develops, which determine the setting and hardening behavior of the material. Despite many decades of intensive research on cement hydration, insight on the early age of this process remains elusive. Detailed understanding of the initial stages of calcium silicate hydrate (C-S-H), the most cohesive phase, is paramount for the development of new additives enabling an improvement of the mechanical performances of concrete and/or a reduction of the cement portion in the next generation of concrete.

The past decade has witnessed major advances in our comprehension of the early stages of crystallization.<sup>(6, 17, 60-68)</sup> Many “non-classical” nucleation pathways, including the formation of precursors, have been proposed to account for the formation of the stable crystalline phase. These multi-step nucleation processes comprise aggregation-based mechanisms of aqueous species ranging from multi-ion complexes to fully formed nanocrystals. The majority of these studies were concerned with proteins <sup>(16)</sup> or minerals of geological and biological interest,<sup>(63)</sup> in particular calcium carbonate. Calcium carbonate polymorphs have been reported to nucleate from aggregation and coalescence of pre-nucleation clusters formed through a liquid-liquid phase separation process.<sup>(68)</sup> These processes are accompanied by dehydration/solidification that eventually leads to mineralization. Similar mechanisms were proposed for other mineral systems <sup>(5)</sup>. Yet so far, systems of industrial relevance have been investigated much less, the only exception being calcium sulfate.

Many studies on calcium silicate hydrate (C-S-H) rely on atomistic simulations,<sup>(69)</sup> but aside from a study by Nonat and coworkers that interprets conductivity results in solution within the framework of the classical nucleation theory (CNT) the early stages of C-S-H formation have not been unraveled. C-S-H belongs to the family of inosilicates, whose structure

is derived from that of natural 14 Å-tobermorite.<sup>(70)</sup> It contains calcium sheets flanked on each side by linear “Dreierketten” silicate chains. The composition of C-S-H, i.e., the calcium to silicon ratio (Ca/Si) and the amount of water molecules, is variable depending on the concentration of calcium hydroxide in solution.<sup>(71)</sup> In regular cement suspensions, the solution is typically close to the solubility limit of Portlandite ( $\text{Ca(OH)}_2$ ,  $c = 23\text{mM}$  at  $23^\circ\text{C}$ ) or slightly supersaturated (up to 33 mM). Under those conditions, the infinite silicate chains of the tobermorite structure are reduced to silicate rows containing silicate dimers, occasionally bridged by a third silicate tetrahedra. Although the overall Ca/Si ratio in C-S-H may vary from 0.66 to 2, its range is restricted to values between 1.4 and 1.7 in cement pastes.<sup>(72)</sup> Disregarding the concomitant dissolution of anhydrous cement phases which are kinetically coupled to the precipitation of hydrates during the hydration of cement in paste,<sup>(73)</sup> the precipitation reaction of C-S-H can be formulated as follows:



$\text{H}_4\text{SiO}_4$  is chosen as silicate species for mass balancing even though the solution contains a mix of  $\text{H}_4\text{SiO}_4$ ,  $\text{H}_3\text{SiO}_4^-$  and  $\text{H}_2\text{SiO}_4^{2-}$ . In ordinary Portland cement, the first remarkable physical transformation, the setting, is mostly due to the precipitation of C-S-H around the cement grains strengthening the percolating network.<sup>(74-76)</sup> The C-S-H nucleation is a crucial step in the hydration kinetics. Indeed, experimental and modelling studies have shown that the crystal growth of C-S-H is strongly limited<sup>(73)</sup> which in turn indicates that the precipitation is driven by nucleation rather than crystal growth. Another facet is that the heterogeneous precipitation of C-S-H into dissolution etch-pits can locally annihilate the dissolution of anhydrous silicate phases as it has been recently proposed and observed.<sup>(77, 78)</sup> Aluminum ions<sup>(79)</sup> and admixtures<sup>(80, 81)</sup> have a negative impact on C-S-H nucleation whereas controlled seeding represents an attractive way to accelerate the evolution of the mechanical properties of cement for industrial applications.<sup>(82)</sup>

Here, we demonstrate that the homogeneous nucleation of C-S-H is a two-step mechanism proceeding *via* amorphous spheroidal intermediates. C-S-H nucleation is clearly heterogeneous under regular operating conditions, even though homogeneous nucleation has been identified in the presence of polycarboxylate ether polymers, typical additives used as fluidifying agents.<sup>126</sup> In order to unravel the underlying elementary steps, the complexity has been reduced by using idealized representative homogeneous conditions, i.e., the formation occurs in solution devoid of particles at typical pH and ionic conditions of cement pastes.



### 3.1.2 Results and Discussion

The homogeneous nucleation of C-S-H was studied from solutions supersaturated with respect to C-S-H and undersaturated (or slightly supersaturated) with respect to Portlandite ( $\text{Ca(OH)}_2$ ). Supersaturation was reached after slow titration of sodium silicate to a lime solution with a custom-designed set-up (fig. S1). Representative conditions of cement solution were approached, i.e., a high pH ( $\text{pH} = 12.6$ ), a calcium concentration close to the solubility of Portlandite ( $[\text{Ca}] = 15 \text{ mM}$ ), a low Si concentration ( $[\text{Si}] \leq 200 \mu\text{M}$ ) and a high ionic strength ( $I = 0.245 \text{ M}$ ). A solution containing  $100 \mu\text{mol/L}$  of Si and  $80 \text{ mmol/L}$  of NaOH was thoroughly characterized and was reported here as reference solution. To prevent carbonation, all solutions were freshly prepared with nitrogen purged deionized water, and the experiments were performed in a closed Teflon vessel under nitrogen. By titration, the solubilized amount of  $\text{CO}_2$  was indeed found to be extremely low (fig. S2). The final product, obtained after 1000 minutes, was characterized by transmission electron microscopy (TEM). The TEM micrograph (Fig. 16A) shows that the product has a foil-like morphology, which was previously reported for the synthesis of C-S-H (47,81) The product was analyzed by nano area electron diffraction (NAED, Fig. 16, B and C). The rotational average from the diffraction pattern has maxima at  $5.3 \text{ nm}^{-1}$  and  $3.2 \text{ nm}^{-1}$ . A periodicity of  $\sim 5.3 \text{ nm}^{-1}$  corresponds to that the expected Ca-O layer repeat distance of C-S-H in the direction of the silicate chains [110] reflection. The broad rings between  $0.31 \text{ nm}$  and  $0.35 \text{ nm}$  demonstrate a distribution of the d-spacing, indicating the presence of strong structural variations between regions of short-range ordering. These results are consistent with the results of previous X-ray diffraction (XRD) studies on C-S-H that revealed the presence of a broad diffuse peak in the range of  $0.25\text{-}0.31 \text{ nm}$ . A comparison of Fig.16B and C reveals that the periodicity of short-range ordering in the diffuse rings varies from region to region. The composition was analyzed by scanning transmission electron microscopy (STEM,) combined with energy dispersive X-ray spectroscopy (EDX, Fig. 16, D and E). The product contains calcium and silicon with a molar ratio of  $1.41 \pm 0.02$  together with minor amounts of sodium ( $2.2 \pm 0.6 \text{ at. \%}$ ) and chloride ( $1.8 \pm 0.9 \text{ at. \%}$ ) ions. The Ca/Si ratio and the  $\zeta$ -potential value of  $+14.50 \pm 0.5 \text{ mV}$  determined by electrophoresis match the value expected from the synthesis of C-S-H for such calcium hydroxide concentrations. (82, 83) This information is in accordance with the precipitation of  $\beta\text{-C-S-H}$ , according to the thermodynamic model developed by Haas and Nonat in which the negative surface charges are overcompensated by calcium ions.

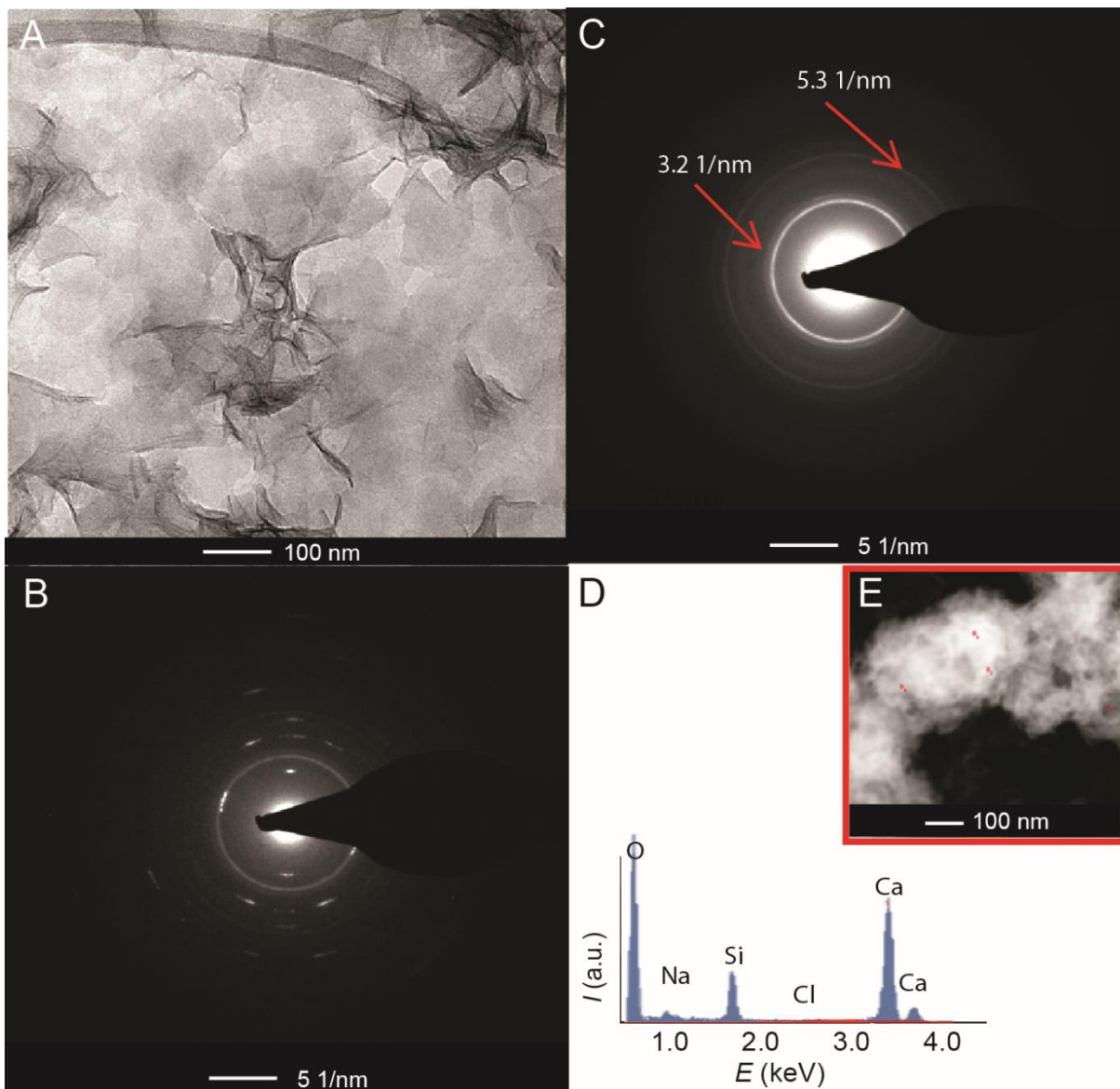


**Figure 16. Characterization of the final reaction product. (A)** TEM micrograph of the collected solid phase. **(B, C)** NAED pattern of the final product. **(D)** STEM EDX spectrum and **(E)** area from which the EDX pattern was recorded.

The physico-chemical evolution of the suspension during C-S-H nucleation was monitored by turbidimetry and pH measurements (Fig. 17A). The concentration of Si and Ca was obtained through the analysis of supernatants by inductively coupled plasma optical emission spectrometry (ICP-OES) (Fig. 17B). The concentrations allow the calculation of  $\beta$  the ratio of the ion activity product to the solubility product with respect to  $\beta$ -C-S-H and Portlandite, i.e., the degrees of supersaturation (Fig. 17C). The nucleation process has been divided into three main stages according to the characteristic evolution of the turbidity (Fig.17A) which shows that clear start solutions ( $U_{turb} = 800$  mV) are getting more turbid in two steps (drops of  $U_{turb}$  in stages I and III).

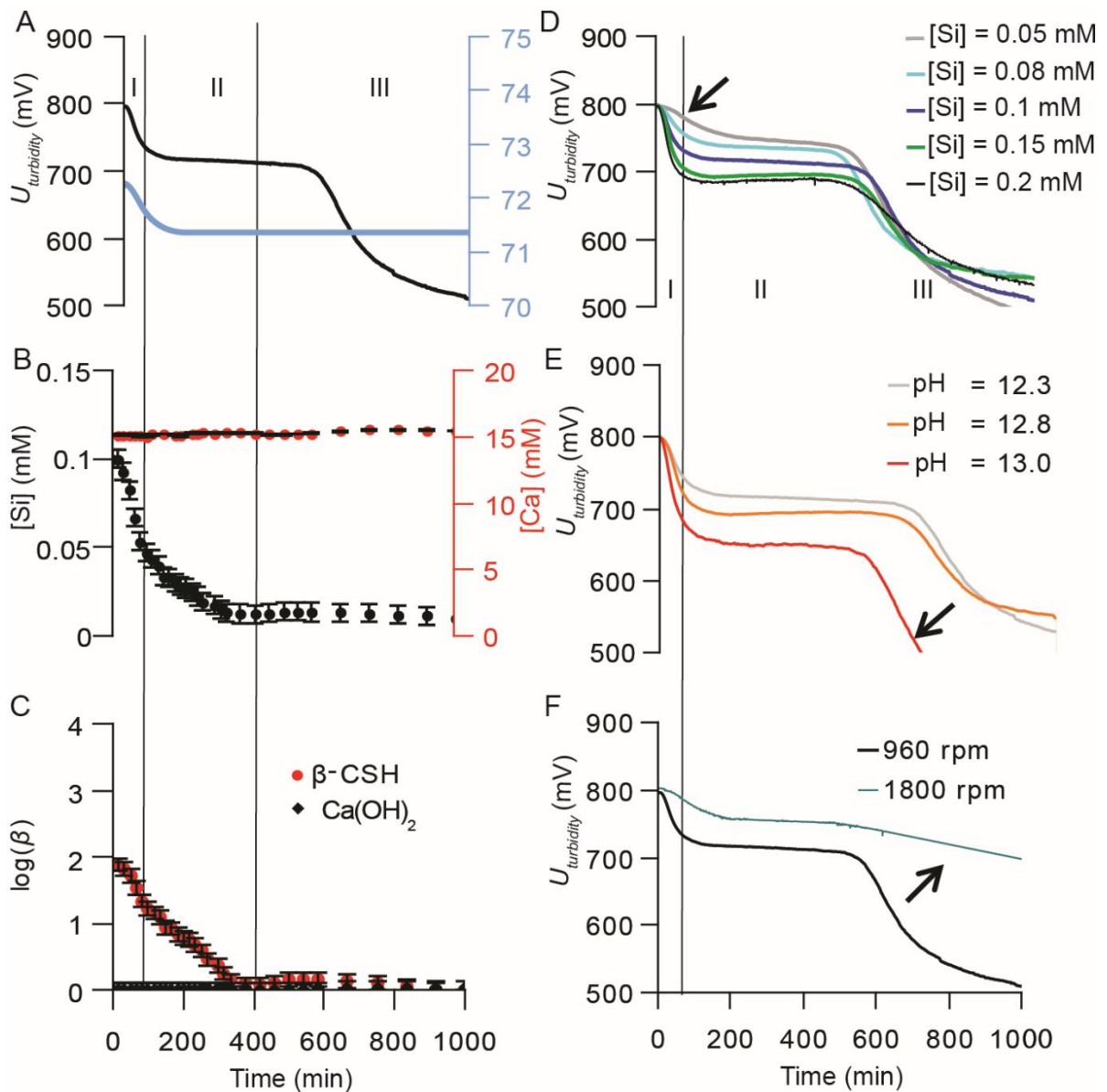


**Figure 17. Evolution of the turbidity and solution concentrations.** (A, B, C) show results related to the reference experiment containing 100  $\mu\text{mol/L}$  of Si and 80 mmol/L of NaOH: (A) Time evolution of the turbidity (black) and the activity of hydroxide (blue). (B) the  $[Si]$  and  $[Ca]$  concentrations (mean values averaged over three experiments) analyzed by ICP-OES. (C) Evolution of the supersaturation ( $\beta$ ) with respect to C-S-H and  $Ca(OH)_2$  solubilities calculated from the solution concentrations. Evolution of the turbidity for various conditions: at different silicate concentrations (D), different pH values (E) and different stirring speeds (F) as a function of time. The standard deviation of the turbidity potential is below 5 mV.

The drops of the turbidity and the hydroxide ion activity coincide during stage I. Unlike the turbidity the pH shows only a significant change in stage I and no change during stage III (Fig. 17A). The silicate concentration drops from 0.10 to 0.04 mM during stage I and II (Fig. 17B). The calcium concentration remained fairly constant because it is the two orders higher of magnitude than the other concentrations from the beginning. The evolutions of silicate concentration, pH and turbidity are well correlated during stages I and II. After addition of

the sodium silicate solution the system is supersaturated with respect to  $\beta$ -C-S-H (Fig. 17C). The silicate concentration decreases rapidly during stages I and II and more slowly afterwards. The solubility equilibrium was almost reached at the end of stage II within the accuracy of measurement ( $\sim 4 \mu\text{mol/L}$  in Si), although the calculations indicate a low undersaturation with respect to  $\beta$ -C-S-H at the end of the experiment. The supersaturation index ( $\log \beta$ ) with respect to Portlandite is close to zero, and no Portlandite formation was detected by IR spectroscopy (fig.A4). As no abrupt change in chemical composition was observed in stage III, secondary precipitation of other solids like calcium carbonate can be excluded. The silicate concentration ( $[\text{Si}] = 50\text{-}200 \mu\text{mol/L}$ ) was varied in order to change the supersaturation with regard to  $\beta$ -C-S-H in the starting solution. The supersaturation affects the drop of  $U_{\text{turb}}$  in stage I: the higher the supersaturation, the earlier and the sharper the drop. The turbidity in stage II and III is independent of the silicate concentration. This indicates that the second  $U_{\text{turb}}$  drop is not directly linked to the supersaturation (Fig. 17D). An increase in pH accelerates the first and the second  $U_{\text{turb}}$  drops (Fig. 17E). When increasing the pH to 13.0, the final C-S-H product was indeed formed after only 600 minutes. The higher pH increased the supersaturation with respect to  $\beta$ -C-S-H and the deprotonation of the silanol groups, i.e., the charge density of the silicate chains in C-S-H. An increase in stirring speed (Fig. 17F) retarded the  $U_{\text{turb}}$  drop in stage II and III. The stirring speed, e.g. the rate of mass transport (diffusion, convection, shear force, etc.) affects the production/consumption dynamic of the forming material. C-S-H formation is highly sensitive to the experimental parameters as the supersaturation of the system and the stirring.

Size and morphology of the objects formed in the supersaturated reference solution (Fig. 18A) were obtained from dynamic and static light scattering (DLS, SLS) measurements carried out on samples collected and transferred into dedicated cuvettes. Objects with a hydrodynamic radius ( $R_{H,app}$ ) of  $\sim 60 \text{ nm} \pm 3 \text{ nm}$  were detected already at the very first stage of the measurement, which indicates that they were formed right after silicate addition i.e. during the 5 minutes prior to the first DLS acquisition. The particle size was independent of the incidence angle (35), which indicates that the particle size distribution is fairly narrow.  $R_{H,app}$  increases linearly from 60 to 90 nm during the next 60 min (Fig. 18A). After the first 60 minutes no further increase of  $R_{H,app}$  was observed during stage I. Fig. 3B displays  $R_g$  the gyration radius calculated from SLS measurements, as a function of time. The Guinier plots show a linear correlation yielding  $R_g = 70 \pm 3 \text{ nm}$  (fig.A5). According to the SLS experiments, a change of the silicate concentration from 50 to 200  $\mu\text{M}$  had no effect on  $R_g$  in stage II (fig. A5). Thus, the  $U_{\text{turb}}$  drop in stage II with increasing silicate concentration is

caused by a higher amount of scattering particles (Fig. 18D), suggesting that particle formation is fast compared to their growth. Whereas a higher silicate concentration in stage I and II leads to a higher number of spheroids, it is possible that the first  $U_{\text{urb.}}$  drop is associated to the time needed to reach the detection limit. The structure parameter  $\rho$  ( $R_g/R_{H,\text{app}}$ ) was found to be 0.77, indicating that the objects are fairly spherical (35). No morphological changes were detected by SLS for the next four hours (Fig. 18B).

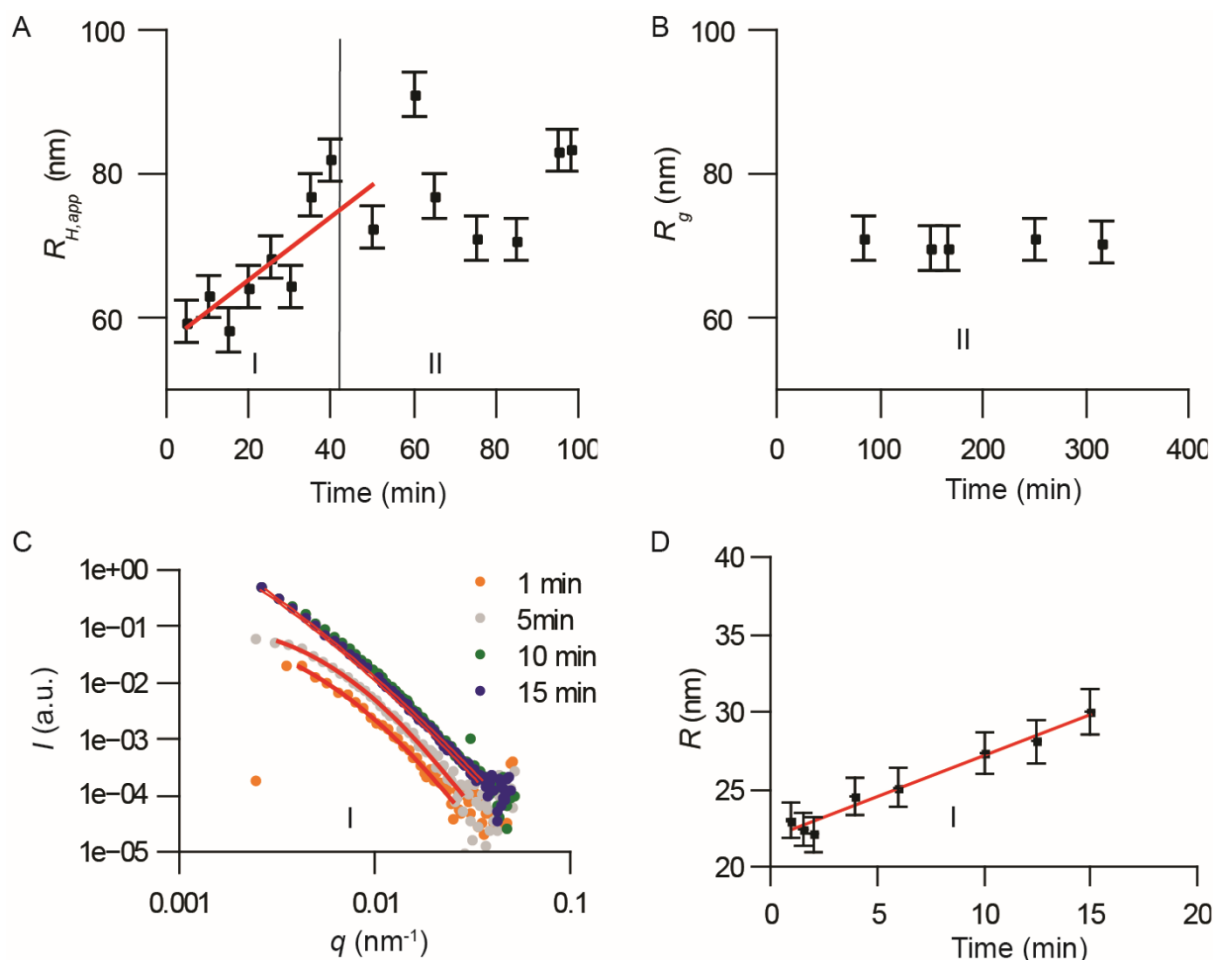


**Figure 18. Light and synchrotron X-ray scattering analysis of the supersaturated reference solution.** (A) Hydrodynamic radius determined by DLS at three different angles during the first 5 to 100 minutes. (B) Evolution of the gyration radius calculated from the Guinier plot ( $\ln I_q$  over  $q^2$ ) obtained by SLS during stages I and II (400 minutes). (C) Time resolved *in situ* SAXS pattern during the first 15 min. The formation of small primary entities/scatterers is shown through the increase in intensity with the fits of scattering curves (red). (D) Radius evolution resulting from the fits of scattering curves (size distribution represented by the error bars).

The DLS measurements required the transfer of the supersaturated solution into a cuvette and thus did not allow any stirring. In order to circumvent this problem and to monitor the size evolution of the objects from the very first minute, the early stages of the reaction were investigated by small angle X-ray scattering (SAXS) with synchrotron radiation using the

same titration set-up, where a circulation loop powered by a peristaltic pump and connected to a capillary allowed this *in situ* analysis. Fig. 3C reveals that the first objects are detected within the first two minutes and continue to grow linearly (Fig. 18D). The scattering curves were fitted assuming spherical particles obeying a log-normal size distribution. Fig. 18C represents the radius evolution of these spherical objects during the first 15 minutes. The radius of the first particles determined by SAXS ( $\sim 22$  nm) is significantly lower than that from DLS ( $\sim 60$  nm), although their growth over time is similar (0.55 and 0.44 nm/min). This difference in particle size might be attributed to the effect of stirring.

Cryo-TEM investigations performed 300 min after the addition of the silicate solution (Fig. 19A and fig. A7) confirmed the presence of spherical particles at this stage with a radius of about  $32 \pm 9$  nm, close to that obtained by SAXS. These objects appear to be predominantly non-crystalline in stage II. No maximum in the NAED pattern is observed (Fig. 19B) which means that the particles are non-crystalline. Ca and Si contents of  $40.2 \pm 0.5$  and  $35.2 \pm 0.8$  at.-% determined by STEM EDX (Fig. 19C) yielded a Ca/Si ratio of  $1.13 \pm 0.33$ . The objects also contained sodium ( $19.7 \pm 0.2$  at.-%) and chloride ( $5.3 \pm 0.8$  at.-%), yielding a Ca/Na ratio of 2. Yet, a few particles already show crystalline features (circled particle in Fig. 19A), which can readily be identified after 600 min. Irregular fringes inside the spheroids indicate some medium-range order (Fig. 19D). Fig. 4 shows that the spheroids transform into an ordered structure with layers spaced by  $1.36 \pm 0.3$  nm. The morphology and chemical composition of the spheroids support the formation of an amorphous C-S-H intermediate during stage I that transforms into a crystalline product that matches the  $14 \text{ \AA}$  tobermorite-type structural periodicity.<sup>(83)</sup> The presence of sodium and chloride ions contrasts with the composition of the final reaction product, indicating that sodium and chloride are expelled during stage II. At the same time, the Ca/Si ratio increased from 1.13 to 1.41 can be explained by a Na/Ca cationic exchange rather than by depletion in Si as the [Si] decrease is completed in the middle of stage II.

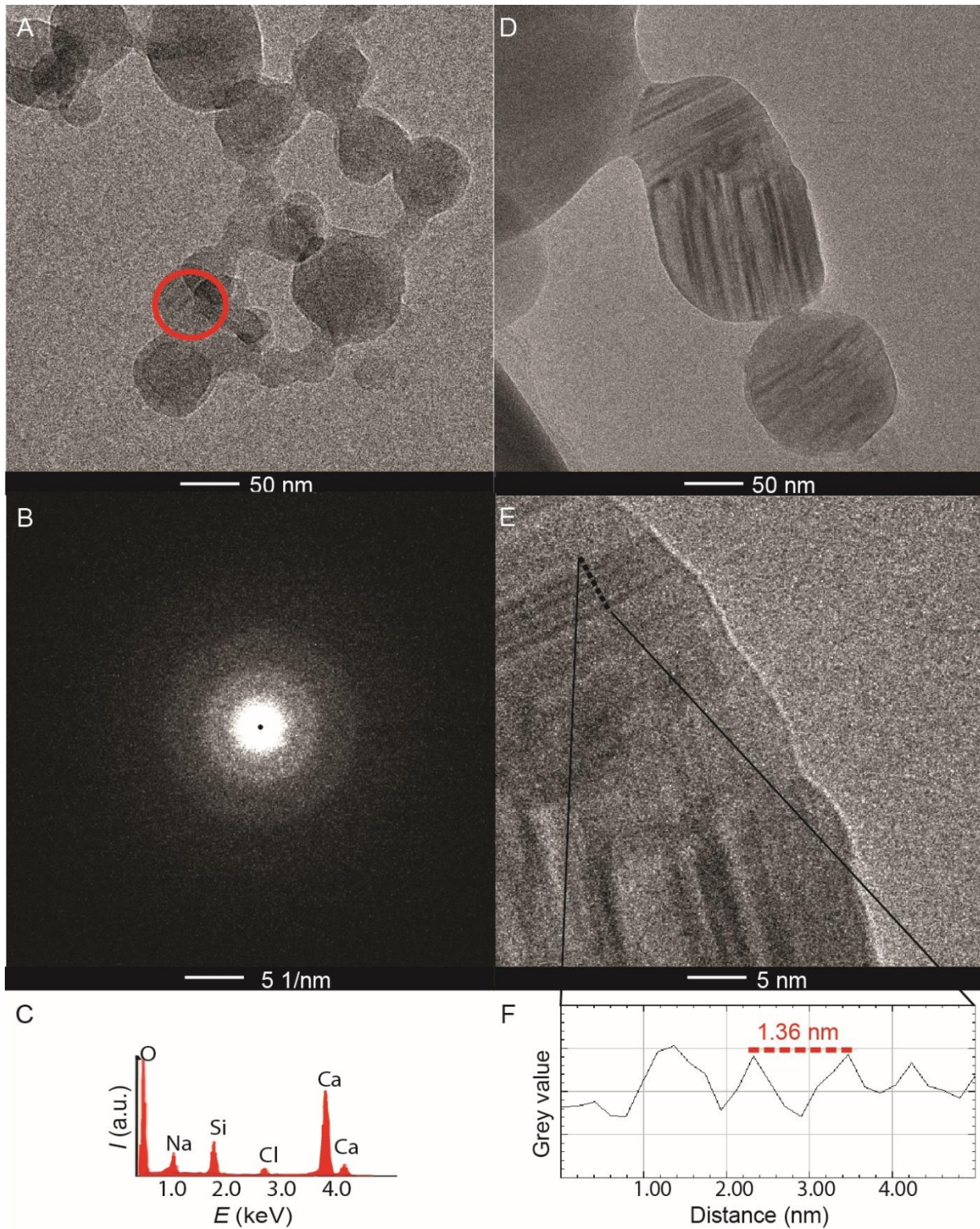


**Figure 19. C-S-H crystallization from the reference supersaturated solution observed by Cryo-TEM, NAED and STEM EDX. (A)** Cryo-TEM image of the suspended particles 300 min after addition of the silicate solution. **(B)** NAED pattern of the spheroid after 300 min **(C)** STEM EDX spectrum of the spheroid after 300 min. **(D)** Cryo-TEM image of the suspension and **(E)** high resolution image after 600 min. **(F)** Profile plot along the back dotted line shown in high resolution image **(E)** of the particles formed after 600 min in solution.

The experimental Ca/Si ratio (1.41) and the  $\zeta$ -potential (+14.5 mV) correspond to  $\beta$ -C-S-H at equilibrium according to the model of Nonat and Haas (85) which predicts a theoretical Ca/Si ratio of 1.45 and a surface potential of +8 mV. The final  $\beta$ -C-S-H product theoretically contains 93% of silicate dimers. A charge balance calculation shows that the speciation in spheroids, based on the composition obtained by STEM/EDX, is very similar to that of  $\beta$ -C-S-H. The apparent negative charge deficit inside the spheroids may be explained by the presence of 72-100% of fully deprotonated silicate dimers (table A.6). By modeling the electrostatic interactions in the framework of the primitive model, the composition allows to calculate the silicate dimer density associated with the Ca/Na ratio of 1.41 at equilibrium. The modeling results indicate that the density with respect to silicate inside the spheroids is  $\sim 19$  times lower than in final C-S-H (fig. A.5A). The significantly lower silicate density inside the spheroids compared to C-S-H indicates that the transformation of the calcium silicate spheroids into final  $\beta$ -C-S-H is accompanied by a densification, i.e. water molecules are expelled. This densification yields a variation of the surface charge density ( $\sigma$ ) which in turn has to drive the colloidal stability of the system (Fig. 20B). In contrast to the strong attractive forces between highly charged ( $\sigma = -4 \text{ e/nm}^2$ ) C-S-H platelets resulting from strong ion-ion correlation forces, (86) the low charge density in the spheroids ( $\sigma = -0.6 \text{ e/nm}^2$ ) prevents them from aggregating because repulsive forces predominate.



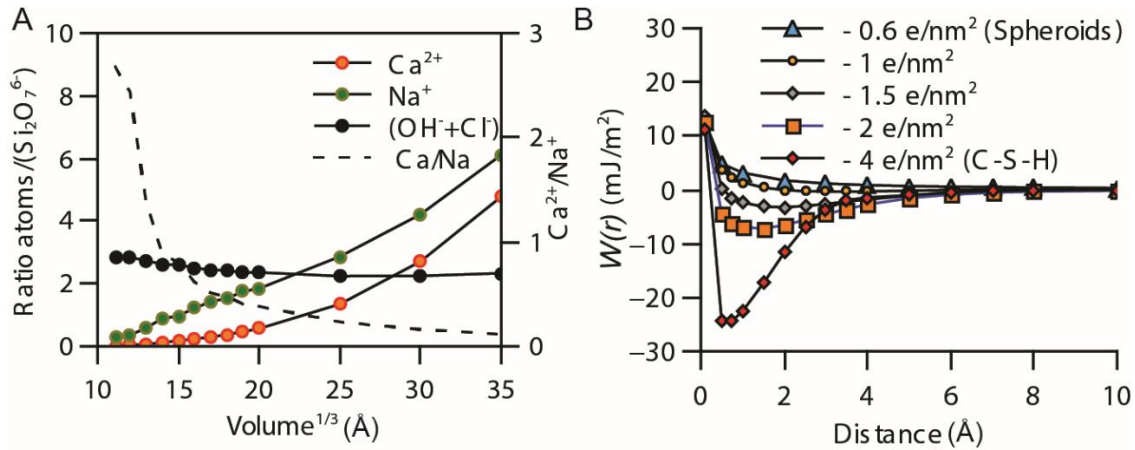


**Figure 20. Modeling results. (A)** Simulations of the average number of  $\text{Ca}^{2+}$ ,  $\text{Na}^+$  and anions ( $\text{OH}^-$  and  $\text{Cl}^-$ ) per silicate dimer ( $\text{Si}_2\text{O}_7^{6-}$ ) as a function of the volume of the cubic simulation box. The simulations are performed in the semi-grand canonical ensemble with one silicate dimer per box. The volume of the box is therefore proportional to the density in silicate dimers in the spheroids. The ions excepted the silicate dimer are allowed to move in and out of the simulation box according to their set chemical potential, i.e. they are in equilibrium with the bulk solution. A  $\text{Ca}^{2+}/\text{Na}^+$  ratio of 2 corresponds to a volume of  $16^3 \text{ \AA}^3$ . In C-S-H, this volume corresponds to  $6^3 \text{ \AA}^3$ , and the surface charge density is  $-4 \text{ e}/\text{nm}^2$ . Thus, the spheroids are, the spheroids are approximatively  $(16/6)^3 = 19$  times less dense than C-S-H and their surface is  $(16/6)^2 = 7$  times less charged. **(B)** Interaction surface free energy ( $W(r)$ ) curves as a function of the distance between two negatively charged infinite plates (see Fig. A8), for different charge densities. A charge of  $-0.6 \text{ e}/\text{nm}^2$  corresponds to the surface charge density of the spheroids as calculated in (A). A charge of  $-4 \text{ e}/\text{nm}^2$  matches the surface charge density of C-S-H. The interaction is purely repulsive at low charge density and becomes attractive at  $-1 \text{ e}/\text{nm}^2$ .

### 3.1.3 Conclusion and outlook

**Chemical reaction model.** The combined experimental and theoretical results from scattering, STEM EDX, cryo-TEM and modelling allow to sketch a physico-chemical model for the nucleation of C-S-H, characterized by two turbidity drops that appear to be the consequence of two well-defined chemical steps. The first turbidity step corresponds to the formation of  $\sim 50 \pm 10 \text{ nm}$  sized amorphous calcium silicate spheroids. These amorphous spheroids have a composition compatible with the C-S-H chemistry, but they are depleted in calcium compared to the final equilibrium state. These amorphous particles form rapidly after addition of silicate to a calcium hydroxide solution, but they do not form in the absence of calcium (fig. A6).  $\text{Ca}^{2+}$  is known to catalyze the oligomerization of silicates ions. (87) Yet, as the pH in this study is high and the silicate concentration low, oligomerization is clearly disfavored. In addition, a decrease of the starting pH shifts the first  $U_{\text{turb}}$  drop to later times (Fig. 18E). Consequently, the spheroid formation is not directly associated with the formation of Si-O-Si bonds, and increasing pH and  $[\text{Si}]$  will only result in higher

supersaturations. Furthermore, the solution (based on the Si speciation) approaches the solubility concentration of C-S-H already during stage II, i.e., the chemical potentials of the species in the spheroids and in C-S-H are similar. Thus, it is reasonable to assume that the spheroid formation is triggered by similar molecular calcium-silicate interactions as in crystalline C-S-H. However, the amorphous and crystalline C-S-H phases differ in their density as revealed by the different contrast between the TEM images of the spheroids and the crystallizing C-S-H phase and by the different Ca/Na ratios as shown by the charge modeling (Fig. 20A). The low silicate (i.e. charge) density inside the spheroids ensures their colloidal stability and explains their existence as dispersed particles on long-time scales. A low density contributes to faster relaxation, rotation of silicate polyhedra inside the intermediate spheroids and to the distortion of bond lengths and angles (86) in order to accommodate the species into the crystalline C-S-H structure.

**Second chemical step.** The well-defined diffraction rings in cryo-TEM SAED indicate the appearance of crystalline order related to C-S-H during stages II and III. In contrast to the first step, the initial silicate concentration does not affect the time of the second  $U_{turb}$  drop. Moreover, the solution is already close to the solubility equilibrium of C-S-H before the ordering process. Therefore, the second step appears not to be directly driven by the deviation from the C-S-H solubility equilibrium. As the crystallization starts in stage II and particles seem to be dispersed in stage II but aggregated in stage III, the second increase in turbidity is likely the result of the concomitant transformation of spheroids into  $\beta$ -C-S-H and the aggregation of  $\beta$ -C-S-H crystallites. Based on electrostatic considerations, the sodium and calcium ions are bound to the silicate tetrahedra. The formation of an ordered arrangement leads to an alignment of the silicate layers and is likely to be associated with a release of water molecules and a concomitant densification inside the spheroids, which, in turn, would favor Ca adsorption.(87) The crystallization is therefore accompanied by an exchange of sodium against calcium ions. As supported by the modelling, this progressive densification is linked directly to an increase of the surface charge density and leads to an aggregation of the spheroids (Fig. 20B). It turns out that the onset of aggregation seems to be rather the consequence of the crystalline ordering. As further support, higher pH accelerates the second  $U_{turb}$  drop (Fig. 18E). This can be linked to a higher deprotonation of silanol groups, i.e., a higher charge density of the silicate chains in C-S-H as the electrostatic interactions increase with pH. If density fluctuations were assumed to be the main kinetic factor driving crystallization inside the spheroids (65) high attractive forces between calcium silicate entities might indeed promote a higher local density of species and thus statically accelerate the transformation into crystals. The formation of amorphous

intermediates is often observed in sol-gel processing of ceramics and typically the initial formation of poorly crystalline intermediates from dissolved species is more exothermic than the crystallization into a hydrous crystalline phase.<sup>(88, 89)</sup> This latter accompanied by the release of water molecules is indeed lowly exothermic or even endothermic but the process then becomes a purely entropy-driven reaction, and finally, it leads to more dense compounds. This higher density in charged species goes hand in hand with final stronger attractive interactions between these crystallizing objects and faster aggregation. The two-step mechanism of the homogeneous nucleation of C-S-H is sketched in Fig. 21.

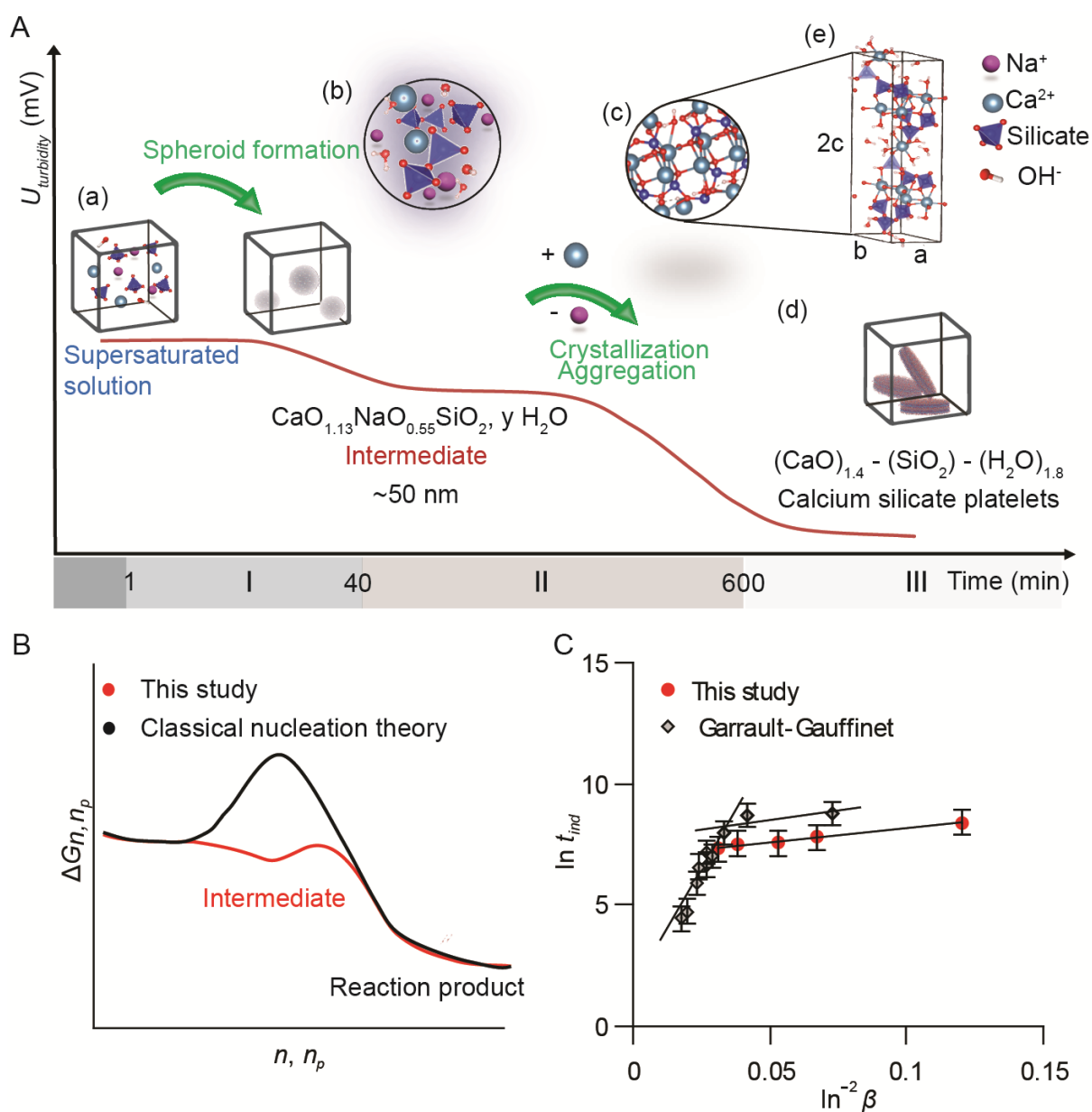


**Figure 21. Two-step pathway theory versus classical nucleation theory (CNT).** (A) Evolution of the turbidity (red curve) with the different species emerging along the reaction the path: (a) Supersaturated solution, (b) liquid amorphous intermediate, (c) crystalline domains and (d) final  $\beta$ -C-S-H platelets. (e) Model of C-S-H structure represented by 14 Å tobermorite. Reprinted with permission from ref. 104. Copyright 2017 American Chemical Society. The first chemical step, defined by the first  $U_{turb}$  drop in stage I, is the formation of liquid amorphous intermediates rich in silicate dimers and calcium. The intermediate has a composition in silicate and calcium similar to that of  $\beta$ -C-S-H with additional sodium ions and water molecules. The second step encompasses a Ca/Na exchange (stage II to stage III) resulting in the formation of  $\beta$ -C-S-H crystallites which aggregate and give rise to the second  $U_{turb}$  drop. (B) Tentative free energy profiles showcasing the two-step mechanism observed in this study (red line) compared to classical nucleation (black line). (C) Typical plot in the framework of the CNT used for the calculation of the energy penalty (interfacial energy) to form a solid phase from supersaturated solution.

**Two-step nucleation vs. the one-step model from the classical nucleation theory.** Our results describe the formation of C-S-H crystalline particles through a two-step mechanism which differs fundamentally from a model based on conductometric studies by Garrault-Gauffinet that suggesting the direct nucleation of C-S-H nuclei.<sup>(4)</sup> An apparent induction time,  $t_{ind}$ , could also be assigned to the first  $U_{turb}$  drop in our study, and a deviation from equilibrium can be calculated from the initial conditions taking into account  $\beta$ -C-S-H as equilibrium phase. Based on the classical nucleation theory  $t_{ind}$  is linked to the supersaturation by

$$\ln t_{ind} = \frac{fV \Omega^2}{(kT)^3 \ln^2 \beta} \quad (13)$$

where  $V$ ,  $\Omega$  and  $f$  are respectively the molar volume, the surface energy, and the shape factor, and  $T$ ,  $\beta$  and  $k$  are the temperature (298 K), the supersaturation, and the kinetic constant.<sup>(90)</sup> Fig. 21C highlights that the evolution of  $\ln t_{ind}$  is proportional to  $\ln^2 \beta$ , which indicates that the sole formation of spheroids could be also described within the framework of the classical nucleation theory from an energy point of view. Still, this plot is not sufficient to elaborate the chemical path. We demonstrate that the formation of the nuclei involves, at least, an amorphous intermediate. Garrault-Gauffinet's data (Fig. 21C), however, highlight two supersaturation domains in each of which a linear dependency with  $\ln^2 \beta$  was observed. Without other experimental evidence, Garrault-Gauffinet assumed a switch between heterogeneous (low  $\beta$ ) and homogeneous (high  $\beta$ ) nucleation processes. Regardless of any consideration on the geometry and nature of the forming objects, the plot also indicates that the energy penalty to form the amorphous spheroids is significantly lower than Garrault-Gauffinet's data at high  $\beta$  but matches the data at low  $\beta$ . As suggested by Navrotsky <sup>(91)</sup>, low interfacial surface energy is the key to explain the occurrence of intermediate phases in crystallization processes which may be thermodynamically or kinetically preferred for small particle sizes. The switch observed by Garrault-Gauffinet could thus result from the change between amorphous intermediate-driven and crystalline phase-driven formations. In that case, the amorphous intermediate could only be observed when the transition kinetics is slow, i.e., from low to moderate supersaturations. We demonstrated the key role of aggregation during the transformation of spheroids into a crystalline product and it has been shown elsewhere that the aggregation lowers the overall energy of the system <sup>(92)</sup> and also allows a rapid propagation of the chemical transformation due to the percolating character of the aggregates.<sup>(93)</sup> It is evident that the aggregation is favored at high concentration of spheroids, i.e., at high supersaturations. The energy transition could be simply due to

statically low aggregation at low supersaturations which in turn would enable the observation of these transient amorphous spheroids.

The nucleation of very few minerals have been thoroughly investigated and rationalized based on complex models. This study shows that C-S-H nuclei are formed in two distinct steps that can be differentiated by their crystalline order, their calcium contents and their density. However, it is unknown whether the amorphous spheroids are a requirement for C-S-H formation in real cement pastes. As a matter of fact, their amount and dispersion state would be crucial for building up the C-S-H network structure. Along this path we demonstrated, how advection influences spheroid formation and it may be correlated to the effect of mixing during the early hydration of cement. (94) The stabilization of spheroids by polymers may be at the origin of the frequent and adverse retardation observed with the use of the polycarboxylate ether superplasticizers. As a support, Valentini et al. (95) proposed that C-S-H nucleation switches from heterogeneous to homogeneous in the presence of superplasticizers, and Nicoleau (81) used similar polymers to stabilize single C-S-H particles. Aluminum ions were reported to distort the local ordering in C-S-H. (96) This may be an explanation for a longer or more difficult crystallization of the spheroids into C-S-H in the presence of aluminum and the known poisoning effect of aluminum during the early stage of cement hydration.

A fundamental understanding of the mechanism of C-S-H formation at a molecular level is essential for a rational design of novel, cement-based construction materials. The implication is a novel perspective and opportunity for “designing” the hydration process and the materials properties. Our study indicates how the evolution of the chemical composition may become a handle for a scientifically guided material design of cements and hydrated nanocomposites.

## 3.2 Influence of polymers

### 3.2.1 Objectives

When discussing the influence of organic or inorganic additives on crystallization mechanisms, the classical approach of considering adsorption of these molecules to crystal growth surface still prevails where the additives are assumed to affect growth rate and crystal habit. Naka et al. observed that vaterite, which is a less stable polymorph of  $\text{CaCO}_3$ , is stabilized by the addition of polyacrylic acid either in a spherulitic or nanoparticulate form, depending on the moment when the polymer interferes with the crystallization. (97) Wang et al. proposed a mechanism based on the assumption of mesocrystals in order to explain peculiar shapes of  $\text{CaCO}_3$  crystals that crystallized in the presence of polystyrene sulfonate. (98) The polymer affected the process by complexing ions, by nucleating, by stabilizing the intermediate amorphous particles, and by controlling the assembly of so-called mesocrystals. Rather similar experiments were done by Gebauer. (6) The effect of various peptides on the nucleation of  $\text{CaCO}_3$  was analysed, and it has been proven that titration in combination with ion-selective electrodes is a powerful method to shed light on the formation mechanism of  $\text{CaCO}_3$  at very early stages, eventually leading to the acceptance of the pre-nucleation cluster theory. (99) As the setting of cement is due to ionic correlation forces between highly negatively charged C-S-H nanoparticles throughout a calcium-rich solution, a way to enlarge the attraction range between C-S-H particles is to add cationic oligomers that compete with calcium ions modifying the ionic correlation forces *via* a bridging mechanism of longer range. There, results demonstrated that cationic oligomers can compete with calcium cations as counterions to the C-S-H surface. They used commercially available unmethylated substances as diaminopropane and nor-Spermidine. In addition to these studies, A. Picker (100) analysed the ongoing processes in a calcium silicate formation model system. This was done with the help of titration experiments and parallel monitoring of ion concentrations with ion-selective electrodes with polyDADMAC. In the course of this study, a calcium chloride solution is titrated into a silicate solution of high pH. This is in contrast to the previously used system (2.1.), and the system is not supersaturated with regard to C-S-H. The inversion of the system enables us to monitor the change in free calcium in solution over time during the formation process. The aim of this part is to provide a better understanding of the interaction between free calcium ions and the silicate species in solution. Furthermore, the influence of well-known cement hydration admixtures as sugars and cationic polymers like quarternized Vinylimidazole and Vinylpyrrolidone on the nucleation process were analysed.

### 3.2.2 Data evaluation

The experimental setup is described in 2.1 (for more detail see A1). A typical titration curve is shown in Figure 22.

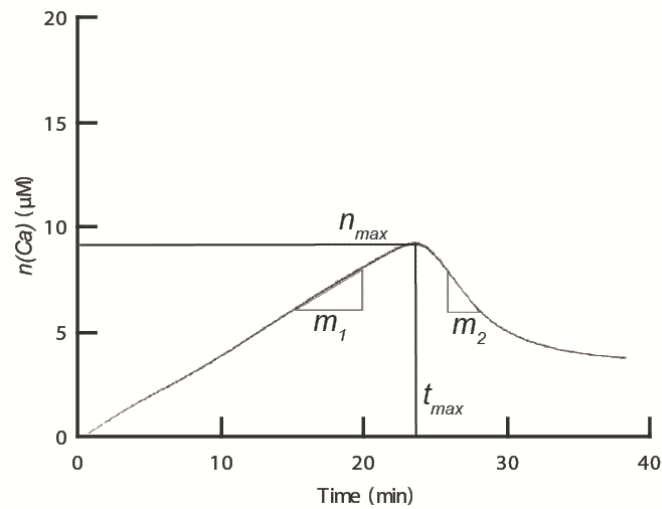


**Figure 22.** Titration curve.

The maximum of the titration curve is assigned at the time of the nucleation point ( $t_{max}$ ) and the amount of free calcium in solution ( $n_{max}$ ). The slope  $m_1$  is evaluated as the pre-nucleation slope, providing information about the amount of bound calcium by silicates. The post-nucleation slope  $m_2$  is a key indicator for the decrease of free calcium ions in solution after the maximum and provides some insight about the early nucleation and growth rates.



### 3.2.3 Results and discussion

The first series of experiments investigated the influence of the stirring speed and dosing speed. During the experiment,  $\text{CaCl}_2$  is constantly added to the solution of sodium silicate, leading to a constant slope  $m_7$  over time. Once the maximum is reached, a subsequent drop was monitored, which indicates the consumption of calcium ions due to a calcium silicate formation process (Figure 23).

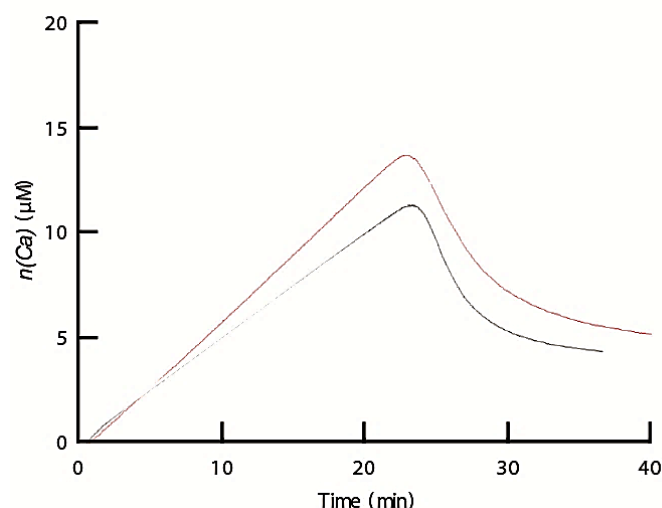


**Figure 23.** Titration curves at pH 13.6 ( $[\text{Na}_2\text{SiO}_3] = 6.6 \text{ mM}$ ,  $[\text{CaCl}_2] = 30 \text{ mM}$ ) with a stirring speed of 8 (black) and 15 (red).

As can be seen from Figure 23, an increase in stirring speed shifts the nucleation point to a higher amount of free calcium in the solution. The increase in slope before the nucleation point indicates a lower calcium consumption and binding by the silicate species. Higher silicate oligomers bind calcium ions more efficiently than shorter ones. (100) According to that, a lower calcium consumption indicates an influence of the stirring speed on the degree of structuring the silicate chains and the structuring of the rather unordered primary nucleated particles. To analyse the dosing speed, equivalent volumes of  $\text{CaCl}_2$  were added at 0.01 mL/min, 0.02 mL/min and 0.04 mL/min. The titration curves are shown in Figure 24 and Figure 25.

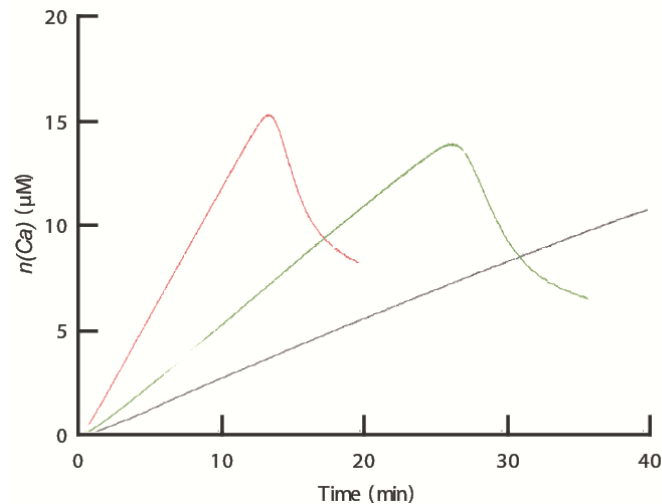


**Figure 24.** Titration curves at pH 13.6 ( $[\text{Na}_2\text{SiO}_3] = 6.6 \text{ mM}$ ,  $[\text{CaCl}_2] = 30 \text{ mM}$ ) with a dosing speed for  $\text{CaCl}_2$  of 0.04 mL/min (red), 0.02 mL/min (green) and 0.01 mL/min (black).

In Figure 25, the titration curves are plotted against the dosed amount of calcium.

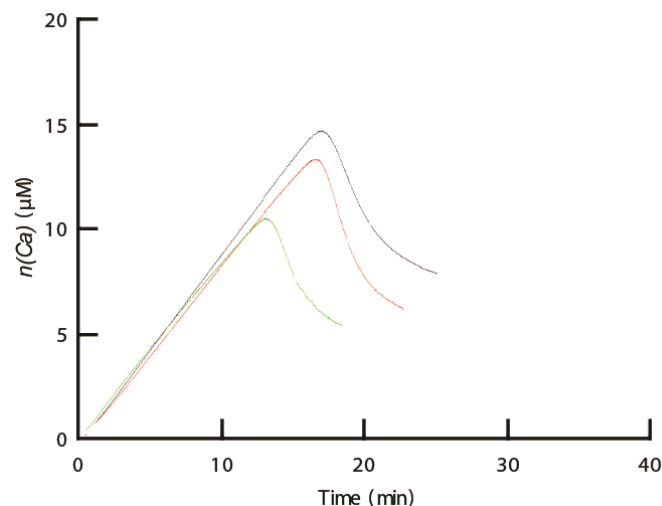


**Figure 25.** Titration curves at pH 13.6 ( $[\text{Na}_2\text{SiO}_3] = 6.6 \text{ mM}$ ,  $[\text{CaCl}_2] = 30 \text{ mM}$ ) with a dosing speed of 0.04 mL/min (green), 0.02 mL/min (red) and 0.01 mL/min (black) over the dosed amount of calcium.

Higher dosing speed shifts the nucleation point to the higher amount of free calcium in solution at  $t_{max}$ . The higher the dosing speed, the higher the corresponding calcium amount of the supersaturation when all other ion concentrations in solution stay constant. In Figure 25, the amount of free calcium measured in solution differs from the theoretically dosed amount. Some free calcium is taken out of the system, most likely due to adsorption or complexation of silicate in the solution. According to the reasoning presented, the longer reaction time for the nucleation with lower dosing speed increases the degree of oligomerization of the silica species in solution. A lower amount of calcium is needed to

structure and stabilize the silicate chains. This is in accordance with the expectation, as the degree of oligomerization has an influence on the surface charge of the silicate chains and the number of calcium ions needed to compensate the negative charge. The ripening time has an influence on the amount of calcium incorporated in the formed species.

To analyse the influence of additives on the C-S-H nucleation, it should be taken into account that the experimental parameters like dosing and stirring speed stay constant.

### Influence of sugars on the C-S-H nucleation

In a series of experiments, the influence of sugars and the sweetener saccharin, as typical retarders of the cement hydration process, were investigated in the C-S-H nucleation model system. The structural chemical formula of the analysed additives is shown in Figure 26.

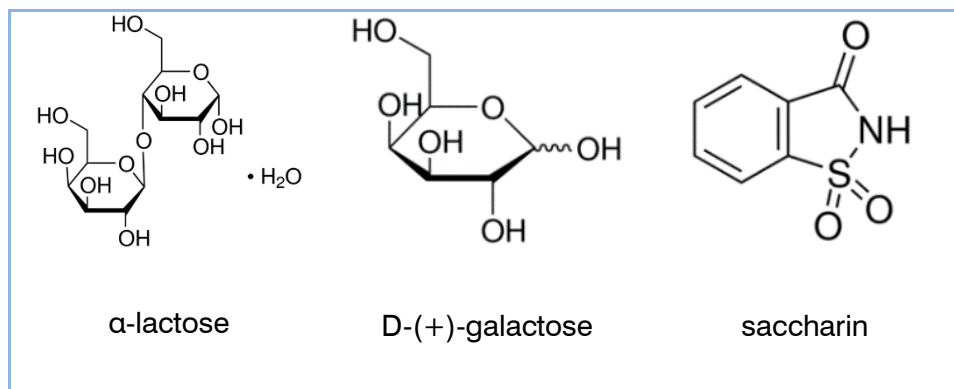


**Figure 26.** Structural chemical formula of  $\alpha$ -lactose, D-(+)-galactose and saccharin.

According to Taylor, (2) the mechanism of retardation by sugars is an adsorption of sugar molecules onto the surfaces of growing particles of hydrating products and a result of free calcium ion complexation. The titration curves of  $\alpha$ -lactose and D-(+)-galactose are shown in Figure 27 and Figure 28.

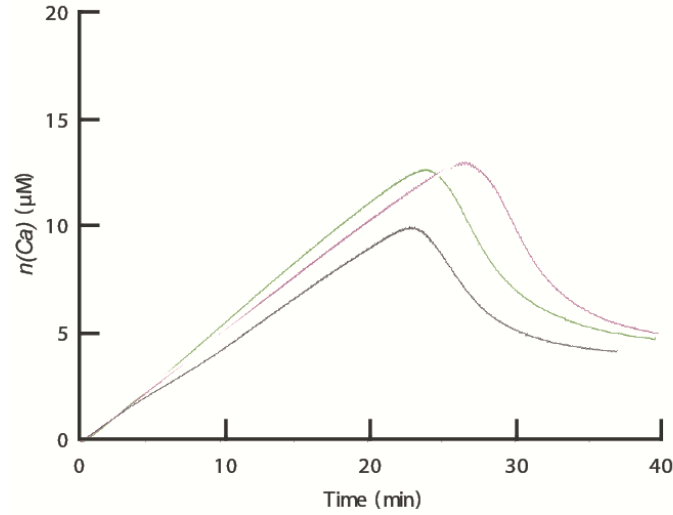


**Figure 27.** Titration curves at pH 13.6 ( $[\text{Na}_2\text{SiO}_3] = 6.6 \text{ mM}$ ,  $[\text{CaCl}_2] = 30 \text{ mM}$ ) with addition of 10 mg lactose (green) and 15 mg lactose (purple).

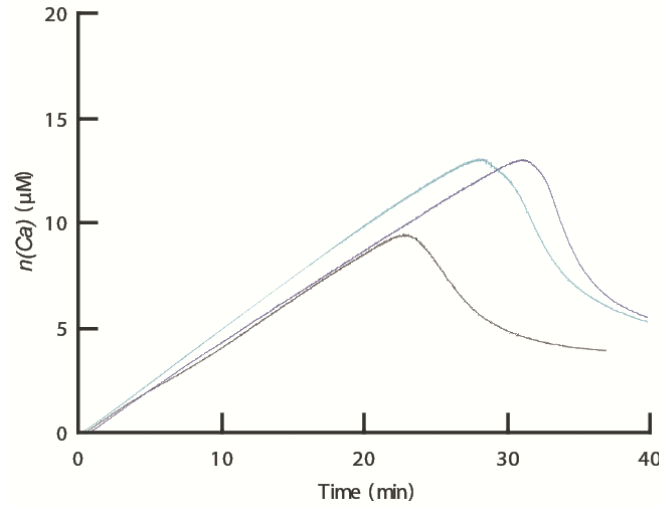


**Figure 28.** Titration curves at pH 13.6 ( $[\text{Na}_2\text{SiO}_3] = 6.6 \text{ mM}$ ,  $[\text{CaCl}_2] = 30 \text{ mM}$ ) with addition of 10 mg galactose (turquoise) and 15 mg galactose (purple). The blue graph shows the dosed amount of calcium by titration.

The reasoning presented by Taylor is not in accordance with our titration results. It was not possible to observe a strong uptake of free calcium from the solution. In contrast to the expectation, an increase in pre-nucleation slope is observed in presence of the additives. For comparison reasons, a relative amount of maximum calcium content (rel.  $n_{max}$ ), maximum time (rel.  $t_{max}$ ), and slope (rel.  $m_1$  and rel.  $m_2$ ) is defined.

$$rel. n_{max} = \frac{n_{max} - n_{max}(reference)}{n_{max}(reference)} \quad (14)$$

$$rel. t_{max} = \frac{t_{max} - t_{max}(reference)}{t_{max}(reference)} \quad (13)$$

$$rel. m_1 = \frac{m_1}{m_1(reference)} \quad (14)$$

$$rel. m_1 = \frac{m_2}{m_2(\text{reference})} \quad (15)$$

**Table 1:** Comparison of the effect of lactose and galactose on the nucleation of C-S-H.

Additive	$n_{max}$ ( $\mu\text{M}$ )	$t_{max}$ (min)	$m_1$ ( $\mu\text{M}/\text{min}$ )	$m_2$ ( $\mu\text{M}/\text{min}$ )	Rel. $n_{max}$	Rel. $t_{max}$	Rel. $m_1$	Rel. $m_2$
+ 10 mg lactose	12.14	24.50	0.56	-1.10	11.14	23.50	1.18	0.73
+ 15 mg lactose	12.52	26.60	0.51	-0.80	11.52	25.60	1.07	0.53
+ 10 mg galactose	13.18	28.34	0.46	-1.41	12.18	27.34	1.15	1.67
+ 15 mg galactose	13.18	31.22	0.43	-1.73	12.18	30.22	1.07	2.04

The reaction time is longer for higher concentrations of lactose. The effect increases from lactose to galactose. Rel.  $t_{max}$  increases from 25.60 to 30.22 with 15 mg lactose to 15 mg of galactose. This effect can be seen as well in an increase of rel.  $n_{max}$  and rel.  $m_2$ . It was possible to compare the effect of the sugars on the calcium potential by comparing the effect on the pre and post-nucleation slope and the time of maximum calcium potential. It was not possible to observe a strong uptake of free calcium from the solution in presence of the analysed sugars. In contrast to the expectation, it was not possible to monitor a retarding effect on the nucleation of the calcium silicate hydrate in this system. As lactose and galactose are reducing sugars, in a basic environment, the Lobry de Bruyn Alberda van Ekenstein transformation takes place. The transformation of an aldose into the ketose isomer or vice versa, with a tautomeric enediol as a reaction intermediate, is proposed to be responsible for the retarding effect of sugars during the cement hydration. (2) In this study, an increase of rel.  $m_1$  indicated that the sugars lower the ability of the silicate species to bind the free calcium effectively in solution. Besides that, this result indicates that the mechanism in this model system is not based on a simple complexation of free calcium by the negative charge of the tautomeric endiol. This indicates that, other than a simple calcium complexation, further interactions are responsible for the retarding influence of sugars on the cement hydration process. A better understanding of the development of silicate species in solution is needed for further analysis of the influence of the sugars on the system. Taking a closer look at the silicate species could be realized with the help of DLS after quenching the reaction with ethanol.

## Influence of polymers on the calcium silicate hydrate system

The chemical structural formula of the investigated polymers is shown in Figure 29 (L1). polymer L3 has PEG side chains in addition to the structure in Figure 22 of polymer L1.

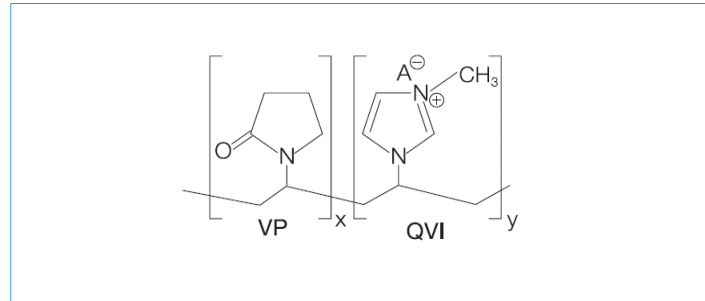


**Figure 29.** Structural chemical formula of copolymers of vinylpyrrolidone (VP) and quaternized vinylimidazole (QVI).

Figure 30, Figure 31, Figure 32, and Figure 33 show the titration curves observed with FC 370, FC 550, L1, and L3, respectively.

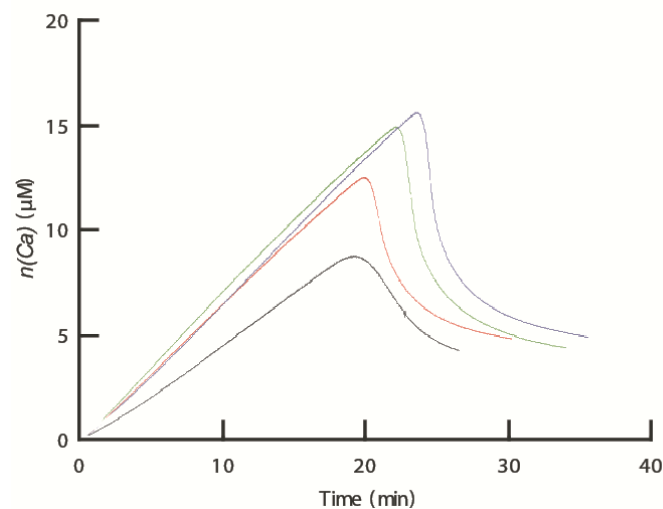


**Figure 30.** Titration curves at pH 13.6 ( $[\text{Na}_2\text{SiO}_3] = 6.6 \text{ mM}$ ,  $[\text{CaCl}_2] = 30 \text{ mM}$ ) with the addition of FC 370. Comparison of the effect of 2.5 mg (red), 5 mg (green) and 15 mg FC 370(blue). .

**Table 2:** Comparison of the effect of FC 370 on the nucleation of C-S-H.

Additive	$n_{max}$ ( $\mu\text{M}$ )	$t_{max}$ (min)	$m_1$ ( $\mu\text{M}/\text{min}$ )	$m_2$ ( $\mu\text{M}/\text{min}$ )	Rel. $n_{max}$	Rel. $t_{max}$	Rel. $m_1$	Rel. $m_2$
+ 2.5 mg FC 370	12.48	25.01	0.49	-2.64	11.48	24.01	1.19	3.29
+ 5 mg FC 370	14.83	27.74	0.55	-4.24	13.83	26.74	1.33	5.27
+ 15 mg FC 370	15.50	29.49	0.55	-4.95	14.50	28.49	1.13	6.16

FC 370 shows a retarding effect on the formation process. A strong increase in  $m_1$  was observed with only 2.5 mg of FC 370. The reaction time for the nucleation is longer when increasing the amount of FC 370. An increase in  $n_{max}$  is observed correspondingly. The longer the reaction for the nucleation, the higher rel.  $m_2$  is. After the nucleation point, the amount of free calcium in solution decreases to a value around 5  $\mu\text{M}$ , which is higher than without the addition of the additive. More calcium needs to be added to reach the critical supersaturation, after which less calcium is bound into the final product. The effect is comparable with that already observed with  $\alpha$ -lactose, but it should be taken into account that the dosing with FC 370 is one order of magnitude lower.

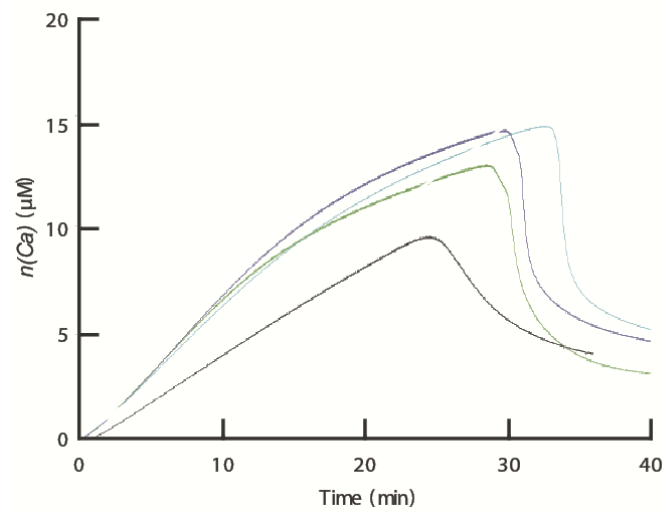


**Figure 31.** Titration curves at pH 13.6 ( $[\text{Na}_2\text{SiO}_3] = 6.6 \text{ mM}$ ,  $[\text{CaCl}_2] = 30 \text{ mM}$ ) with addition of FC 550. Comparison of the effect of 2.5 mg (green), 20 mg (dark blue) and 40 mg FC 550 (light blue).

**Table 3:** Comparison of the effect of FC 550 on the nucleation of C-S-H.

Additive	$n_{max}$ ( $\mu\text{M}$ )	$t_{max}$ (min)	$m_1$ ( $\mu\text{M}/\text{min}$ )	$m_2$ ( $\mu\text{M}/\text{min}$ )	Rel. $n_{max}$	Rel. $t_{max}$	Rel. $m_1$	Rel. $m_2$
+ 2.5 mg FC 550	12.75	28.51	0.37	-4.59	11.75	27.51	0.81	4.72
+ 20 mg FC 550	14.33	29.62	0.74	-8.67	13.33	28.62	1.64	8.91
+ 40 mg FC 550	14.51	32.59	0.65	-8.70	13.51	31.59	1.45	8.94

As for FC 370, with the addition of FC 550, a retarding effect can be observed as well, with a high increase of  $m_1$ ,  $n_{max}$  and  $t_{max}$ . In comparison to the addition with FC 370, the titration curves show a flatter pre-nucleation slope in combination with a small plateau after a first nucleation point. The plateau indicates that the polymers stabilize primary formed particles to a certain extent. Figure 32 shows the addition of L1.

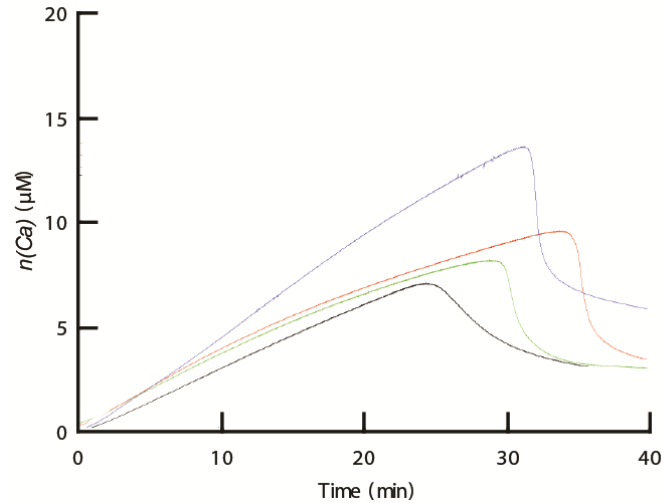


**Figure 32.** Titration curves at pH 13.6 ( $[\text{Na}_2\text{SiO}_3] = 6.6 \text{ mM}$ ,  $[\text{CaCl}_2] = 30 \text{ mM}$ ) with addition of L1. The blue graph shows the dosed amount of calcium by titration. Comparison of the effect of 3 mg (green), 10 mg (red) and 20 mg L1 (blue).

**Table 4:** Comparison of the effect of L1 on the nucleation of C-S-H.

Additive	$n_{max}$ ( $\mu\text{M}$ )	$t_{max}$ (min)	$m_1$ ( $\mu\text{M}/\text{min}$ )	$m_2$ ( $\mu\text{M}/\text{min}$ )	Rel. $n_{max}$	Rel. $t_{max}$	Rel. $m_1$	Rel. $m_2$
+ 3 mg L1	9.71	36.78	0.84	-9.57	15.71	35.78	1.82	9.72
+ 10 mg L1	10.25	30.54	0.69	-12.0	16.35	30.25	1.51	12.2
+ 20 mg L1	14.82	31.25	0.96	-14.2	12.4	31.10	1.03	14.5

L1 shows a strong retarding effect. With higher amounts of L1, an increase in  $n_{max}$ ,  $m_1$ , and  $m_2$  is observed. In contrast to the previous experiments, the highest concentration of L1 results in a shorter reaction time. Table 5 shows a comparison of the addition of FC 550, FC 370, and L1. A plateau is not observed by the addition of the polymer with the highest degree of positive charge density.

**Table 5:** Comparison of the effect of FC 370, FC 550, and L1 on the nucleation of C-S-H.

Additive	Charge ( $\text{meq} \cdot 10^{-3}$ )	Rel. $n_{max}$	Rel. $t_{max}$	Rel. $m_1$	Rel. $m_2$
+ 2.5 mg FC 370	5.00	11.48	24.01	1.19	3.29
+ 2.5 mg FC 550	8.25	11.75	27.51	0.810	4.72
+ 3 mg L1	18.3	15.71	35.78	1.82	9.72

The effect of the high charge density of L1 has a strong effect on rel.  $n_{max}$  and rel.  $m_2$ , whereas the effect on the reaction time is comparably low. Figure 33 shows the titration curves with L3.



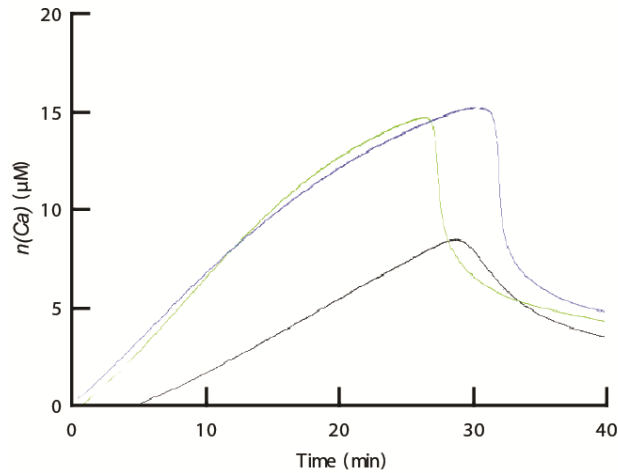


**Figure 33.** Titration curves at pH 13.6 ( $[\text{Na}_2\text{SiO}_3] = 6.6 \text{ mM}$ ,  $[\text{CaCl}_2] = 30 \text{ mM}$ ) with addition of L3 12.5 mg (green) and 15 mg (blue) with reference (black).

**Table 6:** Comparison of the effect of L3 on the nucleation of C-S-H.

Additive	$n_{max}$ ( $\mu\text{M}$ )	$t_{max}$ (min)	$m_1$ ( $\mu\text{M}/\text{min}$ )	$m_2$ ( $\mu\text{M}/\text{min}$ )	Rel. $n_{max}$	Rel. $t_{max}$	Rel. $m_1$	Rel. $m_2$
+ 12.5 mg L3	17.14	26.96	0.78	-9.51	16.06	25.96	1.77	11.0
+ 15 mg L3	17.71	30.84	0.76	-11.3	16.71	29.84	1.73	13.1

The addition of L3 shows a strong increase in rel.  $n_{max}$ ,  $m_1$ , and  $m_2$ . With 12.5 mg L3, the reaction time is shorter than without the additive, and the additive shows an accelerating effect on the C-S-H nucleation at this dosing. This is in contrast to the previous series of experiments with LC 370 and LC 550. Table 7 shows a comparison of the effect of L1 and L3.

**Table 7:** Comparison of the effect of L1 and L3 on the nucleation of C-S-H.

Additive	Charge ( $\text{meq} \cdot 10^{-3}$ )	Rel. $n_{max}$	Rel. $t_{max}$	Rel. $m_1$	Rel. $m_2$
+ 3 mg L1	18.3	15.71	35.78	1.82	9.72
+ 12.5 mg L3	32.5	16.06	25.96	1.77	11.0
+ 10 mg L1	61.0	16.35	30.25	1.51	12.2

The comparison in Table 6 and Table 7 shows that, with the increasing positive charge density of the additive, rel.  $n_{max}$  and rel.  $m_2$  increase. This indicates that the interaction of the negative silicate species with the free calcium in solution is less effective with the addition of the positively charged polymers. The rel.  $m_1$  and  $t_{max}$  do not show a clear trend with increasing amount of positive charge.

### 3.2.4 Conclusion

In this chapter, the influence of cationic polymers on the nucleation behaviour of a calcium silicate hydrate system was studied. The presence of copolymers of poly[(3 methyl 1 vinylimidazolium chloride) co (1 vinylpyrrolidone)] has a strong influence on the calcium potential during the formation of the calcium silicate species. Calcium was bound in the pre-nucleation stage by the polymers, and the polymers impact the stabilization of the pre-forms species in solution. The increasing positive charge density from FC 370 to FC 550 revealed a strong stabilizing effect on the primary nucleated particles and resulted in a second nucleation point during the nucleation process. I. Pochard et al. analysed the influence of cationic oligomers in cement pastes and examined an attractive interaction between charged oligoelectrolytes and C-S-H particles. As a crucial aspect, it was highlighted that oligoelectrolytes can compete with calcium as counterions to the ionized silanol groups of the C-S-H. The stabilizing effect of the first formed species examined in presence of the highly charged copolymers in this study can be explained by the exchange of calcium ions against the polymer as counterions. For a given pH, there is a considerable change in surface charge density with the valence of the counterion. As oligoelectrolytes lead to a stronger positive surface charge than monovalent sodium ions, polymers containing exclusively positively charged units like polyDADMAC, can serve as a template for the silicate oligomerization. Picker examined an accelerating effect on the nucleation of C-S-H in presence of polyDADMAC. (100) It was proposed that a local supersaturation with respect to C-S-H finally leads to an accelerated formation of C-S-H nuclei and subsequent agglomeration. This indicates that the polymers have an influence on the calcium-catalyzed oligomerization and the pre-structuring of silicate chains. Further feasible scenarios for the results, based on the previous mechanism proposed in Chapter 2.1, imply a stabilization of the rather unordered primary nucleated particles by the polymer, i.e. an inhibition of aggregation. However, in addition to these first results of the polymer screening, more thorough investigations have to be made to elucidate the exact processes going on during the nucleation in presence of the cationic additives. Cryo-TEM or DLS in combination with SLS experiments could gain insight into the type of formed particles at various points of time to compare the results with the non-additive case.

# **Influence of biomolecules on cement hydration**

## 4.1 Enzyme screening

### 4.1.1 Objectives

There is still much research to be done in the area of biocement, and it would be highly desirable to find other bio-additives with the potential to dramatically improve the concrete properties in terms of mechanical performance and hardening benefits. There is much potential in interfering with the early hydration process of cement by speeding up C-S-H formation for improving the early strength development of concrete. In the course of this study, additives popular from the field of silica mineralisation, which have unique properties to catalyse the formation of silica, were analysed. By using only small amounts of an additive with catalytic activity, the possible negative effects on the performance of Ordinary Portland cement (OPC) by changing the typical composition could be reduced. So far, proteins catalysing silica formation have inspired innovative high-performance composites for construction applications. One of the recent examples of proteins, which are involved in the bio-enabled synthesis of nanomaterials, is silaffin. First identified in diatoms, silaffins represent a class of peptides and proteins that direct precipitation of silica at neutral pH and ambient temperatures in vitro. In addition to silica formation, silaffin has recently been recognized as an attractive template for titania mineralization under mild aqueous conditions.<sup>(101)</sup> These titania nanostructures are of special importance due to their current and prospective applications as photocatalysts, UV blockers, photochromic pigments, oxygen sensors and components in lithium batteries and solar cells.<sup>(102)</sup> Another molecule that attracts much attention is silicatein. This is not only a structure-guiding protein but also a structure-forming protein. Silicateins are the key enzymes involved in the enzymatic polycondensation of the inorganic scaffold of the skeletal elements of the siliceous sponges, the spicules. Silicatein uses both ortho-silicate and organosilicon as a substrate for in vitro and in vivo silica formation.<sup>(37)</sup> The addition of even very small portions of these bioextracts leads to a tenfold increase in the amount of harvestable silica. The aim of this study is to verify whether proteins with silica activity, like silicatein, can also reach their potential of speeding up silicate/C-S-H formation under less physiological conditions, such as in the cement environment, with an extremely basic pH and high salinity on a laboratory level.

### 4.1.2 Results and discussion

The results provided by isothermal calorimetry (for more detail see of OPC with different additives are as shown:

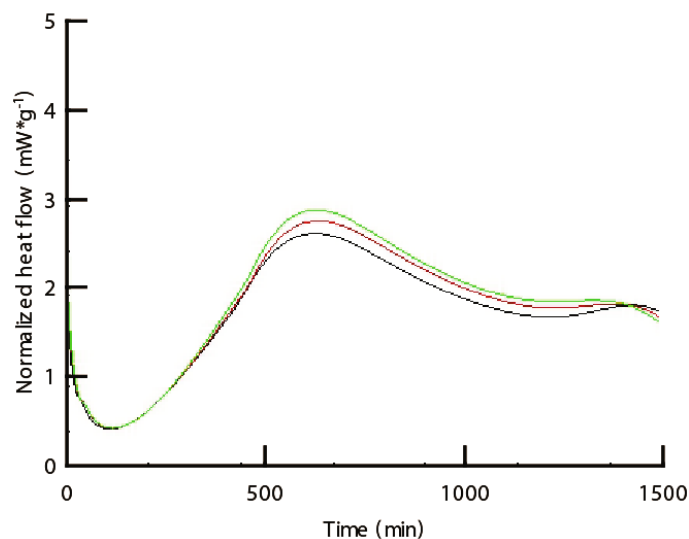


**Figure 34.** Heat flow curves of the hydration of OPC with 225 (red) and 450 ppm (green) papain and reference (black) over 1500 minutes.

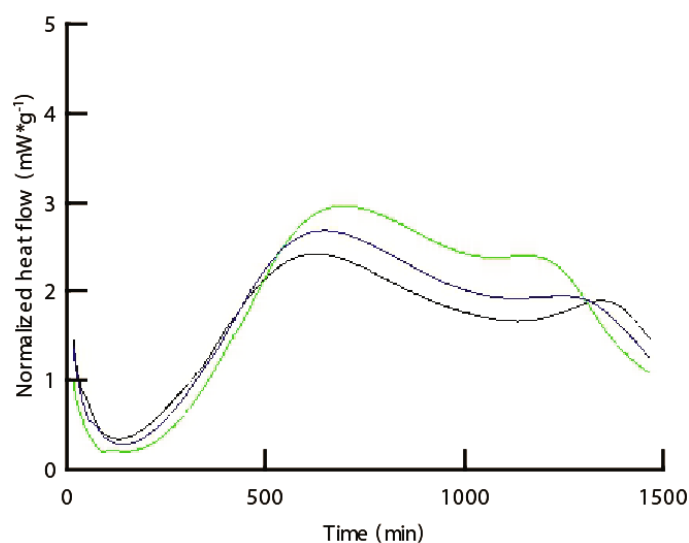


**Figure 35.** Heat flow curves of the hydration of OPC with 625 (blue) and 1350 ppm (green) papain and reference (black) over 1500 minutes.

**Table 8:** Degree of acceleration of the hydration of OPC caused by 225 and 450 ppm papain.

Additive	$H_{max}$ (mW/g)	$P(H_{max})$ (%)	$t_{max}$ min	$P(HoH)$ (%)	$P(slope)$ (%)
Blank	2.69	100.00	554.00	100.00	100.00
225 ppm papain	2.82	104.97	555.00	103.30	101.52
450 ppm papain	2.94	109.36	554.00	105.80	110.73

An effect on the main heat flow event can be seen with an increase in maximum slope with 1.52% and 10.73% with papain. Furthermore, a small accelerating effect can be seen with an increase in  $H_{max}$  of 4.97% and 9.36%.

**Table 9:** Degree of acceleration of the hydration of OPC caused by 625 and 1350 ppm papain.

Additive	$H_{max}$ (mW/g)	$P(H_{max})$ (%)	$t_{max}$ (min)	$P(HoH)$ (%)	$P(slope)$ (%)
Blank	2.56	100.00	583.80	100.00	100.00
625 ppm papain	2.82	110.16	600.60	112.50	118.75
1350 ppm papain	3.08	120.31	645.00	126.99	129.59

The addition of higher concentrations of papain influences the heat of hydration. The effect on the main heat flow event can be seen with an increase in the maximum slope with 18.75% and 29.59%. An accelerating effect can be seen with an increase in  $H_{max}$  of 10.16% and 20.31%.  $HoH$  is greatly accelerated up to 26.99%.

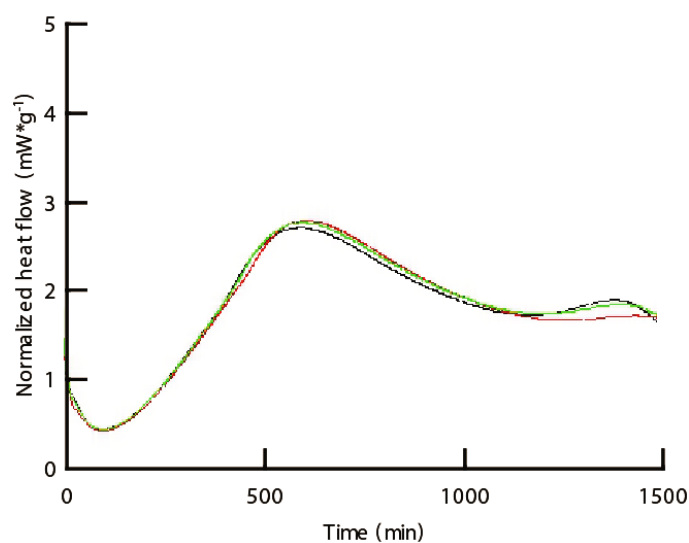


**Figure 36.** Heat flow curves of the hydration of OPC with 25 (green) and 50 ppm (red) modified polylysine (6% histidine) with reference (black) over 1500 minutes.

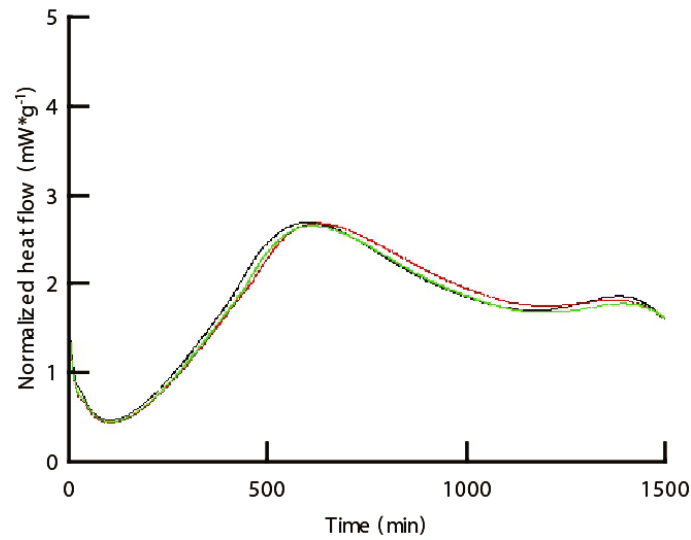


**Figure 37.**Heat flow curves of the hydration of OPC with 25 (green) and 50 ppm (red) cathepsin B with reference (black) over 1500 minutes.

**Table 10:** Acceleration of the hydration of OPC caused by cathepsin B at different concentrations.

Additive	$H_{max}$ (mW/g)	$P(H_{max})$ (%)	$t_{max}$ (min)	$\rho(HoH)$ (%)	$P(slope)$ (%)
-	2.72	100.00	565.00	100.00	100.00
25 ppm cathepsin B	2.68	98.71	575.00	97.62	94.48
50 ppm cathepsin B	2.72	100.04	594.00	99.42	89.56

The addition of modified polylysine and cathepsin B did not affect the heat flow in a significant way. cathepsin B had a small decelerating effect with a decrease in slope and retardation in reaching  $H_{max}$ . Figure 38 displays the normalized heat flow of OPC with trypsin.

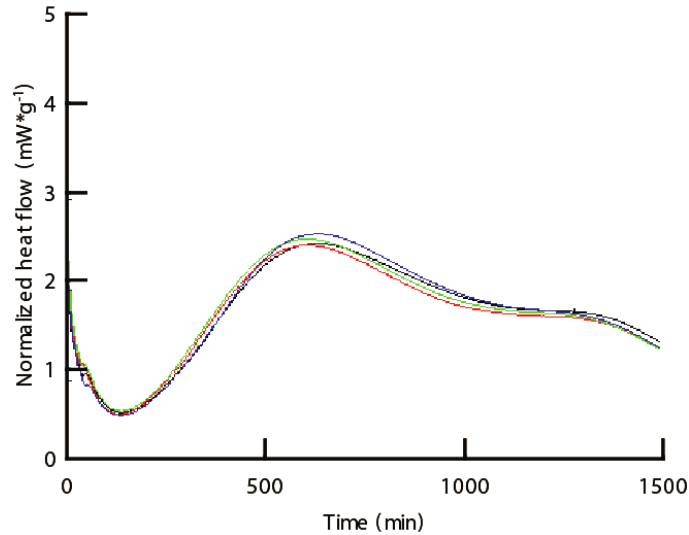


**Figure 38.** Heat flow curves of the hydration of OPC with 50 (red), 150 (green), and 450 (blue) ppm trypsin with reference (black) over 1500 minutes.

**Table 11:** Degree of acceleration of the hydration of OPC caused by 50, 150, and 450 ppm trypsin.

Additive	$H_{max}$ (mW/g)	$P(H_{max})$ (%)	$t_{max}$ (min)	$P(HoH)^*$ (%)	$P(slope)$ (%)
-	2.51	100.00	594.00	100.00	100.00
50 ppm trypsin	2.50	99.601	562.00	98.922	101.12
150 ppm trypsin	2.55	101.59	560.00	101.57	103.76
450 ppm trypsin	2.63	104.78	589.00	102.32	106.06

\* Integration from 190 to 1000 minutes.

The addition of trypsin has a small effect on the hydration process. The effect on the main heat flow event can be seen with an increase in maximum slope with 6.06% with the addition of 450 ppm trypsin. An accelerating effect is examined with an increase in  $H_{max}$  of 4.78%. Furthermore,  $t_{max}$  was achieved up to 35 minutes earlier with 150 ppm trypsin. These results indicate that the additive has a small accelerating effect on the hydration process. According to the manufacturer, the presence of calcium (20 mM) will retard the autolysis of trypsin and maintain the stability of the trypsin in the solution, being an advantage for the stability of the enzyme in the cement solution with high calcium concentration. The pH optimum of trypsin at 7.8-8.5 is higher than that of papain at 7, according to the manufacturer. The solubility in water is comparable with those of papain (10 mg/mL). Figure 39 displays the normalized heat flow of OPC with bromelain.



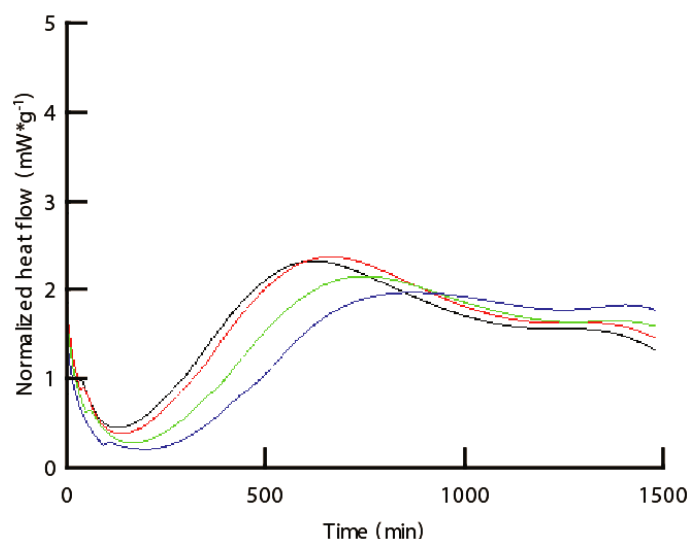


**Figure 39.** Heat flow curves of the hydration of OPC with 50 (red), 150 (green) and 450 ppm (blue) bromelain with reference (black) over 1500 minutes.

**Table 12:** Degree of acceleration of the hydration of OPC caused by bromelain.

Additive	$H_{max}$ (mW/g)	$P(H_{max})$ (%)	$t_{max}$ (min)	$P(HoH)$ *(%)	$P(slope)$ (%)
Blank	2.45	100.00	573.00	100.00	100.00
50 ppm bromelain	2.52	102.86	620.00	100.13	105.02
150 ppm bromelain	2.30	93.87	712.00	88.768	89.331
450 ppm bromelain	2.12	86.53	807.00	77.471	81.370

\* Integration from 190 to 1000 minutes.

The addition of bromelain has a retarding effect on the heat of hydration. The effect on the main heat flow event can be seen with a decrease in maximum slope with 18.63%. Another peculiarity is the shift of  $t_{max}$  with higher concentration of bromelain. With 450 ppm bromelain added,  $t_{max}$  is achieved 4 hours later. The effect of bromelain on the hydration process does not resemble the effect of the cysteine protease papain. It is worth mentioning that the optimum pH range for the protease activity of bromelain is with 4.5-5.5 lower compared with those of papain according to the manufacturer. The optimum pH range of papain is around 7. Besides that, the solubility of bromelain in water is 1 mg/mL, ten times lower compared to that of papain.

#### 4.1.3 Conclusion and outlook

During the course of screening of enzymes by IC, papain is the only additive having an accelerating effect on the hydration process. The accelerating effect can be expressed in an acceleration of  $H_{max}$  at up to 20.31% and an acceleration of the maximum slope of 29.95%. The addition of 50, 150, and 450 ppm trypsin has small effects on the hydration process.

The effect on the main heat flow event can be seen with an increase in maximum slope with 6.06% with the addition of 450 ppm trypsin. An accelerating effect can be seen with an increase in  $H_{max}$  of 4.78%. Furthermore,  $t_{max}$  was achieved up to 35 minutes earlier with 150 ppm trypsin. These results indicate that the additive has an accelerating effect on the hydration process. bromelain shows a retarding effect on the heat of hydration. The effect on the main heat flow event can be seen with a decrease in maximum slope with 18.63%. Another peculiarity is the shift of  $t_{max}$  with a higher concentration of bromelain. With 450 ppm bromelain,  $t_{max}$  is achieved 4 hours later. The effect of bromelain on the hydration process does not resemble the effect of the cysteine protease papain. It is worth mentioning that the optimum pH range for the protease activity of bromelain is 4.5-5.5, which is lower compared to those of papain, according to the manufacturer. In the further course of this study, a control test with dialyzed papain was carried out (3.2.). The control test has the ability to confirm the specific influence of the enzyme on the hydration process. Besides that, using  $C_3S$  as a test system, instead of OPC, provides information about the accelerating effect on the silicate reaction. To better understand how the enzyme interferes with the cement hydration, a simple first step could be to check if the active site of papain is really involved in the process. An approach for that is, to monitor the influence of the enzyme after thermal denaturation.

## 4.2 The effect of the cysteine protease papain

### 4.2.1 Objectives

To provide a better understanding of the interference of the cysteine protease papain in the cement hydration, a simple first step was to analyse whether the active site of papain is really involved in the process. An approach for that is to block the active site residue of the enzyme and to determine the effect of this modified enzyme on the hydration process. “The coomassie blue dye binding was used to determine the protease activity of the active and inactivated papain prior to inserting them into the cement hydration process. To ensure the full activity of the papain, the cysteine residue must be present in reduced form. Furthermore, the coomassie assay was used in several experiments to analyse the effect of a basic environment on the protease activity of papain.” These experiments provide useful information about the influence of a basic cement environment on the enzyme. A polyacrylamide gel electrophoresis (PAGE) was performed to determine the molar mass of the enzyme during the experiments and to roughly estimate their concentrations. Isothermal calorimetry (IC) was performed to analyse the effect of inhibited papain on the hydration process. “To exclude the effect of buffer salts on the hydration process, papain was supplied in a 50 mM sodium acetate solution (pH 7.0). The effect of a 50 mM sodium acetate buffer has been examined and is negligible in the IC of OPC.” For this purpose, papain was purified *via* the spin column method and supplied in 50 mM sodium acetate (pH 7.0, for more detail see A9-A14).

## 4.2.2 Results and discussion

The effect of the substrate Casein on the coomassie blue absorbance spectrum is shown in Figure 40. The coomassie blue was adjusted to a final concentration of 0.0025% (w/v) in a phosphoric acid-ethanol solution (see Materials and Methods). Absorbance spectra from 400 to 700 nm were obtained.

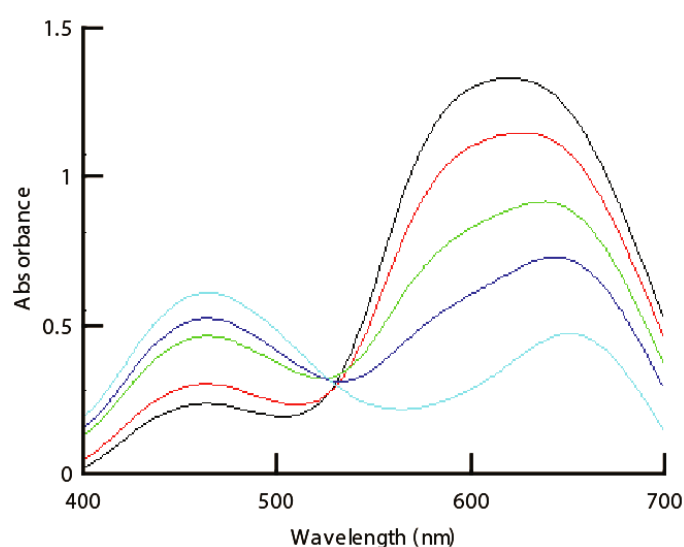


**Figure 40.** Absorbance spectra of coomassie blue from 400 to 700 nm at 5 (black), 3.75 (red), 2.5 (green) and 1.25 mg/mL (blue) of the substrate Casein with reference (light blue).

Without protein, the dye stayed in the cation form (Bickerstagg, 1993) with an absorbance peak at 470 nm. The addition of protein changed the spectrum primarily to that of the anion species with an absorbance maximum at 595 nm.

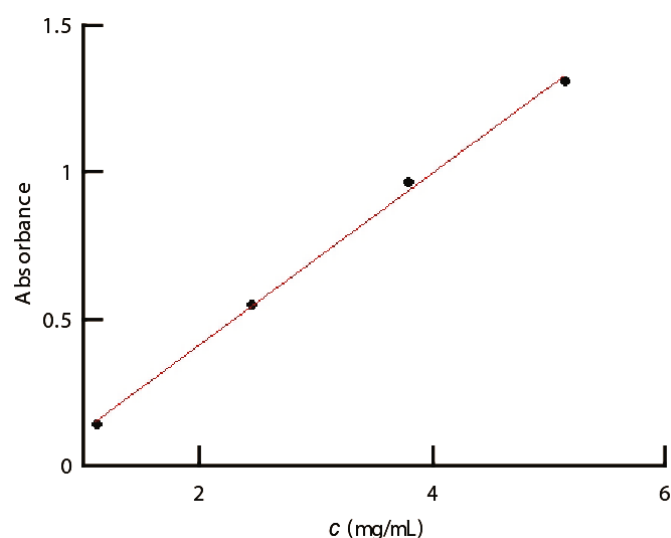


**Figure 41.** Absorbance at 595 nm versus different concentrations of Casein at 595 nm.

The plot of the absorbance at 595 nm with different concentrations of the protein reveals a high linearity with  $R^2=0.998$ . The absorbance increases linearly with increasing Casein concentration. This is in accordance with the expectation that small differences in Casein concentration can be monitored by the coomassie assay. Figure 42 displays the absorbance difference at 595 nm with different concentrations of activated and inactivated papain. The absorbance difference was calculated by subtracting the absorbance of the protease assay from the absorbance of the control experiment without papain.”

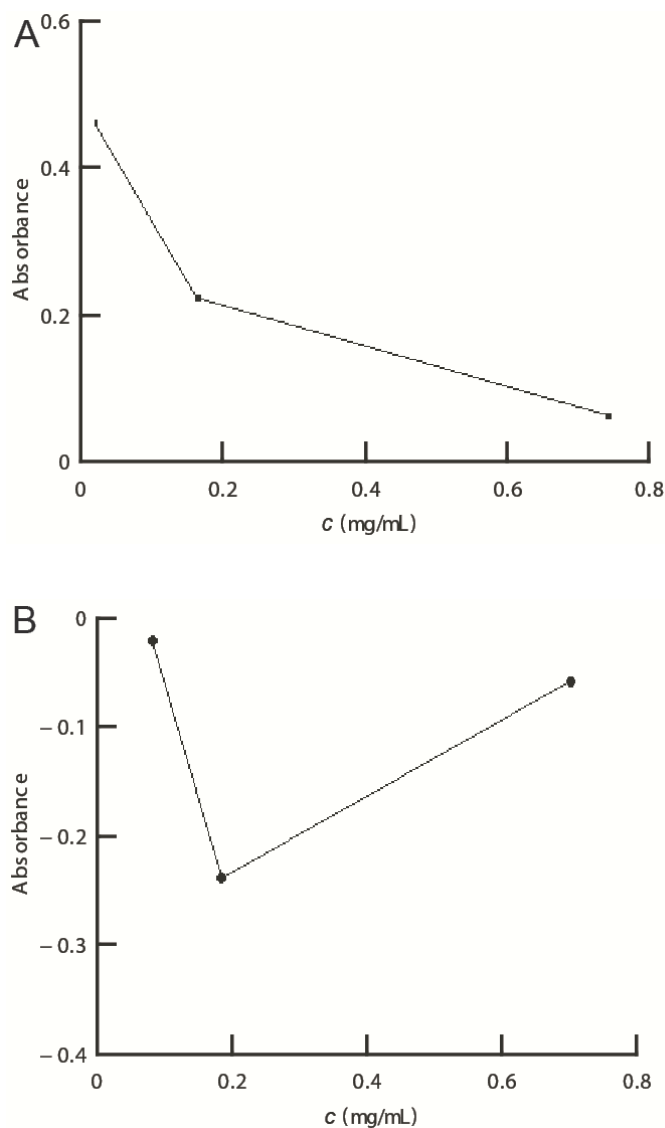


**Figure 42.** (A). The absorbance difference versus different concentrations of activated papain. (B). The absorbance difference versus different concentrations of inactivated papain at 595 nm.

“For the activated papain, the absorbance difference at 595 nm increases with increasing protease concentration. An activation of the protease was reached. For the inactivated species, negative values for the absorbance difference were observed. In contrast to the

activated papain, no decrease in absorbance is observed. This indicates that the inhibition with NEM was successful and the active site is blocked. The negative values for the difference in absorbance result from a small increase in absolute absorbance with increasing papain concentration because the dye binds to the papain enzyme as well. Figure 43 displays the protease activity of papain (0.7 mg/mL) after incubation in a basic buffer solution (pH 12) for 30 minutes and 2.5 hours.

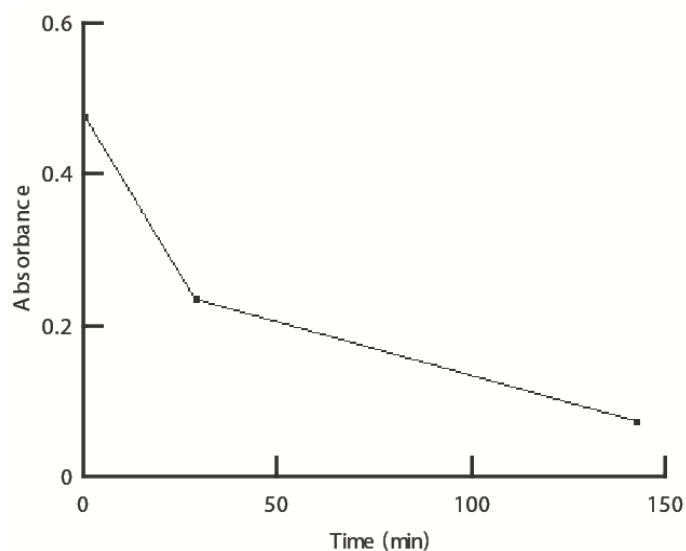


**Figure 43.** Absorbance difference at 595 nm versus time with 0.7 mg/mL of papain after incubation in a basic solution of pH 12.

The incubation in the basic solution prior to the coomassie assay results in a loss of protease activity. The absorbance difference (with a concentration of 0.7 mg/mL) decreases when increasing the time of incubation in the basic solution from 0.49 to 0.16. It should be noticed that after 30 minutes, the absorbance difference is only 40% lower. The effect of a basic substrate solution in the coomassie assay is shown in Figure 44.

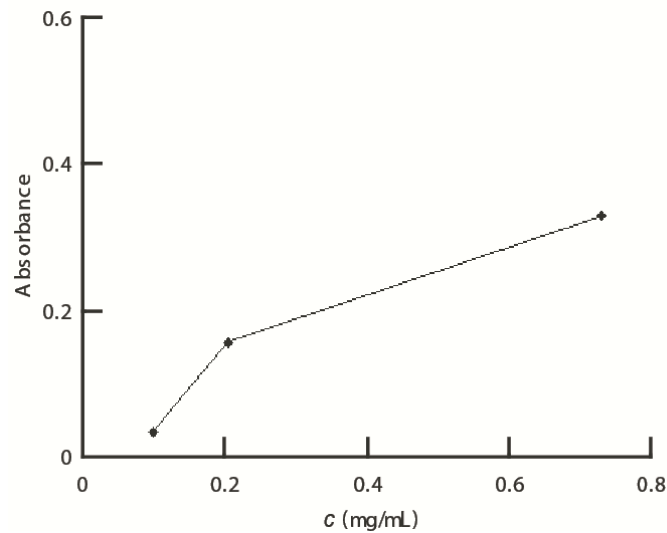


**Figure 44.** Absorbance difference of coomassie assay with basic substrate solution versus different concentrations of papain at 595 nm.

The absorbance difference increases with increasing protease concentration. In contrast to the assay with neutral substrate solution, a lower absorbance difference is observed. With the basic substrate solution, the absorbance difference of 0.7 mg/mL papain is around one-third lower than with the neutral substrate solution. This indicates that the basic substrate solution lowers the protease activity of papain. Figure 45 displays the SDS-PAGE photograph of the Casein solution.

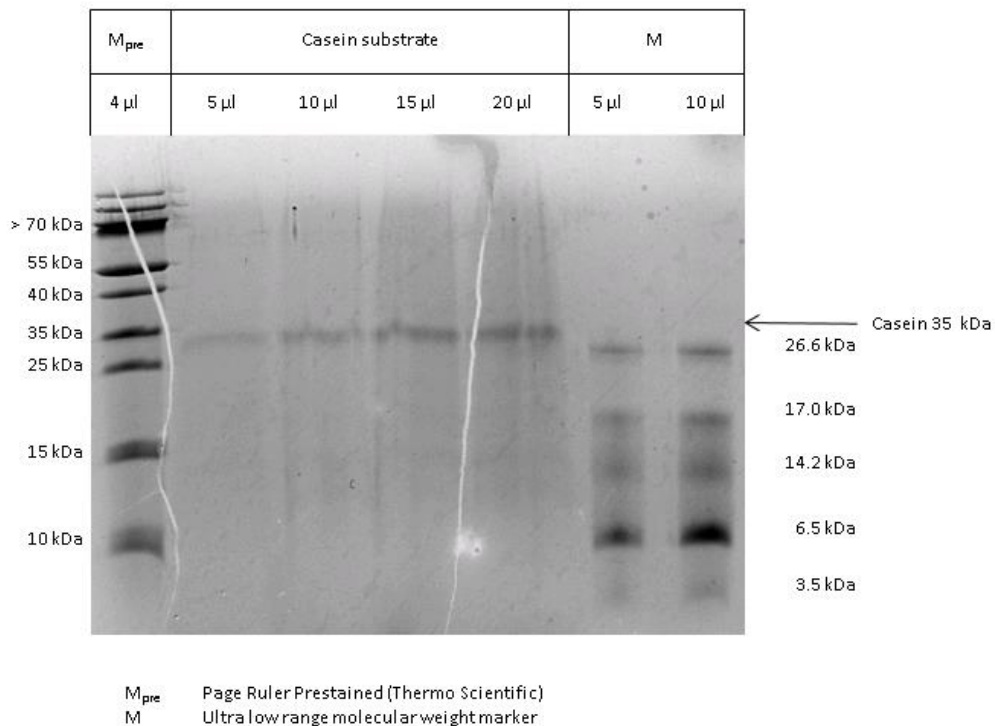


**Figure 45.** SDS-PAGE photograph of the Casein substrate solution. The photograph was taken by a Kodak *Gel-Dokumentation* instrument (EDAS 290) after destaining the gel in a standard fixing solution.

As expected, the mature 35 kDa Casein band appears. The higher the concentration of the protein, the more intense the band is. Figure 46 displays the SDS-PAGE photograph of the activated papain solution.

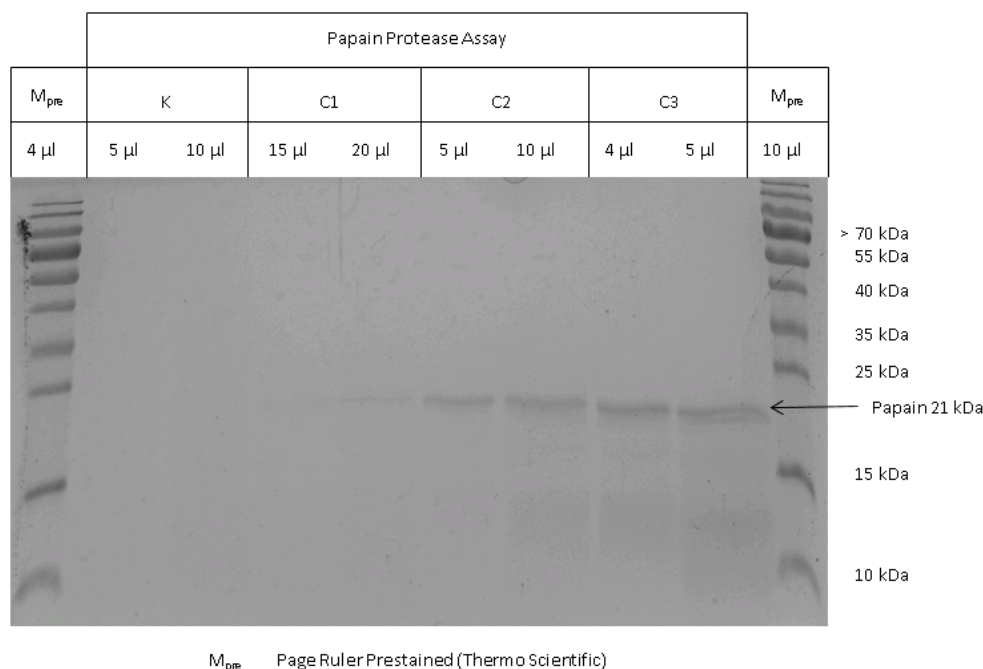


**Figure 46.** SDS-PAGE photograph of the papain protease solution. The photograph was taken by a Kodak *Gel-Dokumentation* instrument (EDAS 290) after destaining the gel in a standard fixing solution. K is the control without papain, C1 contains 0.1mg/mL, C2 contains 0.2 mg/mL, and C3 contains 7 mg/mL.

As expected, the mature 21 kDa papain band appeared. The higher the concentration of the enzyme, the more intense was the papain band. No other bands were monitored. Figure 47 displays the SDS-PAGE photograph of the activated papain protease solution after the incubation with the substrate.



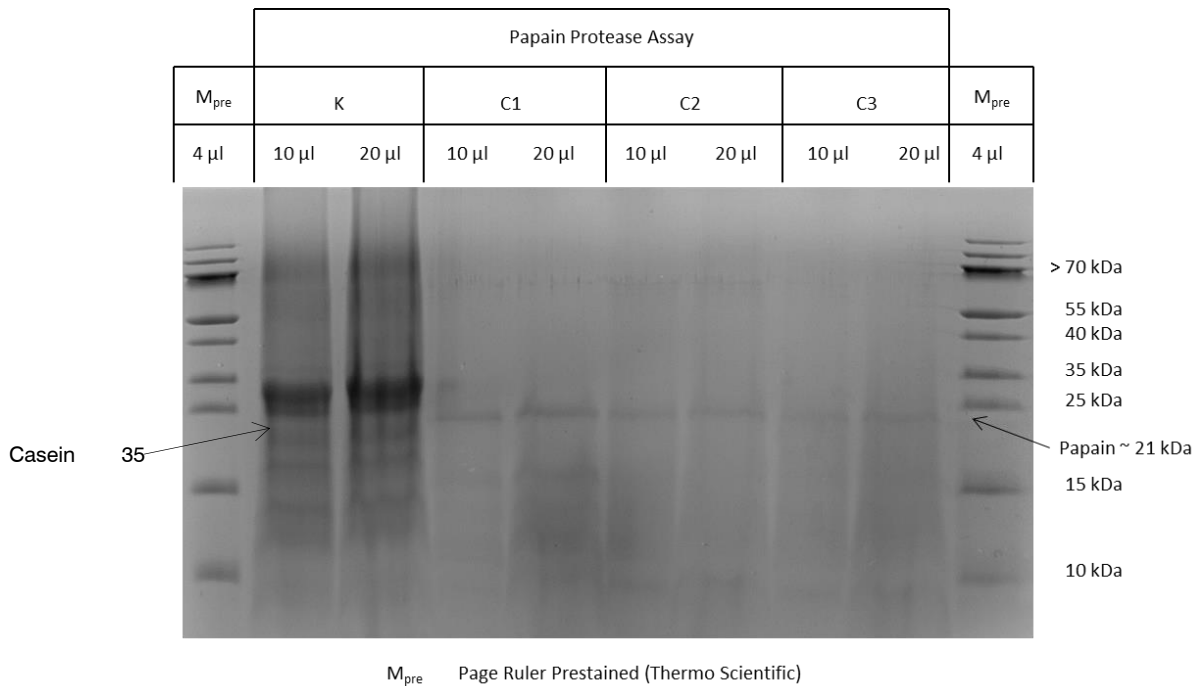


**Figure 47** SDS-PAGE photograph of the papain protease solution after the coomassie assay. The photograph was taken by a Kodak Gel-Dokumentation instrument (EDAS 290) after destaining the gel in a standard fixing solution. K is the control without papain, C1 contains 0.1 mg/mL, C2 contains 0.2 mg/mL, and C3 contains 0.7 mg/mL.

In contrast to the control K, the Casein band of 35 kDa disappeared after 30 minutes in the coomassie assay C1, C2, and C3 with papain. The band of papain appeared at around 21 kDa. As expected, the amount of Casein after 30 minutes of incubation with the protease is negligibly low. This result is in accordance with the results observed *via* the coomassie blue dye binding. papain had a high protease activity. Figure 48 displays the normalized heat flow of OPC with the inhibited papain.”

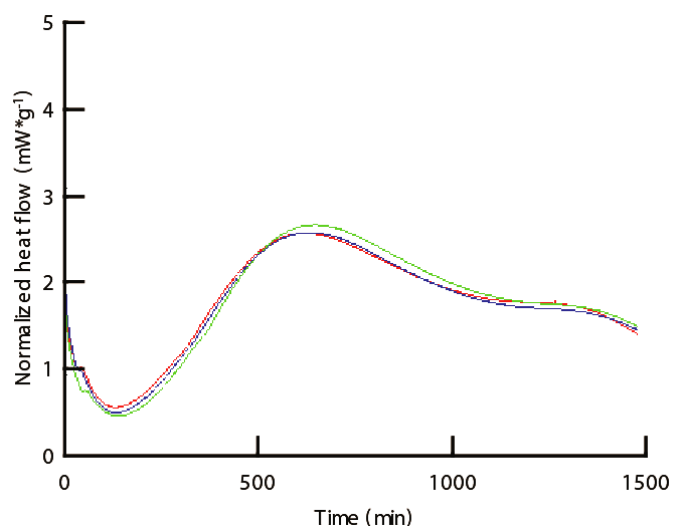


**Figure 48.** Heat flow curves of the hydration of OPC with 450 (blue) and 675 ppm (green) inhibited papain with reference (red) over 1500 minutes.

**Table 13:** Acceleration of the hydration of OPC caused by inhibited papain.

Additive	$H_{max}$ (mW/g)	$P(H_{max})$ (%)	$t_{max}$ (min)	$P(HoH)^*$ (%)	$P(slope)$ (%)
-	2.51	100.00	590.00	100.00	100.00
450 ppm inhibited papain	2.52	100.39	584.00	98.86	101.34
675 ppm inhibited papain	2.60	103.59	611.00	100.69	102.33

\* Integration from 190 to 1000 minutes.

The addition of the inhibited papain does not affect the heat flow in a significant way. 675 ppm of inhibited papain showed a small increasing effect on  $H_{max}$  with 3.59%. In contrast,  $t_{max}$  was achieved about 20 minutes later. The effect of 675 ppm of the inhibited papain is different from the effect of the active enzyme. 625 ppm of the active papain showed an increase of maximum slope with 29.59% and  $H_{max}$  with 20.31%.

### 4.2.3 Conclusion and outlook

It was possible to use the coomassie assay to ensure the protease activity of activated and inactivated papain prior to IC. Furthermore, the coomassie assay was used to verify the effect of a basic environment on the protease activity of papain. The results were reviewed *via* an SDS-PAGE. After inhibition of papain by NEM, a loss of protease activity of papain was observed *via* the coomassie assay. After 30 minutes of incubation in the basic solution, the protease activity monitored by the coomassie assay decreased by around one-third. A similar trend was observed using a basic substrate solution in the coomassie assay, where

the protease activity decreased. *Via* IC, the accelerating effect of 675 ppm of papain after inhibition decreased in contrast to the effect of the active enzyme. High concentrations of inhibited papain (675 ppm) showed only a small increasing effect on the hydration process (using 675 ppm of papain,  $H_{max}$  was increased with 3.59%). The slope increased by 2.33%, and  $t_{max}$  was achieved about 20 minutes later. In comparison to that, 625 ppm of the activated papain showed an increase in  $H_{max}$  with 20.31% and a maximum slope of 29.59%. The effect of 225 ppm of the active species was monitored with an increase in maximum slope with 1.52% and 4.97% for  $H_{max}$ . The time of achieving  $H_{max}$  was not shifted. In contrast to that, with 675 ppm of the inactive species,  $t_{max}$  is achieved around 20 minutes later, the maximum slope is increased with 2.33% and  $H_{max}$  with 3.59%. The effect of 675 ppm of the inhibited papain is even lower in comparison with the effect of 225 ppm of the active enzyme. The results of the IC give reason for the assumption that the active site of papain is partly responsible for the accelerating effect observed in the hydration process. Nevertheless, the effect observed of the enzyme is comparatively low. According to the decreased protease activity observed by the coomassie assay after basic incubation, it can be suggested that the basic cement environment lowers the enzyme activity. Additionally, infusibility of the enzyme is caused by the hardening of the cement paste. At this point, a next step could be to find an additive that is more resistant to conditions as the basic cement environment or to stabilize an enzyme like papain and make it more resistant to the basic cement environment.

# Conclusion and Outlook

A nucleation setup was designed including a titration setup, two sensors, a pH-sensor, and an optical sensor, combined with a closed Teflon beaker to monitor the calcium silicate hydration, the main binding phase in ordinary Portland cement, decoupled from the dissolution process. The titration setup was used to slowly mix the starting solution and adjust the time to supersaturation of the system. A supersaturated solution was designed to resemble the basic cement pore solution with high salinity. After the addition of the silicate species by titration, the system was supersaturated with regard to the calcium silicate hydrate phase but not supersaturated with regard to the portlandite phase. The pH sensor could provide useful information about the change in chemical composition in combination with the optical sensor for the change in turbidity *in situ*. The sealed Teflon beaker was designed to eliminate any intrusion of CO<sub>2</sub> into the system, thus preventing the carbonation of the highly basic solution. As the system is portable, it was combined with a powerful combination of *ex-situ* and *in-situ* methods to provide information about composition, morphology and structure over time. On the *ex-situ* side, the mechanism over time was analysed over time *via* cryo-TEM, SAED, EDX, ICP-OES and SLS. On the *in-situ* side, the change in the composition of the solution was analysed via DLS and SAXS. The combined experimental and theoretical results from scattering, STEM EDX, cryo-TEM and modelling allow for sketching a physico-chemical model for the nucleation of C-S-H, characterized by two turbidity drops that appear to be the consequence of two well-defined chemical steps. Our results describe the formation of C-S-H crystalline particles through a two-step mechanism *via* an X-ray amorphous intermediate. However, it is unknown whether the amorphous spheroids are in fact required for C-S-H formation in real cement pastes. Indeed, their amount and dispersion state would be crucial for building up the C-S-H network structure. A charge balance calculation showed that the speciation in the spheroids, based on the composition obtained by STEM/EDX, is very similar to that of  $\beta$ -C-S-H. The apparent negative charge deficit inside the spheroids may be explained by the presence of 72-100% of fully deprotonated silicate dimers. By modelling the electrostatic interactions in the framework of the primitive model, the composition allowed calculating the silicate dimer density associated with the Ca/Na ratio of 1.41 at equilibrium. Modeling results indicated that the density with respect to silicate inside the spheroids is  $\sim 19$  times lower than in the final C-S-H. Compared to C-S-H, the significantly lower silicate density inside the spheroids compared to C-S-H indicates that the transformation of the calcium silicate spheroids into final  $\beta$ -C-S-H is accompanied by a densification, specifically, water molecules are expelled.

This densification yields a variation of the surface charge density ( $\sigma$ ) which in turn has to drive the colloidal stability of the system. In contrast to the strong attractive forces between highly charged ( $\sigma = -4 \text{ e/nm}^2$ ) C-S-H platelets resulting from strong ion-ion correlation forces, the low charge density of the spheroids ( $\sigma = -0.6 \text{ e/nm}^2$ ) prevents them from aggregating because repulsive forces predominate. In this study, the focus was on using SAXS to determine the initial formation of the first particles in solution. A next task here is to evaluate the crystallization and aggregation at later stages to provide a better understanding of the driving forces in the reaction. Since a variation in pH has an accelerating effect on the crystallization and aggregation process, one could focus on these parameters. The stabilization of spheroids by polymers may be central to the frequent and adverse retardation observed with the use of the cationic polymers in this study. The effect of various cationic polymers was analysed in the designed setup, and the retarding effect on the nucleation of calcium silicate hydrates was monitored. The addition of a highly pH resistant protease papain to the cement accelerated the overall hydration in the more complex ordinary Portland cement system. When studying the effect of an extremely basic pH and high salinity on the activity of several proteases separately, *via* the coomassie blue dye assay, a strong decrease in protease activity was detected. At this point, a next step could be, finding an additive that is more resistant to the conditions of the basic cement environment or to stabilize an enzyme like papain to make it more resistant to the basic cement environment. *Via* the IC, the accelerating effect of papain after inhibition decreased in contrast to the effect of the active enzyme. This is a strong indication that the active site residue is involved and furthermore responsible and important for the accelerating effect on the hydration process. As the retarding effect of polymers like polycarboxylate ethers on the hydration process is not well understood, a next question to address in the model system is what effect the insertion of various polycarboxylate ethers has on the formation and stabilization of the spheroids. To make the system more complex, a next-level step was to combine the nucleation again with a constant dissolution of silicate species titrated over time. As the OPC pore solution has a high amount of potassium, a next step was to change the supersaturated starting solution by replacing a certain amount of sodium chloride with a potassium salt. As aluminum ions were reported to distort the local ordering in C-S-H, changing the starting solution by adding of an aluminium salt, can perhaps provide an explanation for the long-discussed influence of aluminum on C-S-H formation and the known poisoning effect of aluminum during the early stage of cement hydration. In this study, it was demonstrated, how advection, supersaturation, and certain additives influence intermediate formation. A fundamental understanding of the mechanism of C-S-H formation

at a molecular level is essential for rationally designing novel, cement-based construction materials. The implication will be a novel perspective and opportunity for “designing” the hydration process and the materials properties.

# Authors contributions

## Nucleation of C-S-H and the impact of polymers

### **Category 1**

*Conception and design of study:*

N. Krautwurst, L. Nicoleau, W. Tremel.

*Acquisition of data:*

N. Krautwurst, B. Barton, I. Lieberwirth, A. Fernandez-Martinez, T. Wohlhaupter.

*Analysis and/or interpretation of data:*

N. Krautwurst, L. Nicoleau, W. Tremel, A. Fernandez-Martinez, I. Lieberwirth, C. Labbez.

## Influence of Biomolecules on Cement Hydration

### **Category 1**

*Conception and design of study:*

N. Krautwurst, N. Loges, W. Tremel, H. Paulsen, C. Cerfass

*Acquisition of data:*

N. Krautwurst, A. Götz

*Analysis and/or interpretation of data:*

A. Götz, N. Krautwurst, C. Cerfass, H. Paulsen, W. Tremel, N. Loges

# Appendix

## A1. Synthesis and titration set-up

Potentiometric and turbidimetric measurements were performed using a computer-controlled system from Metrohm (Filderstadt, Germany), operated with the custom-designed software Tiamo (v2.4). The setup consists of a titration device (Titrand 905) that controls two dosing units (Dosino 800). The system is supplemented by a pH module (Metrohm, pH module 867). The pH in the sample was monitored in real time with a glass iUnitrode electrode (Metrohm, No. 6.0278.300) while the turbidity of the samples can be monitored with an optical sensor (Spectrosense, Metrohm No. 6.1109.110). All experiments were carried out in a lab-built PTFE titration vessel (Fig. A1). The vessel was closed and protected from the atmosphere in order to minimize potential artifacts that may arise from diffusion of atmospheric CO<sub>2</sub> or evaporation of the solution. The room temperature was controlled at  $T = 293.15$  K.

A solution supersaturated with respect to calcium silicate hydrate and undersaturated with respect to portlandite was used as starting solution. The chemicals used and the ion concentrations of the different supersaturated solutions are shown in Table A1 and S2. The desired pH of 12.86 was reached by addition of sodium hydroxide (solution at 1 M). In order to ensure the same high ionic strength, sodium chloride was added to the solution in order to reach an ionic strength  $I = 0.245$  M. To prevent carbonation of the supersaturated solution, all solutions were freshly prepared with nitrogen purged deionized water. In addition, all experiments were performed in a closed Teflon vessel by passing a dry nitrogen flux. The freshly prepared solutions were filtered with a Millex-GV, 0.22  $\mu$ m, PVDF, 33 mm to prevent the intrusion of dust. The sodium metasilicate solution was added with a dosing speed of 1.2 mL/min while the solution was stirred (stirring speed: 960 rpm).

## A2. Measures against and control of solution carbonation

To avoid the carbonation of the solution during C-S-H formation, all solutions were freshly prepared with nitrogen purged deionized water. The experiments were performed in a closed Teflon vessel by passing a dry nitrogen flux (for more detail see methods). An aliquot of the starting solution was analyzed to evaluate the carbonation of the solution. With the titrimetric barium carbonate method, the carbonate content of the supersaturated basic solution was calculated. For the titrimetric barium carbonate method, the amount of carbonate was precipitated in excess with 5 wt.-% (w/v) barium chloride and back-titrated with hydrochloric acid (Fig.S2).

A second equivalence point was observed in the starting solution and the amount of carbonate was monitored without the preparation of the starting solution. In contrast, no carbonate was monitored in the starting solution by using the nitrogen purged and freshly prepared solutions.

## A3a. TEM/STEM EDX

Transmission electron microscopy (TEM) was carried out on a Tecnai 12 transmission electron microscope equipped with field emission gun and working at 120 kV. TEM



snapshots were prepared by taking a drop of the crystallization solution during the *in situ* measurement and placing it on copper grids coated with amorphous carbon. Scanning electron microscopy (STEM) images were obtained with a FISCHONE high angular annular dark field (HAADF) detector and elemental analysis was performed by energy-dispersive X-ray (EDX) spectroscopy and quantified by EDAX Genesis (Version 6.4.1.). The spacing of the atomic planes was obtained by a profile plot (Image J: Image J 1.50a, National Institutes of Health, USA, Java 1.6.0\_46).

### A3b. Cryo-TEM/NAED

Frozen-hydrated (cryo) samples were prepared by drop-casting a C-S-H suspension on a TEM grid covered by holey carbon film (Quantifoil 2/2), followed by blotting and plunge-freezing in liquid ethane (Gatan Cryoplunge 3). For the subsequent examination this specimen was transferred to a TEM (FEI Tecnai F20) keeping cryogenic conditions using a cryo TEM holder (Gatan 926). The cryo-TEM measurements were performed at 120 kV with a Tecnai 12 (FEI, Hillsboro, OR, USA) equipped with a BIO-TWIN-lens and a 2kx2k CCD by Gatan (Pleasanton, CA, USA). For electron diffraction measurements the operation mode of the TEM was adjusted to the nano area diffraction mode (NAED). By inserting a small 10  $\mu\text{m}$  C2 condenser lens a fine, a parallel beam was formed which could be focused to a diameter of several nm. Since the vitrified water as well as the sample are extremely beam sensitive, the total beam current was reduced to approx. 5 pA. The electron diffraction was recorded on a 2k CCD camera at binning 4 using an exposure time of 500 ms.

### A3c. Protocol and preparation of solutions for ICP OES measurements

Inductively-coupled plasma equipped with optical emission spectroscopy (Spectro Ciros Visions ICP-OES) was used to determine the silicon and calcium content in the solution. At designated time intervals, 0.2 mL of the suspension were collected and centrifuged for 5 minutes at 5000 rpm to separate the solution from larger particles for analysis. The supernatant was acidified to stop the reaction with nitric acid (8 M) and diluted with deionized water. In order to achieve the highest precision, the calibration was performed by taking into account matrix-matching, i.e, the calcium and silicon standards were prepared with the same concentration in NaCl as in samples.

### A3d. Light scattering and data evaluation

The light scattering cuvettes and the titration setup were cleaned by flushing with acetone for 30 minutes. All filtering steps were carried out in a flow box to avoid contamination by dust. After addition of the metasilicate solution into the calcium hydroxide solution, an aliquot of the resulting mixture was filled into a cylindrical quartz glass cuvette (Hellma, 20 mm outer diameter), and the cuvette was closed which marks the starting point of the light scattering measurements.

## Static light scattering

The SLS setup consists of a He-Ne laser (Uniphase, 22 mW,  $\lambda = 632.8$  nm), a SP86 goniometer with ALV3000 correlator (ALV GmbH Langen) with ALV High QE APD Avalanche photodiode and detection at  $T = 293$  K (Huber thermostat, ministat). The scattering intensity was recorded between  $\theta = 0^\circ$  to  $150^\circ$  with angular step size at  $5^\circ$ . The radius of gyration ( $R_g$ ) was extracted from the scattering data by using the Guinier approximation:

$$\ln I_s(q) = \ln I_i - \frac{q^2 R_g^2}{3} \quad (\text{A.1})$$

$R_g$  is defined as the mass weighted average distance from the core of a molecule to each mass element in the molecule and yields a mass-weighted length scale of the scattering object:

$$R_g^2 = \frac{\sum m_i r_i^2}{\sum m_i}$$

(A.2) With  $m_i$  is the mass of the  $i^{\text{th}}$  atom in the particle and  $r_i$  is the distance from the center of mass to the  $i^{\text{th}}$  particle. (59)

## Dynamic Light Scattering

For the dynamic light scattering experiments a small amount of the freshly prepared supersaturated solution was analyzed. The light scattering cuvettes were cleaned by flushing with acetone for 30 minutes and filtering steps were carried out in a flow box to avoid contamination by dust. All experiments were performed at a temperature of  $T = 293.15$  K. The DLS setup consists of an ALV-CGS-8F SLS/DLS 5022 goniometer and Avalanche photodiode detector. A He-Ne laser ( $\lambda = 632.8$  nm,  $P = 22$  mW) was used. Measurements were carried out at eight different angles ( $29.9^\circ$ ,  $49.9^\circ$ ,  $63.9^\circ$ ,  $80.9^\circ$ ,  $97.9^\circ$ ,  $114.9^\circ$ ,  $131.9^\circ$  and  $148.9^\circ$ ). The analysis was performed with HDRC (version 6.3.1.). A bi-exponential function was fitted to the field correlation function  $g_1$  at a fixed angle:

$$g_1 = a_1 \cdot e^{-D_1 q^2 r} + a_2 \cdot e^{-D_2 q^2 r} \quad (\text{A.3})$$

The apparent diffusion coefficient  $D_{app}$  was calculated from the scattering vector  $q$ ,  $a_i$  as the amplitude, which represents the intensity weighted contribution of  $D_1$  and  $D_2$  to the correlation function:

$$\langle D_{app} \rangle = \frac{a_1 D_1 + a_2 D_2}{a_1 + a_2} \quad (\text{A.4})$$

Due to the growing particles, the correlation function yields an apparent diffusion coefficient. The baseline was subtracted before the fit. The apparent hydrodynamic radius  $R_{H,app}$  was calculated by applying the Stokes-Einstein equation with the diffusion coefficient  $D$ , the solvent viscosity  $\eta$  (for water with a value of  $1002.0 \cdot 10^{-6}$  kg m<sup>-1</sup>s<sup>-1</sup> at 293.15 K), the Boltzmann constant  $k$  and the temperature  $T$ : (59)

$$R_{H,app} = \frac{kT}{6\pi\eta\langle D_{app} \rangle} \quad (\text{A.5})$$

$R_{H,app}$  is defined as the radius of an equivalent hard sphere diffusing at the same rate as the object under observation. As the monitored objects do not exist as hard spheres, the determined hydrodynamic radius more closely reflects the apparent size adopted by the solvated, tumbling molecules. The way in which  $R_H$  and  $R_g$  is calculated means that the value itself is slightly more dependent on the structure of the molecule of interest than the value of  $R_H$ . The ratio of  $R_g$  to  $R_H$  ( $R_g/R_H$ ) provides information about shape, i.e. particle morphology. Combining static and dynamic light scattering, the structure factor  $\rho$  is defined as follows:

$$\rho = \frac{R_g}{R_{H,app}} \quad (\text{A.6})$$

### A3e. Small Angle X-Ray Scattering

All time-resolved small angle X-ray scattering (SAXS) measurements were carried out at beamline I02 at the ESRF. The setup uses the monochromatic, highly collimated, and intense beam in a pinhole configuration with sample-to-detector distance variable from 0.6 m to 30 m. Experiments were performed using a monochromatic X-ray beam at 12.4 keV and two-dimensional (2D) scattered intensities were collected at small-angles with a Pilatus 300K (2D large area pixel-array detector<sup>49</sup>). Transmission was measured by means of a photodiode installed in the beam-stop of the SAXS detector. For each experiment a series of backgrounds and reference samples were measured including: the empty capillary cell, cell filled with water and cell filled with the initial, unmixed  $\text{CaCl}_2$  solution at the used concentration and temperatures. In all SAXS measurements, the acquisition time per frame varied between experiments (from 1 to 30 s per frame). This time frame was based on previously off-line tested reaction times for the various conditions. A Kapton capillary (ID = 0.1461 cm) was used for the measurements through which solution was allowed to flow. This setup maintained a constant X-ray beam over the course of a single experiment, allowing SAXS patterns taken at different times to be quantitatively compared. Solutions flowed continuously through the capillary over the course of the experiment using peristaltic pumps at the inlet and outlet with a flow rate of  $\sim 100$  mL/h.

In a general way, the intensity scattered at low angles can be approximated by:

$$I_{SAXS} = I(0)P(q)S(q) \quad (\text{A.7})$$

where  $I(0)$  is proportional to the total number of scatterers.  $P(q)$  and  $S(q)$  represent the form and structure factor, respectively. The high dilution conditions of the system under study justify the use of a model of non-interacting particles, which makes  $S(q) = 1$ .  $P(q)$  is the Fourier transform of the electronic density of the particles. Here, a model using a log-normal distribution of non-interacting spherical particles is used:

$$P(q) = (\Delta\rho)^2 \int n(r, R, \sigma) V^2 \frac{9(\sin(qR) - qR\cos(qR))^2}{(qR)^6} dR \quad (\text{A.8})$$

where  $V$  and  $\Delta\rho$  are the particle volume and the electronic density difference (or contrast) between the particle and the surrounding solution. The probability density function of the log-normal distribution is given by:

$$n(r, R, \sigma) = \frac{1}{\sigma\sqrt{2\pi}r} \exp\left(-\frac{[\ln(r)-R]^2}{2\sigma^2}\right) \quad (\text{A.9})$$

where  $q$  is the scattering vector,  $R$  is the average of the distribution and  $\sigma$  is the standard deviation or shape parameter. This distribution was shown to give an accurate description of size distributions of grains obtained from nucleation and growth processes.<sup>(105)</sup> Modeling of background-corrected SAXS data was performed using the software IRENA.<sup>(106)</sup>

### A3f. Electrophoretic mobility

The electrokinetic potential of the reaction product was measured by electrophoresis. The apparatus used for the determination of the electrokinetic properties was a Zetasizer (Nano ZS 3600, Malvern Instruments Ltd., UK). The electrophoretic mobility was measured through Laser Doppler Velocimetry. Each measurement was repeated 6 times.

### A4. Thermodynamic calculations

The ion activities were calculated with the speciation software Phreeqc v2.13. The relevant chemical equations implemented in the database used for the speciation is shown in Table A2. The activity coefficients were calculated with the extended Debye-Hückel equation which obviously remains an approximation. Nevertheless, we used it with a sufficient degree of confidence since the ion concentrations was rather low and the known ion-pairing was accounted for the cations bound to hydroxide and silicate ions. The concentrations of the calcium silicate complexes were determined in the respective concentration range and implemented in the database. The concentration of  $\text{OH}^-$  was obtained from the charge balance. The thermodynamic model used for C-S-H stems from the literature<sup>(85)</sup> but the original C-S-H solubility products were refitted taking the calcium silicate complexes into account.

For any reaction  $x\text{A} + y\text{B} = \text{A}_x\text{B}_y$  at equilibrium,  $\Delta G$  the change in free energy is zero which can be written as follows:

$$\Delta G = \Delta G^0 + RT \ln(\text{A})^x(\text{B})^y \quad (\text{A.10})$$

$$\Delta G = -RT \ln K \text{ and } K = (\text{A})_{\text{eq}}^x (\text{B})_{\text{eq}}^y \quad (\text{A.11, A.12})$$

with  $R$ ,  $T$  and  $(j)$  the gas constant, the absolute temperature and the activity of  $i$ .  $\Pi$ , the ion activity product is defined as:

$$\Pi = (\text{A})^x(\text{B})^y \quad (\text{A.13})$$

$\beta$ , the saturation degree is then defined as the ratio between the ion activity product and the solubility product, and, the saturation index ( $S$ ) as the logarithm of the saturation degree:

$$\beta = \frac{\pi}{K} \text{ and } SI = \log \beta \quad (\text{A.14, A.15})$$

both being considered as a deviation from equilibrium. For the reference solution 1 (Table A4), we present below the results of the Haas and Nonat model. The most stable phase according to the model is  $\beta$ -C-S-H. The model is based on two types of surfaces: an external (labelled  $e$ ) and an internal surface (labelled  $\lambda$ ). The internal surface must be neutral, but the external surface may be positive or negative depending on pH conditions and the amount of  $\text{Ca}^{2+}$  as defined by the adsorption constants. Different silicate species refer to these surfaces and can be either protonated or deprotonated or bound to  $\text{Ca}^{2+}$  or bound to  $\text{CaOH}^+$  (Table A5). The supersaturations with respect to C-S-H phases were calculated with the speciation software Phreeqc according to the Haas and Nonat model,<sup>(85)</sup> but the C-S-H solubility constants were refitted from their original experimental dataset after adding the calcium silicate complexes to the database (Table A6).

#### A5. Turbidimetric measurements

Time-dependent turbidity was measured with an optical sensor which consists of a light source, two glass fiber (light) guides, a concave mirror, and an amplifier. The monochromatic light from the first light guide passes through the solution where it is partially absorbed or scattered by the sample. A voltage signal is produced in the amplifier and transmitted to the titrator via the electrode input.

In our system, the turbidity was measured as the decrease of potential resulting from light scattering of the formed C-S-H species. The system was a dilute solution ( $c \leq 0.1$  wt-%). The light scattering from dilute solutions is independent of the scattering angle and the scattering from density fluctuations of the solvent itself is ignored. The voltage signal only depends on the scattering power of suspended particles and their mass concentration.<sup>(59)</sup> LUDOX colloidal silica solutions (SM-30, AS-30 and AS-40 by Sigma Aldrich, see Table A6) containing particles of distinctive sizes were analysed to evaluate the detection limit and the capabilities of the optical sensor (Fig. A3). A decreasing voltage was measured for SM-30, AS-30 and AS-40 with increasing mass concentration. The optical sensor was able to detect 7 nm sized colloidal silica particles at a concentration of 0.05 wt-%. With increasing concentration ( $c > 0.1$  wt-%), the transmitted intensity was not proportional to the square of the particle mass, and the system approaches a region of multiple angle scattering.

#### A6. The silicate speciation in spheroids and $\beta$ -CSH according to EDX patterns

The characterization by EDX allows determining the amount of  $\text{Ca}^{2+}$ ,  $\text{Na}^+$ , Si and  $\text{Cl}^-$  ions. The balance between negative and positive charges allows to determine the charge of the silicate ions in order to satisfy the electroneutrality condition in the solid/spheroid. This provided information about the speciation of those ions in the spheroids. Two unknowns, the amounts of hydroxide and  $\text{H}^+$  ions remained to be determined.  $\text{H}^+$  was considered to be bound to silicate ions and  $\text{OH}^-$  bound to calcium ions either as an ion pair in solution or as co-ion if  $\text{Ca}^{2+}$  is complexed by silicates. First, the experimental composition of the final C-S-H product was compared to the model of Haas and Nonat.<sup>(85)</sup> In this model,  $\beta$ -CSH only contains silicate dimers and pentamers, and the silicate mean chain length calculated by the model is 2.19. If  $x$  is the proportion of dimers, it comes:

$$x*2 + (1-x)*5 = 2.19 \text{ and } x = 0.94\% \quad (\text{A.16})$$

The protonation was calculated from the speciation in section 4, and 21.1% of the silicate are protonated. It turns out that the mean charge on a silicate tetrahedra in dimer was -2.37 and -1.89 for a silicate tetrahedra in pentamer. The fraction of  $\text{CaOH}^+$  bound to Si was  $(1.812 + 0.08989)/4.37/2 = 21.8\%$  of all Ca. According to this speciation, the charge balance gave a slight excess of positive charges (case A in Table A8), which can be seen as a reasonable error (~5%) according to the experimental uncertainty from EDX. For further comparison we refined the model to achieve electroneutrality by changing the  $\text{Ca}^{2+}/\text{CaOH}^+$  ratio (case B in Table A8). A variation of the degree of protonation would lead to a change of the Ca/Si ratio and a disagreement with the experimental value.

In a second step, the composition of the spheroids was examined. In the first case (case 1), the speciation was chosen to be identical to that of the solution. Here, one quarter of Ca was present as  $\text{CaOH}^+$  and three quarters as  $\text{Ca}^{2+}$  based on the Ca speciation.  $\text{H}_3\text{SiO}_4^-/\text{H}_2\text{SiO}_4^{2-}$  were the main silicate species and almost equally distributed. With this speciation, there was a high excess of positive charges leading to the conclusion that the composition of spheroids significantly differ from the solution. The lack of negative charges in this first calculation indicated that the silicate ions are more deprotonated than in solution. The only reasonable hypothesis is that they tend to dimerize and they are highly deprotonated as in  $\beta\text{-C-S-H}$ . Based on this hypothesis it was possible to estimate the amount of dimers if the two limiting cases (case 2 and case 3, Table A8) were considered, which correspond to the limit-cases for Ca speciation. The spheroids contained between 72%-100% of silicate dimers in order to satisfy the electroneutrality condition. This calculation shows that the speciation of Si and Ca in the spheroids was close to that in  $\beta\text{-C-S-H}$ .

#### A7. Model and simulation.

The interaction free energy between the spheroids was obtained from the model described in fig. S8. The model used is the same as in (85) and is here only briefly described. The model consists of two planar and parallel surfaces with a uniform surface charge density, namely the spheroids are only described by their surface. The slit formed by the two parallel surfaces is filled with an electrolyte solution described at the level of primitive model. That is, the ions are explicitly modeled as charged hard spheres of diameter  $d = 4 \text{ \AA}$  while the solvent is implicitly treated as a dielectric continuum. The pair potential between two ions separated a distance  $r$  is given by:

$$U(r) = \begin{cases} \frac{Z_i Z_j e^2}{4\pi\epsilon_0\epsilon_r r}, & r > d_{hc} \text{ and } \infty, \\ \infty, & r \leq d_{hc} \end{cases} \quad (\text{A.17})$$

where  $Z_i$  is the valency of species  $i$ ,  $e$  is the elementary charge and  $\epsilon_0$  and  $\epsilon_r$  are the permittivity of vacuum and the dielectric constant of the solvent ( $\epsilon_r = 78.7$ ). Periodic conditions are applied in the two directions parallel to the surfaces using the charged method.(106) The osmotic pressure of the confined solution is calculated at the midplane (mp) according to,

$$p_{osm} = k_B T \sum_i c_i(\text{mp}) + p^{hc} + p^{corr} \quad (\text{A.18})$$

where superscripts <sup>corr</sup> and <sup>hc</sup> stand for correlation and hard core. As clearly seen from this expression, the osmotic pressure is the sum of three terms, two with a repulsive contribution, i.e. the hard core and ideal contribution to the pressure and the correlation pressure induced by the ion correlations on each side of the midplane which give an attractive contribution to the pressure. Details on the calculation of these terms can be found elsewhere. (107) The net osmotic pressure is obtained by subtracting off the bulk pressure.  $W(h)$ , the interaction free energy per surface area for two surfaces separated by a distance  $h$  is obtained by integrating the osmotic pressure:

$$W(h) = -\int_{\infty}^h p_{osm}(h') dh' \quad (\text{A.19})$$

Finally, the interaction force  $F(h)$  between two spheroids of radius  $R$  can be obtained by applying the Derjaguin approximation:

$$F(h) = \pi R W(h) \quad (\text{A.20})$$

This model was solved using Monte Carlo simulations in the Grand Canonical ensemble, that is, in addition to a fixed volume and temperature ( $T = 298$  K), the chemical potential for the salt ions was maintained fixed. We use the standard Metropolis algorithm. (108) The chemical potentials for the simple salt pairs were calculated in a separate simulation using the modified Widom method. (109)

#### A8. Isothermal Calorimetry

The hydration of OPC (Milke CEM I 52.5N) with enzymes was investigated using a TA instrument TAM Air calorimeter. The water-to-cement ratio was 0.45. The mixing water was weighed into small glass vials, and the additive was added to the water. The solid was weighed directly in the calorimetry ampoules. After adding the solution to the solid, the mixture was stirred manually with a metal spatula (stirring for 60 seconds, 30 seconds break and 30 seconds stirring). The mixture was then transferred to the calorimeter. To exclude the effect of buffer salts on the hydration process, the additives were purified *via* the spin column method and supplied in a 50 mM sodium acetate solution (pH 7.0) (more detail, see 3.2.2.2. and Table A13-18 and Table A21). The effect of a 50 mM sodium acetate buffer was examined as the blank measurement.

#### A9. Activation of papain

Papain was activated by dissolving it in a solution containing 1.1 mM EDTA, 6 mM mercaptoethanol, and 5.5 mM cysteine-HCl for 30 minutes (0.05-0.1 mg/mL). After standing for 30 minutes, the solution was passed through a 30kDa Amicon® Ultra-4 Centrifugal Filter Unit (diameter: 17.2 mm, Ultracel regenerated cellulose membrane) which was preequilibrated with 0.05 M sodium acetate buffer (pH 7.0). The enzyme was concentrated in the filter and washed several times with 0.05 mM sodium acetate buffer (pH 7.0). According to the manufacturer, the fraction contains 90-95% of the total protein.

### A9.1. Inhibition by N-ethylmaleimide

The inhibition of the papain was done by N-ethylmaleimide acting as an alkylating reagent. Here, the enzyme's catalytic activity is inhibited by the chemical modification of the essential cysteine residue. The reaction was found to be completely irreversible. The activity of papain was evidenced by the coomassie blue dye binding after the inhibition. The N-ethylmaleimide (NEM), the papain from papaya latex (Suspension in 0.05 M sodium acetate, pH 4.5, containing 0.01% thymol), and the sodium acetate buffer were supplied by the Sigma Chemical Co. To inhibit the activated enzyme, 26 mg NEM was added to papain solution (3mg/mL) and incubated for 30 minutes. The papain from papaya latex (buffered aqueous suspension\*) and the sodium acetate buffer were supplied by the Sigma Chemical Co.

### A10. Purification

The purification was done with a 30 kDa Amicon® Ultra-4 Centrifugal Filter Unit (diameter: 17.2 mm, Ultracel regenerated cellulose membrane) which was pre-equilibrated with 0.05 M sodium acetate buffer (pH 7.0). The reagent was concentrated by centrifugation at room temperature for 1 hour at 5500 rpm (rotor 6000 from Hettich) and washed several times with 0.05 M sodium acetate buffer (pH 7.0).

### A11. Coomassie brilliant blue G-250-based colorimetric assay

“The coomassie brilliant blue G-250-based colorimetric assay was performed for measuring the protease activity. This involves incubating the protease with Casein as a substrate, followed by the removal of an aliquot to which coomassie brilliant blue G-250 dye reagent is added. The assay is based on the observation that the dye interacts only with the substrate Casein but not with the proteolytic products (small peptides and amino acids). (103) Prior to analysing the protease activity of papain, the effect of the substrate Casein on the dye was analysed. Besides analysing the protease activity of the activated and inactivated papain protease, the test was used to analyse the effect of a basic environment on the protease activity of papain. On the one hand, the enzyme was incubated in a basic milieu before the test was done, and on the other hand, the pH of the substrate solution was increased to 12. Bio-rad protein dye reagent concentrate [0.05% (w/v) coomassie brilliant blue G-250, 23.5% (w/v) ethanol and 42.5% (w/v) phosphoric acid] was supplied by the Sigma Chemical Co. The papain from papaya latex (buffered aqueous suspension) and the buffer solution (disodium hydrogen phosphate/sodium hydroxide solution, pH 12) were from the Sigma Chemical Co., as well. Solutions of activated and inhibited papain were prepared with distilled water (0.7, 0.2 and 0.1 mg/mL). After the activation of the enzyme, an incubation in a basic buffer solution of pH 12 was performed (0.7 mg/mL). After an incubation of 30 minutes, the coomassie assay was done. A solution (2 mg/mL) of Casein was prepared with 50 mM Tris-HCl (pH 8.8). The solution was stirred at 85 °C for a total of 30 minutes. Afterwards, the solution was filtered with a Miniart SRP 15 (PTFE-membrane, pore size 0.45 µm). The substrate solution was adjusted to a pH of 12 by a 2 M sodium hydroxide solution.



#### A12. Coomassie blue spectra

One hundred microlitres of 50% Bio-rad reagent concentrate (containing 0.025% coomassie blue G-250) were added to water to make a final volume of 1 mL. When desired, Casein (0.025, 0.05, 0.075, and 0.1 mg) was also added. Absorbance scanning was done on an Infinite M 1000 reader using the software I-Control from Tecan (400-700 nm).

#### A13. Casein-coomassie blue microplate assay

200  $\mu$ L Casein solution (0.5 mg/mL in 50 mM Tris-HCl, pH 8.8) and 50  $\mu$ L protease solution (0.7, 0.2 and 0.1 mg/mL in distilled water) were added to a well on a Microtiter plate (96 Well polystyrene microplate from Greiner). After incubation for 30 minutes at 25 °C, 100  $\mu$ L aliquots of the reaction mixture were transferred to another well containing 50  $\mu$ L water and 100  $\mu$ L of Bio-Rad dye reagent concentrate, diluted 1:5 with phosphoric acid/ethanol/water solution before the final experiment (total volume 250  $\mu$ L). After 10 min, the plate was read on an Infinite M 1000 reader using the software I-control from Tecan at an absorbance of 595 nm. Each experiment was repeated three times. For the test with papain incubated in basic pH, 50  $\mu$ L of the enzyme/basic buffer solution were added to 200  $\mu$ L Casein solution. To analyse the effect of a basic substrate solution, the 200  $\mu$ L Casein solution were replaced by 200  $\mu$ L of the basic substrate solution. Each experiment was repeated three times.

#### A14. Gel electrophoresis: polyacrylamide gel electrophoresis

The gel electrophoresis was examined for controlling the substrate solution and enzyme solution prior to the coomassie assay. It was thus possible to determine the molar mass and roughly estimate their concentrations before and even after the test. Polyacrylamide gel electrophoresis (PAGE) is a technique used in biochemistry to separate biological macromolecules according to their electrophoretic mobility. Mobility is a function of the length and conformation of the molecule. For proteins, sodium dodecyl sulphate (SDS) is an anionic detergent applied to a protein sample to linearize proteins by imparting them with a negative charge. In most proteins, the binding of SDS to the polypeptide chain imparts an even distribution of charge per mass unit, thereby resulting in a fractionation by approximate size during electrophoresis. The discontinuous method of Laemmli for applying small proteins was chosen, as the stacking limit for large proteins in the Laemmli system lies far beyond 100 kDa. The SDS, Tricine p.A., urea p.A., glycerol p.A., acrylamid 2x cryst., bisacrylamid 2x cryst., Pyranin (8-hydroxy-1,3,6-pyrenetrisulfonic acid), and Serva blue G were obtained from Serva. The tetramethylethylenediamine (TEMED) was purchased from Sigma, and the Tris was from Boehringer-Mannheim. The ammonium persulphate and bromphenol blue were purchased from Merck (Darmstadt). The composition of these acrylamide mixtures and of all of the gels is defined by the letters T and C according to Hjerten. T denotes the total percentage concentration of both monomers (acrylamide and bisacrylamide). C denotes the percentage concentration of the crosslinker relative to the total concentration T. All solutions were kept at room temperature with the exception of the acrylamide : bisacrylamide mixtures, which were stored at 4°C. The 10% T, 3% C gel was used as a uniform separating gel, only overlaid by a 4% T, 3% C stacking gel (2 cm). Separating and stacking gels were polymerized together, without prior degassing, by the

addition of 150  $\mu$ L of a 10% ammonium persulphate solution and 15  $\mu$ L of TEMED/30 ml. It is essential that the separating gel polymerizes first. All other gels were composed of a small-pore gel (16.5% T) overlaid by a 10% T, 3% C spacer gel (2-3 cm) which was again overlaid by the 4% T, 3% C stacking gel (1-2 cm). The small-pore gel and the short 10% T-spacer gel (without glycerol) were polymerized together within 15 min by the addition of 100  $\mu$ L of 10% ammonium persulphate and 10  $\mu$ L of TEMED to 30 ml of each mixture. The 10% T gel was again overlaid with water. Several minutes after termination of the polymerization, the water was replaced by the 4% T-stacking-gel mixture polymerized by 100  $\sim$ 1 of 10% persulphate and 10  $\sim$ 1 TEMED per 12.5 ml. The 10% T gel between the stacking and small-pore gels was omitted when the resolution of proteins below 5 kDa was of minor interest. The protein samples were incubated for 30 min at 40°C in 4% SDS, 12% glycerol (w/v), 50 mM Tris, 2% mercaptoethanol (v/v), and 0.01% Serva blue G in water, adjusted with hydrochloric acid to pH 6.8. Serva blue G was used as the tracking dye, although it migrated as a broad band. It ran only a little faster than the smallest proteins in all gels, whereas the commonly used bromphenol blue ran behind the smallest proteins in 10% T, 3% C gels but ahead of them in high-percentage acrylamide gels. Usually, the filling height of the sample was 2.5-10 mm. Slab gels were used in a vertical apparatus. The aluminium plates were never in contact with the electrode buffers. A very similar apparatus (No. 30442) is available from Renner GmbH (Dannstadt, FRG). The protein bands were fixed in a solution containing 50% ethanol and 10% acetic acid for 5 min (0.7 mm gels), or for 60 min (1.6 mm gels), before they were stained with 0.025% Serva blue G in 7% acetic acid for 1-2 h, depending on the thickness and composition of the gels. A complete background destaining of the 0.7 mm gels was achieved by shaking the gels in 10% acetic acid for 2 h. The destaining solution was renewed every 30 minutes. Rapid "fixing", staining, and destaining was essential in the case of small proteins to avoid their elution."

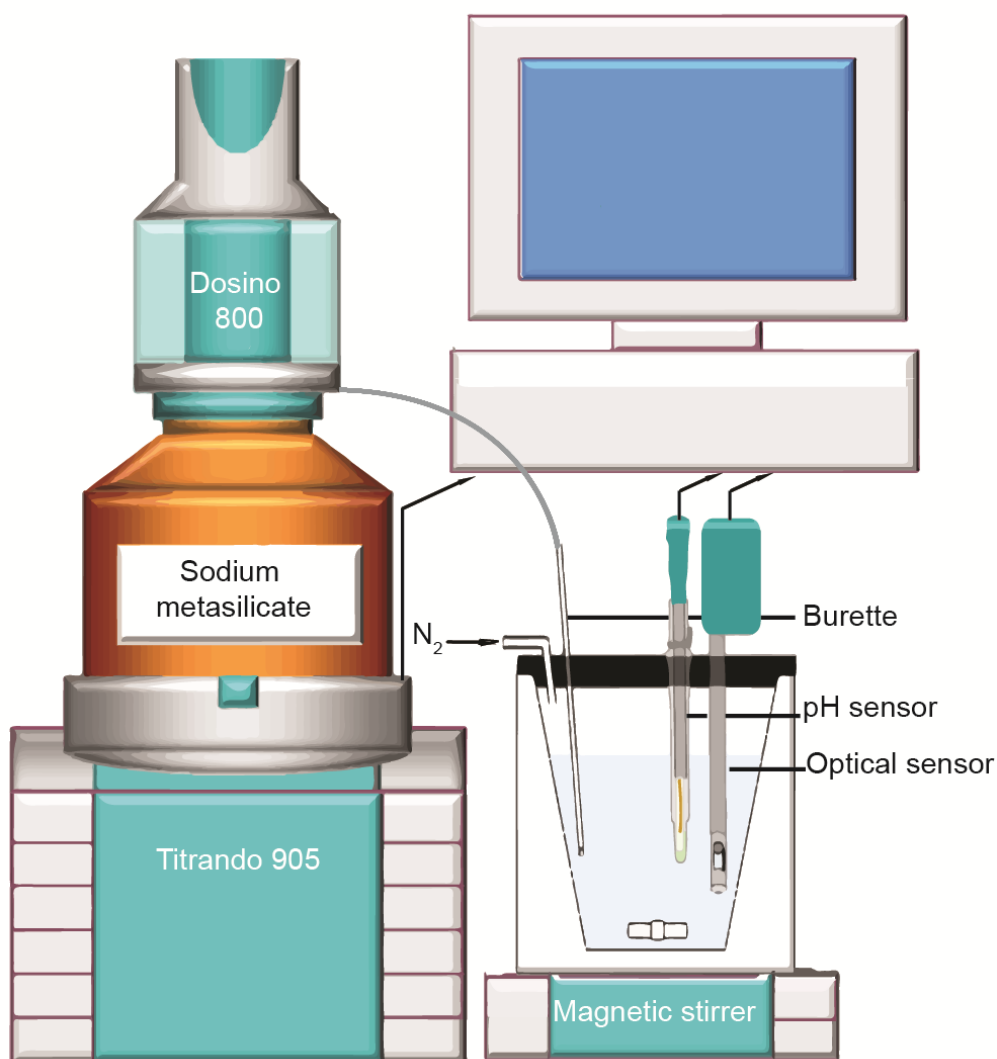


**Fig. A1. Schematic overview of the titration setup.** The magnetic stirrer and titration device (Titrand 905) is controlled by a computer and operates a dosing unit (Dosino 800) for the addition of sodium metasilicate solution. Two sensors are connected: a pH probe and an optical sensor. All experiments were carried out in a lab-built PTFE vessel.

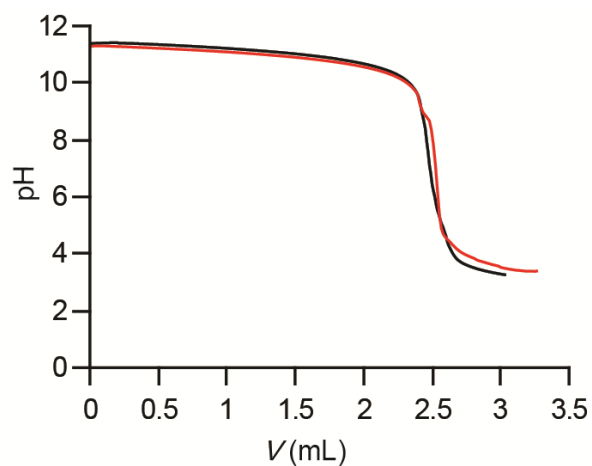


**Fig. A2.** The titration curves of the titrimetric barium carbonate method of the starting solution (solution 1, red) and the control without solution carbonation (black).

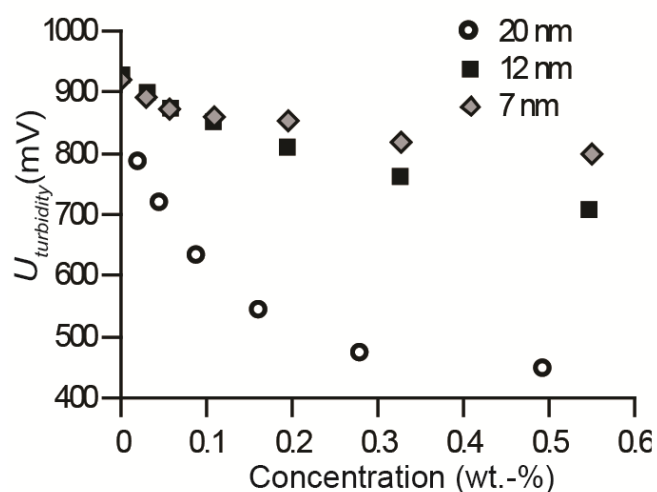


**Fig. A3.** The turbidity of colloidal silica solutions over concentration.

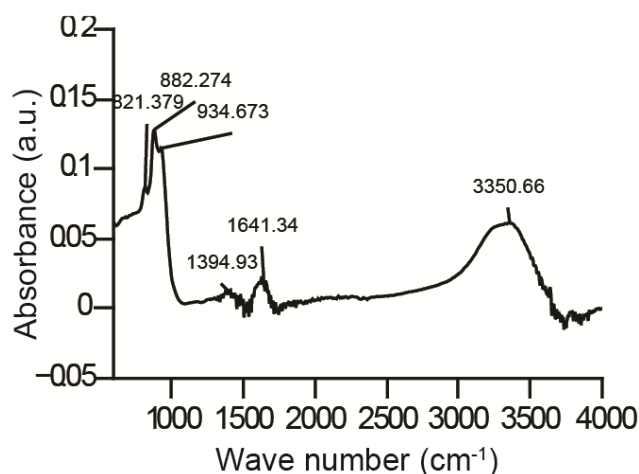


**Fig. A4.** IR spectrum of the reaction product after 1000 minutes. The band at 660–670 cm<sup>-1</sup> is due to Si–O–Si bending and the group between 950–1100 cm<sup>-1</sup> can be assigned to Si–O stretching. The presence of water in the reaction product after 1000 minutes is evidenced by the  $\nu_2$  band maxima between 1364–1641 cm<sup>-1</sup> and the broad band between 2500–3700 cm<sup>-1</sup>, corresponding to the O–H stretching band.

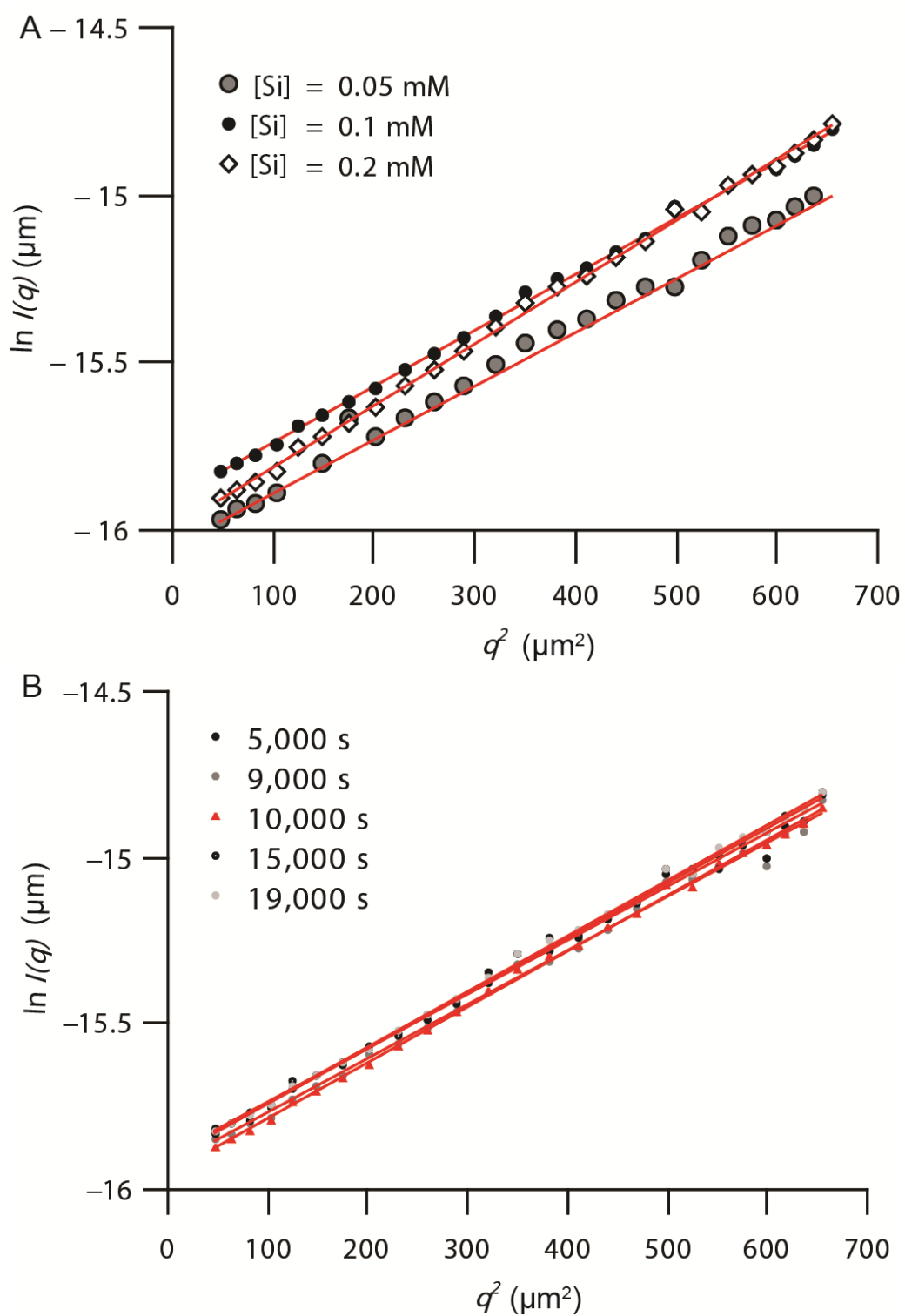


**Fig. A5. Guinier plots.** Guinier plots for experiments with (A) different silicate concentrations (0.05 mM, 0.1 mM, 0.2 mM) after 330 minutes and (B) over time with [Si] = 0.1 mM.

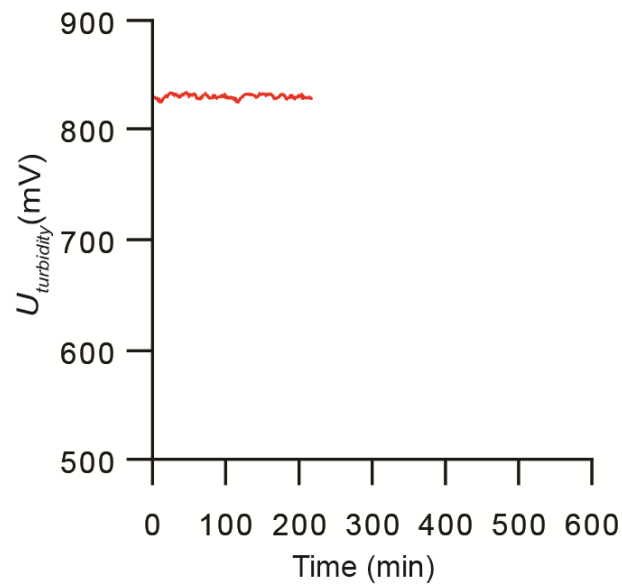


**Fig. A6.** The turbidity over time for a solution devoid in calcium (solution 6, Table A2).

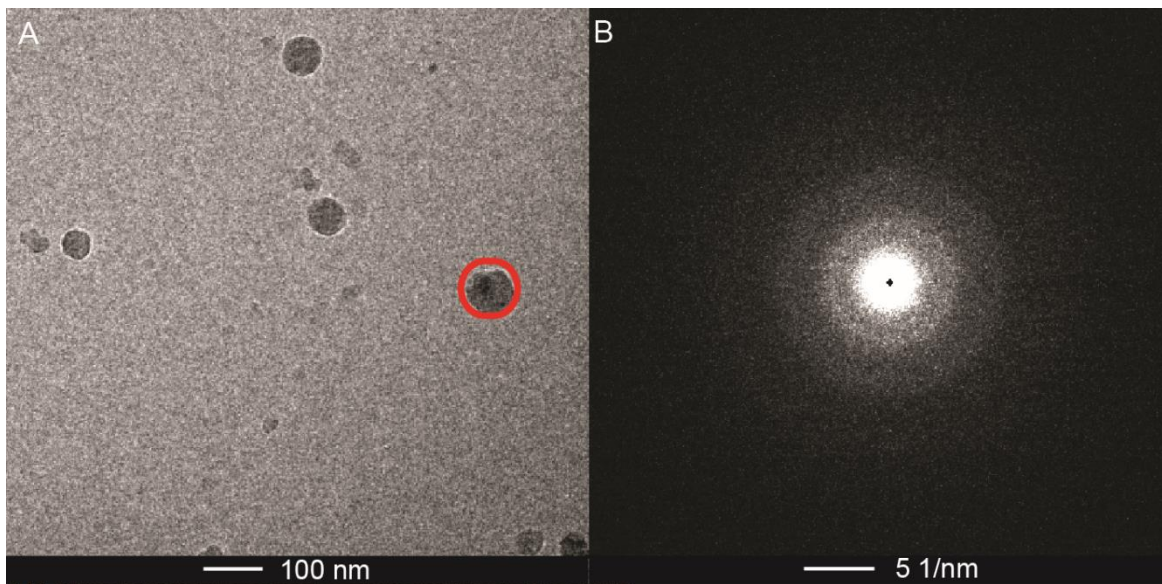


**Fig. A7. Cryo-TEM analysis and NAED.** (A) Cryo-TEM analysis of the suspended objects obtained after 300 minutes and (B) nano area electron diffraction of the area in the red circle (NAED).

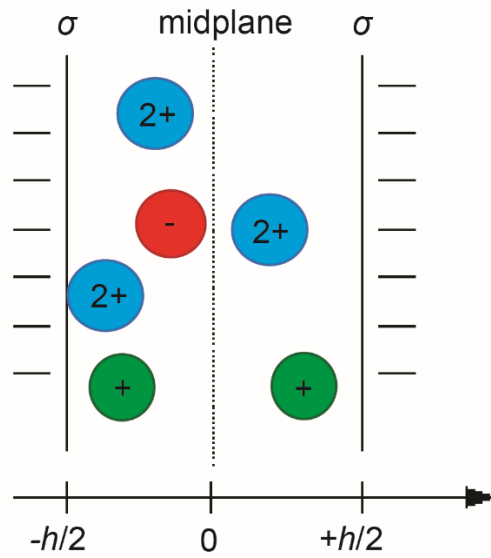


**Fig. A8. Schematic representation of the model used to determine the interactions between the spheroids.** The model consists of two negatively charged surfaces (spheroids) with a uniform surface charge density,  $\sigma$ . The slit is filled with an electrolyte solution containing sodium and calcium counterions as well as hydroxide and nitrate co-ions. The confined solution is in equilibrium with a reservoir of well-defined electrolyte concentrations (chemical potentials).

**TableA 1.** Chemicals.

Name	Chemical formula	PRD-No.	Manufacturer
sodium metasilicate pentahydrate	$\text{Na}_2\text{SiO}_3 \cdot 5\text{H}_2\text{O}$	71746	Sigma Aldrich
calcium chloride dihydrate	$\text{CaCl}_2 \cdot 2\text{H}_2\text{O}$	C3306	Sigma Aldrich
sodium hydroxide	NaOH	S5881	Sigma Aldrich
sodium chloride	NaCl	32038	Sigma Aldrich

**TableA 2.** Concentration of all supersaturated solutions used in this study.

Name	[Ca] (mM)	[Si] (mM)	[Na] (mM)	[Cl] (mM)	[OH] (mM)
Solution 1	15	0.1	200.2	150	80
Solution 2	15	0.05	200.1	150	80
Solution 3	15	0.08	200.16	150	80
Solution 4	15	0.15	200.3	150	80
Solution 5	15	0.2	200.4	150	80
Solution 6	0	0.1	200.2	150	80
Solution 7	15	0.1	235.2	150	115
Solution 8	15	0.1	210.2	150	90
Solution 9	15	0.1	140.2	150	20

**TableA 3.** The particle morphology and the structure factor. (59)

Morphology	$\rho$ -ratio
Homogeneous sphere	0.775
Hollow sphere	1
Ellipsoid	0.775-4
Random polymer coil	1.505



**TableA 4.** The phase assemblage for solution 1.

Phase	<i>S/</i>	log <i>IAP</i>	log <i>KT</i>	Initial	Final	Delta
α-CSH	-3.21	50.29	53.5	0.00	0.00	0.00
β-CSH	0.00	29.35	29.35	0.00	4.37E-05	4.37E-05
γ-CSH	0.38	104.88	104.5	0.00	0.00	0.00
Portlandite	-0.02	23.09	23.11	0.00	0.00	0.00
Silicas	-5.71	-8.41	-2.7	0.00	0.00	0.00

**TableA 5.** The surface composition for solution 1 for the external and internal surface.

<b>External Surface</b>		
Surface charge = 9.840e-003 C/m <sup>2</sup>		
Surface Potential = 8.877e-003 V		
Species	Moles	Fraction
Si <sub>e</sub> _OCa+	1.05E-05	0.48
Si <sub>e</sub> _O-	1.03E-05	0.47
Si <sub>e</sub> _OSi0.5OCa+	5.23E-07	0.024
Si <sub>e</sub> _OSi0.5O-	5.10E-07	0.023
Si <sub>e</sub> _OH	7.40E-09	0.00
Si <sub>e</sub> _OCaOH	7.28E-09	0.00
Si <sub>e</sub> _OSi0.5OH	3.67E-10	0.00
Si <sub>e</sub> _OSi0.5OCaOH	3.61E-10	0.00
<b>Internal surface</b>		
Surface Charge = 0		
Surface Potential = 0		
Species	Moles	Fraction
(Si <sub>i</sub> _O)Ca0.5	2.59E-05	0.4
Si <sub>i</sub> _OH	1.84E-05	0.28
Si <sub>i</sub> _OCaOH	1.81E-05	0.28
Si <sub>i</sub> _OSi0.5OCa0.5	1.29E-06	0.02
Si <sub>i</sub> _OSi0.5OH	9.15E-07	0.014
Si <sub>i</sub> _OSi0.5OCaOH	8.99E-07	0.014

**TableA 6.** Equilibriums in solution or solubility equilibriums.

Solubility Equilibriums	Log <i>K</i>
Portlandite: $\text{Ca(OH)}_2 + 2 \text{H}^+ \rightleftharpoons \text{Ca}^{2+} + 2 \text{H}_2\text{O}$	22.88
Silica: $\text{SiO}_2 + 2 \text{H}_2\text{O} \rightleftharpoons \text{H}_4\text{SiO}_4$	-2.71
$\alpha$ -C-S-H: $\text{Ca}_4\text{Si}_5\text{O}_{16}\text{H}_4, 8 \text{H}_2\text{O} + 8 \text{H}^+ \rightleftharpoons 4 \text{Ca}^{2+} + 5 \text{H}_4\text{SiO}_4 + 4 \text{H}_2\text{O}$	53.5
$\beta$ -C-S-H: $\text{Ca}_2\text{Si}_2\text{O}_7\text{H}_2, 4 \text{H}_2\text{O} + 4 \text{H}^+ \rightleftharpoons 2 \text{Ca}^{2+} + 2 \text{H}_4\text{SiO}_4 + 3 \text{H}_2\text{O}$	29.35
$\gamma$ -C-S-H: $\text{Ca}_6\text{Si}_4\text{O}_{16}\text{H}_4, 8 \text{H}_2\text{O} + 12 \text{H}^+ \rightleftharpoons 6 \text{Ca}^{2+} + 4 \text{H}_4\text{SiO}_4 + 8 \text{H}_2\text{O}$	104.5
Equilibriums in solution	Log <i>K</i>
$\text{H}_2\text{O} \rightleftharpoons \text{OH}^- + \text{H}^+$	-14
$\text{Na}^+ + \text{H}_2\text{O} \rightleftharpoons \text{NaOH} + \text{H}^+$	-14.18
$\text{H}_4\text{SiO}_4 \rightleftharpoons \text{H}_3\text{SiO}_4^- + \text{H}^+$	-9.83
$\text{H}_4\text{SiO}_4 \rightleftharpoons \text{H}_2\text{SiO}_4^{2-} + 2 \text{H}^+$	-23
$\text{Ca}^{2+} + \text{H}_2\text{O} \rightleftharpoons \text{CaOH}^+ + \text{H}^+$	-12.78
$\text{Ca}^{2+} + \text{H}_3\text{SiO}_4^- \rightleftharpoons \text{CaH}_3\text{SiO}_4^+$	0.5
$\text{Ca}^{2+} + \text{H}_2\text{SiO}_4^{2-} \rightleftharpoons \text{CaH}_2\text{SiO}_4$	2.9

**TableA 7.** Chemicals used for the turbidimetric measurements (S5).

Name	Particle size (nm)	CAS Number	Manufacturer
SM-30	7	7631-86-9	Sigma Aldrich
AS-30	12	7631-86-9	Sigma Aldrich
AS-40	20	7631-86-9	Sigma Aldrich

**TableA 8.** Calculations of the possible Ca and Si speciation resulting from different hypotheses.

		Final $\beta$ -CSH product						Spheroid									
		CASE A - Speciation given by the C-S-H model			CASE B - Speciation given by the C-S-H model and refined			CASE 1 - Speciation "as the solution"			CASE 2 - Meet electroneutrality "with CaOH+ as in solution"			CASE 3 - Meet electroneutrality "without CaOH+ as in b-CSH"			
Atom	Charge /atom	CASE A		CASE B		CASE 1		CASE 2		CASE 3		Speciation (%)	Charge	At.-%	Charge	At.-%	Charge
		Speciation (%)	At.-%	Charge	Speciation (%)	At.-%	Charge	Speciation (%)	At.-%	Charge	Speciation (%)						
<b>Cations</b>																	
Ca (100 %)			56.2				39.8				39.8				39.8		
as Ca <sup>2+</sup>	2.00	78%	43.9	87.9	64%	72.3	29.6	59.2	74%	59.2	64%	74%	59.2	29.6	59.2	64%	51.0
as CaOH <sup>+</sup>	1.00	22%	12.3	12.3	36%	20.1	10.2	10.2	26%	10.2	26%	26%	10.2	10.2	10.2	36%	14.3
Na <sup>+</sup>	1.00		2.20	2.20		2.2	19.7	19.7		19.7	19.7		19.7	19.7	19.7		19.7
SUM			58.4	102.4		58.4	94.6	89.1		59.5	89.1		59.5	89.1	59.5		85.0
<b>Anions</b>																	
SiO <sub>2</sub> (100%)			39.7				35.2				35.2				35.2		
as H <sub>3</sub> SiO <sub>4</sub> <sup>-</sup>	-1.00						54%	19.1	-19.1		0.0		0.0	0.0	0.0		0.0
as H <sub>2</sub> SiO <sub>4</sub> <sup>2-</sup>	-2.00						46%	16.1	-32.1		0.0		0.0	0.0	0.0		-20.1
as Si dimers	-2.37	94%	37.2	-88.0	94%	37.2		0.0	0.0	100%	35.2		-83.3	72%	25.2		-59.6
as Si pentamers	-1.89	6.0%	2.50	-4.70	6.0%	2.50		0.0	0.0		0.0		0.0	0.0	0.0		0.0
Cl <sup>-</sup>	-1.00		1.80	-1.80		1.80		5.3	-5.3		5.3		-5.3	5.3			-5.3
SUM			41.5	-94.6		41.5		40.5	-56.6		40.5		-88.6	40.5			-85.0
D (Charges) (+) - (-)			8			0		32			0			0			0

**TableA 9.** Slope  $m$ , the linear correlation coefficient ( $R^2$ ) and the gyration radius ( $R_g$ ) (330 min).

[Si] (mM)	$m$ ( $\mu\text{m}^2 \cdot 10^{-3}$ )	$R^2$	$R_g$ (nm)
0.05	1.59	0.998	$69 \pm 3.0$
0.1	1.67	0.998	$70 \pm 3.0$
0.2	1.74	0.974	$72 \pm 3.0$

**TableA 10.** Slope  $m$ , the linear correlation coefficient ( $R^2$ ) and the gyration radius ( $R_g$ ).

Time (s)	$m$ ( $\mu\text{m}^2 \cdot 10^{-3}$ )	$R^2$	$R_g$ (nm)
5000	1.62	0.994	$70 \pm 3.0$
9000	1.62	0.995	$70 \pm 3.0$
10000	1.68	0.998	$71 \pm 3.0$
15000	1.66	0.997	$71 \pm 3.0$
19000	1.67	0.998	$70 \pm 3.0$

**TableA 11.** Chemicals used for titration experiments.

Name	Chemical formula	PRD-No.	Manufacturer
sodium metasilicate	$\text{Na}_2\text{SiO}_3$	307815-25G	Sigma Aldrich
calcium ion solution	$\text{CaCl}_2$	21059-250ML-F	Sigma Aldrich
sodium hydroxide	$\text{NaOH}$	S5881-500G	Sigma Aldrich
$\alpha$ -lactose	$\text{C}_{12}\text{H}_{22}\text{O}_{11} \cdot \text{H}_2\text{O}$	L3625-5KG	Sigma Aldrich
saccharin	$\text{C}_7\text{H}_5\text{NO}_3\text{S}$	240931-1G	Sigma Aldrich
D-(+)-galactose	$\text{C}_6\text{H}_{12}\text{O}_6$	G0750-5G	Sigma Aldrich
Luviquat FC-550	FC 550	30035096	BASF
Luviquat FC-370	FC 370	30035095	BASF
Luviquat Excellence	L1	30035097	BASF
Luviquat 3	L3	-	BASF

**TableA 12.** Utilized copolymers of poly [(3-methyl-1-vinylimidazoliumchloride)-co-(1-vinylpyrrolidone)]

Name	Composition, % weight		Anion	Solids content (%)	Molecular weight (g/mol)	Charge density (meq/g) at pH 7*
	VP	QVI				
FC 370	70	30	chloride	38-42	100000	2.0
FC 550	50	50	chloride	38-42	80000	3.3
L1	5	95	chloride	38-42	40000	6.1
L3 (with PEG chain)	5	95	chloride	38-42	-	2.6

\*determined with charge density titration

**TableA 13.** Weight of the samples of OPC with 450 and 225 ppm papain.

	blank	OPC + papain* 450 ppm	OPC + papain* 225 ppm
<i>m</i> (cement) (g)	2.001	2.001	2.003
<i>m</i> (water) (g)	0.864	0.864	0.864
<i>m</i> (additive) (mL)	-	0.036	0.018
sodium acetate 50mM (mL)	0.036	-	0.018

**TableA 14.** Weight of the samples of OPC with 1350 and 675 ppm papain.

	blank	OPC + papain* 1350 ppm	OPC + papain* 675 ppm
<i>m</i> (cement) (g)	2.000	2.000	2.000
<i>m</i> (water) (g)	0.788	0.788	0.788
<i>m</i> (additive) (mL)	-	0.112	0.056
sodium acetate 50mM (mL)	0.112	-	0.056

\*Suspension in 50 mM sodium acetate, pH 4.5, containing 0.01% thymol

**TableA 15.** Weight of the samples of OPC with cathepsin B.

	blank	OPC + cathepsin B* <sup>1</sup> 50 ppm	OPC + cathepsin B* <sup>1</sup> 25 ppm
<i>m</i> (cement) (g)	2.002	2.002	2.001
<i>m</i> (water) (g)	0.543	0.543	0.543
<i>m</i> (additive) (mL)	-	0.357	0.178
sodium acetate 50mM, 1mM EDTA (mL)	0.357	-	0.178

\*<sup>1</sup>Suspension in 50 mM sodium acetate buffer, 1 mM EDTA, pH 5.0

**TableA 16.** Weight of the samples of OPC with modified polylysine (6% histidine).

	blank	mod. polylysine 50 ppm	mod. polylysine 25 ppm
<i>m</i> (cement) (g)	2.004	2.002	2.003
<i>m</i> (water) (g)	0.900	0.900	0.900
<i>m</i> (additive) (mg)	-	0.100	0.050

**TableA 17.** Weight of the samples of OPC with 50, 150, and 450 trypsin.

	blank	OPC + trypsin 50 ppm	OPC + trypsin 150 ppm	OPC + trypsin 450 ppm
<i>m</i> (cement) (g)	2.000	2.000	2.000	2.000
<i>m</i> (water) (g)	0.450	0.450	0.450	0.450
<i>m</i> (additive) (mg)	-	0.100	0.300	0.900
sodium acetate 50mM (mL)	0.450	0.450	0.450	0.450

**TableA 18.** Weight of the samples of OPC with 50, 150, and 450 ppm bromelain.

	blank	OPC + bromelain 50 ppm	OPC + bromelain 150 ppm	OPC + bromelain 450 ppm
<i>m</i> (cement) (g)	2.000	2.000	2.000	2.000
<i>m</i> (additive) (mg)	-	0.100	0.300	0.900
sodium acetate 50mM (mL)	0.450	0.900	0.900	0.900

**TableA 19.** Stock solutions for SDS-PAGE.

Buffer	Tris (M)	Tricine (M)	pH	SDS (%)
Anode buffer	0.2		8.9	
Cathode buffer	0.1	0.1	8.25	0.1
Gel buffer	3.0		8.45	0.3
Acrylamide-bisacrylamide mixture	Acrylamide/ % (w/v)	Acrylamide/ % (w/v)	Bisacrylamide/ % (w/v)	Bisacrylamide/ % (w/v)
49.5% T, 3% C	48	48	1.5	1.5
49.5% T, 6% C	46.5	46.5	3.0	3.0

**TableA 20.** Composition of separating, “spacer”, and stacking gels.

	stacking gel 4% T, 3% C	“spacer” gel, 10% T, 3% C	separating gel 10% T, 3% C	separating gel 16.5% T, 5% C
49.5% T, 3% C solution (mL)	1	6.1	6.1	
49.5% T, 6% C solution (mL)				10
Gel buffer (mL)	3.1	10	10	10
Glycerol (g)			4	4
add water to final volume of	12.5 mL	30 mL	30 mL	30 mL

**TableA 21.** Weight of the samples of OPC with inactivated\* papain.

	blank	OPC + inactivated papain 450 ppm	OPC + inactivated papain 675 ppm
<i>m</i> (cement) (g)	2.000	2.000	2.000
<i>m</i> (water) (g)	0.450	0.450	0.450
<i>m</i> (additive) (mg)	-	0.900	1.350
<i>V</i> (sodium acetate) 50mM (mL)	0.450	0.450	0.450

\*The inhibition of papain was done by N-ethylmaleimide.

# References

- [1] E. Worrell, L. Price, N. Martin, L. O. Meida, *Annu. Rev. Energy Environ.* **2001**, *26*, 303–329.
- [2] H. F. W. Taylor, *Cement Chemistry*, Thomas Telford Publishing, London **1997**.
- [3] K. Van Vliet, R. Pellenq, M. J. Buehler, J. C. Grossman, S. Yip, *MRS Bull.* **2012**, *37*, 395 – 402.
- [4] S. Garrault-Gauffinet, A. Nonat, *J. Cryst. Growth* **1999**, *200*, 565-574.
- [5] G. C. Sosso, T. Li, D. Donadio, A. Michaelides, *J. Phys. Chem. Lett.*, **2016** *7(13)*, 2350-2355.
- [6] D. Gebauer, M. Kellermeier, J. D. Gale, L. Berström, H. Cölfen, *Chem. Soc. Rev.* **2014**, *43*, 2348-2371.
- [7] A. E. S. Van Driessche<sup>1</sup>, L. G. Benning, J. D. Rodriguez-Blanco, M. Ossorio, *Science* **2012**, *336*, 69-72.
- [8] D. Damidot, A. Rettel, A. Capmas, *Adv. Cem. Res.* **1996**, *8*, 83.
- [9] P. Gosh, B. Chattopadhyay B., S. Mandal, *Cem. Concr. Com.*, **2009**, *31*, 93-95
- [10] M. Volmer, A. Weber *Z. Phys. Chem.*, 119 (1926) p.277–301
- [11] L. Farkas, *Z. Phys. Chem.* **1927**, *125*, 236.
- [12] R. Becker, W. Döring, *Ann. Phys.* **1935**, *416*, 719–752.
- [13] J.B. Zeldovich, *Acta Physicochim.* **1943**, *18*, 1–22.
- [14] J. W. Gibbs, J. W. *The Collected Works of J. Willard Gibbs*; Longmans, Green and Co.: New York, **1928**.
- [15] E. Sanz, C. Vega, J. R. Espinosa, J. Abascal, C. Valeriani, *J. Am. Chem. Soc.* **2013**, *135*, 15008–15017.
- [16] P.G. Vekilov, *Nanoscale* 2010, *2*, 2346.
- [17] J. De Yoreo, *Nat. Mater.* **2013**, *12*, 284–285.
- [18] W. Pan, A.B. Kolomeisky, P.G. Vekilov, *J. Chem. Phys.* **2005**, *122*, 174905.
- [19] Q. Hu, M. H. Nielsen, C. L. Freeman, J. Tao, J. J. De Yoreo, *Faraday Discuss.* **2012**, *159*, 509–523.
- [20] V.I. Kalikmanov, *J. Chem. Phys.* 2006, *124*, 124505.
- [21] P. N. Pusey, W. van Meegen, *Nature* **1986**, *320*, 340–342.
- [22] U. Gasser, E. R. Weeks, A. Schofield, P. N. Pusey, D. A. Weitz, *Science* **2001**, *292*, 258–262.
- [23] A. D. Dinsmore, E. R. Weeks, V. Prasad, A. C. Levitt, D. Weitz, *Appl. Opt.* **2001**, *40*, 4152.
- [24] M. Sleutel, J. Lutsko, A. E. S. Van Driessche, D. Maes, *Nat. Commun.* **2014**, *5*, 5598.
- [25] E. M. Pouget, P. M. Frederik, G. de With, N. A. J. M. Sommerdijk, *Science* **2009**, *323*, 1455-1458.
- [26] J. Baumgartner, A. Dey, C., P. Fratzl, N. A. J. M. Sommerdijk, D. Faivre, *Nat. Mater.* **2013**, *12*, 310–314.
- [27] J. A. Sellberg, C. Huang, D. Schlesinger, R. G. Sierra, D. Nordlund, *Nature* **2014**, *510*, 381-384.
- [28] P. N. Pusey, W. van Meegen, P. Bartlett, J. Rarity, S. M. Underwood, *Phys. Rev. Lett.* **1989**, *63*, 2753-2756.
- [29] J. Zhu, M. Li, W. Meyer, R. H. Ottewill, W. B. Russel, P. M. Chaikin, *Nature* **1997**, *387*, 883–885.
- [30] M. Ildefonso, P. Punniyam, J. Salmon, N. Candoni, S. Veessler, *J. Cryst. Growth* **2012**, *342*, 9–12.



- [31] S. S. Kadam, S. A. Kulkarni, A. Stankiewicz, J. H. Horst, H. J. Kramer, *Chem. Eng. Sci.* **2012**, *72*, 10-19.
- [32] B. Peters, *J. Cryst. Growth* **2011**, *317*, 79–83.
- [33] G. Bogoeva-Gaceva, A. Janevski, E. Mader, *Polymer* **2001**, *42*, 4409–4416.
- [34] S. R. Davies, K. C. Hester, J. W. Lachance, C. A. Koh, *Chem. Eng. Sci.* **2009**, *64*, 370–375.
- [35] E. Ochshorn, W. Cantrell, *J. Chem. Phys.* **2006**, *124*, 054714.
- [36] A. Manka, H. Pathak, S. Tanimura, B. E. Wyslouzil, *Phys. Chem. Chem. Phys.* **2012**, *14*, 4505–4516.
- [37] H. C. Schröder, X. Wang, W. Tremel, H. Ushijima, W.E.G. Müller, *Nat. Prod. Rep.* **2008**, *25*, 455.
- [38] K. Shimizu, J. Cha, G. D. Stucky, D. E. Morse, *Proc. Natl. Acad. Sci. USA* **1998**, *95*, 6234.
- [39] R. L. Brutchey, D. E. Morse, *Chem Rev.* **2008**, *108*, 4915.
- [40] R. Wetherbee, *Science* **2002**, *298*, 547.
- [41] D. Kisailus, J. H. Choi, J. C. Weaver, W. Yang, D. E. Morse, *Adv Mater* **2005**, *17*, 314.
- [42] D. J. Belton, E. N. Danilovtseva, C. C. Perry, *Proc. Natl. Acad. Sci. USA* **2008**, *105*, 5963.
- [43] K. Spinde, M. Kammer, K. Freyer, H. Ehrlich, J. N. Vournakis, E. Brunner, *Chem. Mater* **2011**, *23*, 2973.
- [44] W. E. G. Müller, W. Tremel, V. Gamulin, C. Perry, A. Boreiko, H. C. Schröder, *Micron* **2006**, *37*, 107-120.
- [45] W. E. G. Müller, A. Boreiko, W. Tremel, A. Reiber, H. C. Schröder *Cell Tissue Res.* **2005**, *321*, 285-297.
- [46] J. Cha, Y. Zhou, S. C. Christiansen, G. D. Stucky, D. E. Morse, *Proc. Natl. Acad. Sci.* **1999**, *96*, 361-365.
- [47] I. G. Richardson, *Cem. Concr. Res.* **2004**, *34*, 1733-1777.
- [48] <https://www.mineralienatlas.de/lexikon/index.php/MineralData?mineral=Tobermorit>, 18.06.2017.
- [49] R. Bonaccorsi, P. Palla, J. Tomasi. *J. Am. Chem. Soc.* , **1984**, *106* (7), pp 1945–1950.
- [50] A. Nonat, *Cem. Concr. Res.* **2004**, *34*, 1521-1528.
- [51] P. Hewlett, *Lea's Chemistry of Cement and Concrete*. 4 th Edition. Arnold. London. **1998** *5*, 865-873.
- [52] M. R. Jones, L. Zheng, M. D. Newland, *Proceedings of the CIM 1992 Annual Conference*.
- [53] W. Muynck, *Constr. Build. Mater.* **2008**, *22* 875-885.
- [54] V. Achal, X. Pan, *Chemosphere* **2012** *8*, 764-768.
- [55] G. Le Metayer-Levrel, S. Castanier, G. Oral, *Sediment. Geol.* **1990** *126*, 25-34.
- [56] S. R. Laxmana Reddy, A. Manjusha, M. Arun kumar, *Int. J. Curr. Eng. Tech.* **2015** *5* P-ISSN 2347-5161.
- [57] H. Galster, *pH measurems: fundamntal, applications, instrumentation*. Weinheim: VCH, **1991** 23-29.
- [58] E. W. Rice, *Anal. Chim. Acta*, **1976** 871-258.
- [59] W. Schaertl, *LS from Polymer Solutions and Nanoparticle Dispersions*, Springer, Heidelberg **2007**.
- [60] J. Rieger, M. Kellermeier, L. Nicoleau, *Angew. Chem.* **2014**, *53*, 12380-12396.
- [61] K. Thanh, N. Maclean, S. Mahiddine, *Chem. Rev.* **2014**, *114*, 7610–7630.

- [62] M. Sleutel, A. E. S. Van Driessche, *Proc. Natl Acad. Sci. USA* **2014**, *111*, E546- E553.
- [63] J. J. De Yoreo, *Nat. Mater.* **2013**, *12*, 284–285.
- [64] W. Sun, S. Booth, A. Myerson, C. Hughes, H. Pan, G. Coquerel, C. Brandel, H. Meekes, M. Mazzotti, L. Fabian, S. Black, P. Vekilov, K. Back, D. Toroz, J. Lovelock, J. Sefcik, A. Rasmuson, E. Breynaert, R. Sear, R. Hammond, M. Ward, T. Threlfall, J. De Yoreo, R. Davey, R. Ristic, K. Lewtas, K. Roberts, A. Hare, M. Gich, H. Cölfen, M. Likhatskiy, N. Sommerdijk, *Farad. Discuss.* **2015**, *179*, 247-267.
- [65] S. T. Sun, P. Zhang, D. Gebauer, H. Cölfen, *Angew. Chem., Int. Ed* **2016**, *55*, 12206-12209.
- [66] A. Rao, P. Vásquez-Quitral, M. S. Fernández, J. K. Berg, M. Sánchez, M. Drechsler, A. Neira-Carrillo, J. L. Arias, D. Gebauer, H. Cölfen, *Cryst. Growth Des.* **2016**, *16*, 1349-1359.
- [67] M. Faatz, F. Grohn, G. Wegner, *Adv. Mater* **2014**, *16*, 153-159.
- [68] A. F. Wallace, L.O. Hedges, A. Fernandez-Martinez, P. Raiteri, J.D. Gale, G.A. Waychunas, S. Whitlam, J.F. Banfield, J. J. De Yoreo, *Science* **2013**, *341*, 885-889.
- [69] A. E. S. Van Driessche<sup>1</sup>, L. G. Benning, J. D. Rodriguez-Blanco, M. Ossorio, P. Bots, J. M. García-Ruiz, *Science* **2012**, *336*, 69-72.
- [70] M. J. Abdolhosseini Qomi, K. J. Krakowiak, M. Bauchy, K. L. Stewart, R. Shahsavari, D. Jagannathan, D.B. Brommer, A. Baronnet, M. J. Buehler, S. Yip, F.-J. Ulm, K. J. Van Vliet, R. J.-M. Pellenq, *Nat. Commun.* **2014**, *5*, 4960/1-10.
- [71] D. Damidot, A. Rettel, A. Capmas, *Adv. Cem. Res.* **1996**, *8*, 83.
- [72] G. Renaudin, J. Russias, F. Frizon, C. Cau-dit-Coumes, *J. Solid State Chem.* **2009**, *182*, 3312-3319.
- [73] L. Nicoleau, A. Nonat, *Cem. Conc. Res.* **2016**, *86*, 1-11.
- [74] K. Ioannidou, M. Kanduč, L. Li, D. Frenkel, J. Dobnikar, E. Del Gado, *Nat. Comm.* **2016**, *7*, 12106/1-9.
- [75] E. Masoero, E. Del Gado, R. J. -M. Pellenq, F. -J. Ulm, S. Yip, *Phys. Rev. Lett.* **2012**, *109*, 155503/1-4.
- [76] N. Roussel, G. Ovarlez, S. Garrault, C. Brumaud, *Cem. Concr. Res.* **2012**, *42*, 148-157.
- [77] C. Labbez, B. Jönsson, A. Nonat, M. Delhorme, *Phys. Chem. Chem. Phys.* **2014**, *16*, 23800-23808.
- [78] Q. Hua, T. Kima, M. Tyler Leya, J. Bullardc, R. Winarskid, *Cem. Concr. Res.* **2016**, *88*, 157-169.
- [79] F. Begarin, S. Garrault, A. Nonat, L. Nicoleau, *Adv. Appl. Cer.* **2011**, *110*, 127-130.
- [80] D. Marchon, U. Sulser, A. Eberhardt, R. J. Flatt, *Soft Matter* **2013**, *9*, 10719-10728.
- [81] L. Nicoleau, T. Gädt, L. Chitu, G. Maier, O. Paris, *Soft Matter* **2013**, *9*, 4864-74.
- [82] T. Rodriguez, *Adv. Appl. Cer.* **2015**, *114*, 362-371.
- [83] B. Lothenbach, A. Nonat, *Cem. Concr. Res.* **2015**, *8*, 57–70.
- [84] L. Nachbaur, P.-C. Nkinamubanzi, A. Nonat, J.-C. Mutin, *Cem. Concr. Res.* **1998**, *202*, 261-268.
- [85] J. Haas, A. Nonat, *Cem. Concr. Res.* **2015**, *68*, 124-138.
- [86] C. Labbez, B. Jönsson, I. Pochard, A. Nonat, B. Cabane, *J. Phys. Chem. B* **2006**, *110*, 9219–9230.

- [87] F. Gaboriaud, A. Nonat, D. Chaumont, A. Craievich, B. Hanquet, *J. Phys. Chem.* **1999**, *103*, 2091–2099.
- [88] P.D. Maniar, A. Navrotsky, J.Y. Ying, J.B. Benziger, *J. Non-Cryst. Sol.* **1990**, *124*, 101-111.
- [89] S. Yang, In Situ Calorimetric, *J. Phys. Chem. B.* **2000**, *104*, 6071-6080.
- [90] D. Kashchiev, *Nucleation: basic theory with applications*, Butterworth-Heinemann, **2000**.
- [91] A. Navrotsky, *Proc. Natl. Acad. Sci U.S.A.* **2004**, *101*, 12096-12101.
- [92] M. Delhorme, C. Labbez, M. Turesson, C. E. Woodward, B. Jönsson, *Langmuir* **2016**, *32*, 2058-2066.
- [93] A. Baronov, K. Bufkin, B. L. Johnson, D. L. Patrick, *Phys.Chem.Chem.Phys.* **2015**, *17*, 20846-20852.
- [94] P. Juilland, A. Kumar, E. Gallucci, R. J. Flatt, K. L. Scrivener, *Cem. Concr. Res.* **2002**, *42*, 1175-1188.
- [95] L. Valentini, M. Favero, M. C. Dalconi, G. Ferrari, G. Artioli, *Cryst. Growth Des.* **2016**, *16*, 2404-2415.
- [96] C. E. White, L. L. Daemen, M. Hartl, K. Page, *Cem. Concr. Res.* **2015**, *67*, 66-73.
- [97] K. Naka, *Langmuir* **2006**, *22*, 7760.
- [98] T. Wang, M. Antonietti, *Chem.-Eur.* **2006** 125722.
- [99] D. Gebauer, A. Verch, H. G. Börner, H. Cölfen. *Cry. Growth Design.* **2009** *9*, 2398–2403.
- [100] Picker, A. Dissertation: University Konstanz. **2012**
- [101] E. Kharlampieva, C. M. Jung, V. Kozlovskava, *J. Mater. Chem.* **2010** *20*, 5242-5250.
- [102] P. Bazant, P. Acker, I. Carol, J. M. R. Catarino, J. C. Chern, M. A. Chiorino, B. Espion, C. Huet, T. Kanstad, V. Kristek, H. S. Muller, B. H. Oh, J. Ozbolt, S. Reid, P. Schwesinger, B. Teply, H. Trost, T. Tsubaki, F. H. Wittmann, Y. P. Xi, *Mater. Struc.* **2005**, *78*, 52-55.
- [103] M. Buroker, *Analyt. Biochem.* **1993** *208*, 5.
- [104] V. O. Özçelik, C. E. White, *J. Phys. Chem. Lett.* **2016**, *7*, 5266–5272.
- [105] R. B. Bergmann, A. Bill, *J. Cryst. Growth* **2008**, *310*, 3135–3138.
- [106] J. Ilavsky, P. R. Jemian, *J. Appl. Crystallogr.* **2009**, *42*, 347–353.
- [107] J. P. Valleau, R. Ivkov, G. M. Torrie, *J. Chem. Phys.* **1991**, *95*, 520-532.
- [108] N. A. Metropolis, A. W. Rosenbluth, A. Teller, E. J. Teller, *Chem. Phys.* **1953**, *21*, 1087-1092.
- [109] B. R. Svensson, C. E. Woodward, *C. E. Mol. Phys.* **1988**, *64*, 247-259.

# List of Figures

<b>Figure 1.</b> Typical SEM micrograph of the alite phase in ordinary Portland cement with calcium silicate hydrate needles after x hours of hydration.....	17
<b>Figure 2:</b> Schematic comparison of one-step versus two-step nucleation for a generic supersaturated solution.....	23
<b>Figure 3:</b> Heterogeneous formation of a hemispherical nucleus at a foreign substrate with the three different interfacial free energies $\gamma_{scr}$ , $\gamma_{lc}$ and $\gamma_{ls}$ .....	26
<b>Figure 4:</b> Several levels of hierarchy in the structure of the skeleton of the glass sponge Euplectella. (A) photograph of entire skeleton, scale bar: 1 cm; (B) Fragment of the cage structure showing the square-grid lattice, scale bar: 5 mm; (C) fractured and partially HF-etched single beam revealing its ceramic fibre-composite structure, scale bar: 20 $\mu\text{m}$ ; (D) cross section through a typical spicule in a strut, showing its characteristic laminated architecture, scale bar: 5 $\mu\text{m}$ ; (E) fractured spicule, revealing an organic interlayer, scale bar: 1 $\mu\text{m}$ ; (F) bleaching of biosilica surface revealing its consolidated nanoparticulate nature, Scale bar: 500 nm. (Science 2005, 8, 5732.).....	28
<b>Figure 5.</b> Isothermal calorimetry of OPC, heat flow versus time with focus on silicate reaction.....	33
<b>Figure 6.</b> Isothermal calorimetry of OPC, heat flow versus time with a focus on aluminate reaction. ..	33
<b>Figure 7.</b> 3D crystal structure showing dreierketten chains present in 1.1 nm tobermorite projected (Ca= green, O= red, Si= brown, H= pink). (48).....	36
<b>Figure 8.</b> Schematic crystal structure of tobermorite-14 Å, as seen perpendicular to [010] according to Merlino and Bonaccorsi. (49) The layers of Ca polyhedral are drawn in green, whereas the silicate chains are in blue. Green circles in the complex layers represent the calcium ions and the red circles the water molecules. ....	36
<b>Figure 9.</b> High-resolution transmission electron micrograph of 1.4 nm tobermorite from Crestmore, California, and the resulting profile plots. (3).....	37
<b>Figure 10.</b> The 3D crystal structure of monoclinic jennite. ....	37
<b>Figure 11:</b> Setup for potentiometric measurements with $U_1$ : Galvani potential of the indicator electrode relative to the sample solution, $U_2$ : Galvani potential of the reference electrolyte relative to the glass membrane, $U_3$ : Galvani potential of the internal reference electrode relative to the reference electrolyte, $U_4$ : Galvani potential of the reference electrode and $U_5$ : Diffusion potential at the diaphragm. ....	42
<b>Figure 12.</b> Construction of ion-sensitive electrodes. ....	43
<b>Figure 13.</b> Schematic illustration of 90° and forward light scattering measurement.....	44
<b>Figure 14.</b> Schematic illustration of the light scattering properties of different particle sizes. ....	45
<b>Figure 15.</b> The turbidity of colloidal silica solutions over concentration. ....	46
<b>Figure 16. Characterization of the final reaction product.</b> (A) TEM micrograph of the collected solid phase. (B, C) NAED pattern of the final product. (D) STEM EDX spectrum and (E) area from which the EDX pattern was recorded. ....	51

**Figure 17. Evolution of the turbidity and solution concentrations.** (A, B, C) show results related to the reference experiment containing 100  $\mu\text{mol/L}$  of Si and 80  $\text{mmol/L}$  of NaOH: (A) Time evolution of the turbidity (black) and the activity of hydroxide (blue). (B) the [Si] and [Ca] concentrations (mean values averaged over three experiments) analyzed by ICP-OES. (C) Evolution of the supersaturation ( $\beta$ ) with respect to C-S-H and  $\text{Ca(OH)}_2$  solubilities calculated from the solution concentrations. Evolution of the turbidity for various conditions: at different silicate concentrations (D), different pH values (E) and different stirring speeds (F) as a function of time. The standard deviation of the turbidity potential is below 5 mV. .... 52

**Figure 18. Light and synchrotron X-ray scattering analysis of the supersaturated reference solution.** (A) Hydrodynamic radius determined by DLS at three different angles during the first 5 to 100 minutes. (B) Evolution of the gyration radius calculated from the Guinier plot ( $\ln I_q$  over  $q^2$ ) obtained by SLS during stages I and II (400 minutes). (C) Time resolved *in situ* SAXS pattern during the first 15 min. The formation of small primary entities/scatterers is shown through the increase in intensity with the fits of scattering curves (red). (D) Radius evolution resulting from the fits of scattering curves (size distribution represented by the error bars). .... 54

**Figure 19. C-S-H crystallization from the reference supersaturated solution observed by Cryo-TEM, NAED and STEM EDX.** (A) Cryo-TEM image of the suspended particles 300 min after addition of the silicate solution. (B) NAED pattern of the spheroid after 300 min (C) STEM EDX spectrum of the spheroid after 300 min. (D) Cryo-TEM image of the suspension and (E) high resolution image after 600 min. (F) Profile plot along the back dotted line shown in high resolution image (E) of the particles formed after 600 min in solution. .... 56

**Figure 20. Modeling results.** (A) Simulations of the average number of  $\text{Ca}^{2+}$ ,  $\text{Na}^+$  and anions ( $\text{OH}^-$  and  $\text{Cl}^-$ ) per silicate dimer ( $\text{Si}_2\text{O}_7^{6-}$ ) as a function of the volume of the cubic simulation box. The simulations are performed in the semi-grand canonical ensemble with one silicate dimer per box. The volume of the box is therefore proportional to the density in silicate dimers in the spheroids. The ions excepted the silicate dimer are allowed to move in and out of the simulation box according to their set chemical potential, i.e. they are in equilibrium with the bulk solution. A  $\text{Ca}^{2+}/\text{Na}^+$  ratio of 2 corresponds to a volume of  $16^3 \text{ \AA}^3$ . In C-S-H, this volume corresponds to  $6^3 \text{ \AA}^3$ , and the surface charge density is  $-4 \text{ e/nm}^2$ . Thus, the spheroids are, the spheroids are approximately  $(16/6)^3 = 19$  times less dense than C-S-H and their surface is  $(16/6)^2 = 7$  times less charged. (B) Interaction surface free energy ( $W(r)$ ) curves as a function of the distance between two negatively charged infinite plates (see Fig. A8), for different charge densities. A charge of  $-0.6 \text{ e/nm}^2$  corresponds to the surface charge density of the spheroids as calculated in (A). A charge of  $-4 \text{ e/nm}^2$  matches the surface charge density of C-S-H. The interaction is purely repulsive at low charge density and becomes attractive at  $-1 \text{ e/nm}^2$ . .... 58

**Figure 21. Two-step pathway theory versus classical nucleation theory (CNT).** (A) Evolution of the turbidity (red curve) with the different species emerging along the reaction the path: (a) Supersaturated solution, (b) liquid amorphous intermediate, (c) crystalline domains and (d) final  $\beta$ -C-S-H platelets. (e) Model of C-S-H structure represented by  $14 \text{ \AA}$  tobermorite. Reprinted with permission from ref. 104. Copyright 2017 American Chemical Society. The first chemical step,

defined by the first  $U_{turb}$  drop in stage I, is the formation of liquid amorphous intermediates rich in silicate dimers and calcium. The intermediate has a composition in silicate and calcium similar to that of  $\beta$ -C-S-H with additional sodium ions and water molecules. The second step encompasses a Ca/Na exchange (stage II to stage III) resulting in the formation of  $\beta$ -C-S-H crystallites which aggregate and give rise to the second  $U_{turb}$  drop. **(B)** Tentative free energy profiles showcasing the two-step mechanism observed in this study (red line) compared to classical nucleation (black line). **(C)** Typical plot in the framework of the CNT used for the calculation of the energy penalty (interfacial energy) to form a solid phase from supersaturated solution. .... 61

**Figure 22.** Titration curve. .... 65

**Figure 23.** Titration curves at pH 13.6 ( $[\text{Na}_2\text{SiO}_3] = 6.6 \text{ mM}$ ,  $[\text{CaCl}_2] = 30 \text{ mM}$ ) with a stirring speed of 8 (black) and 15 (red). .... 66

**Figure 24.** Titration curves at pH 13.6 ( $[\text{Na}_2\text{SiO}_3] = 6.6 \text{ mM}$ ,  $[\text{CaCl}_2] = 30 \text{ mM}$ ) with a dosing speed for  $\text{CaCl}_2$  of 0.04 mL/min (red), 0.02 mL/min (green) and 0.01 mL/min (black). .... 67

**Figure 25.** Titration curves at pH 13.6 ( $[\text{Na}_2\text{SiO}_3] = 6.6 \text{ mM}$ ,  $[\text{CaCl}_2] = 30 \text{ mM}$ ) with a dosing speed of 0.04 mL/min (green), 0.02 mL/min (red) and 0.01 mL/min (black) over the dosed amount of calcium. .... 67

**Figure 26.** Structural chemical formula of  $\alpha$ -lactose, D-(+)-galactose and saccharin. .... 68

**Figure 27.** Titration curves at pH 13.6 ( $[\text{Na}_2\text{SiO}_3] = 6.6 \text{ mM}$ ,  $[\text{CaCl}_2] = 30 \text{ mM}$ ) with addition of 10 mg lactose (green) and 15 mg lactose (purple). .... 69

**Figure 28.** Titration curves at pH 13.6 ( $[\text{Na}_2\text{SiO}_3] = 6.6 \text{ mM}$ ,  $[\text{CaCl}_2] = 30 \text{ mM}$ ) with addition of 10 mg galactose (turquoise) and 15 mg galactose (purple). The blue graph shows the dosed amount of calcium by titration. .... 69

**Figure 29.** Structural chemical formula of copolymers of vinylpyrrolidone (VP) and quaternized vinylimidazole (QVI). .... 71

**Figure 30.** Titration curves at pH 13.6 ( $[\text{Na}_2\text{SiO}_3] = 6.6 \text{ mM}$ ,  $[\text{CaCl}_2] = 30 \text{ mM}$ ) with the addition of FC 370. Comparison of the effect of 2.5 mg (red), 5 mg (green) and 15 mg FC 370 (blue). .... 71

**Figure 31.** Titration curves at pH 13.6 ( $[\text{Na}_2\text{SiO}_3] = 6.6 \text{ mM}$ ,  $[\text{CaCl}_2] = 30 \text{ mM}$ ) with addition of FC 550. Comparison of the effect of 2.5 mg (green), 20 mg (dark blue) and 40 mg FC 550 (light blue). . 72

**Figure 32.** Titration curves at pH 13.6 ( $[\text{Na}_2\text{SiO}_3] = 6.6 \text{ mM}$ ,  $[\text{CaCl}_2] = 30 \text{ mM}$ ) with addition of L1. The blue graph shows the dosed amount of calcium by titration. Comparison of the effect of 3 mg (green), 10 mg (red) and 20 mg L1 (blue). .... 73

**Figure 33.** Titration curves at pH 13.6 ( $[\text{Na}_2\text{SiO}_3] = 6.6 \text{ mM}$ ,  $[\text{CaCl}_2] = 30 \text{ mM}$ ) with addition of L3 12.5 mg (green) and 15 mg (blue) with reference (black). .... 74

**Figure 34.** Heat flow curves of the hydration of OPC with 225 (red) and 450 ppm (green) papain and reference (black) over 1500 minutes. .... 78

**Figure 35.** Heat flow curves of the hydration of OPC with 625 (blue) and 1350 ppm (green) papain and reference (black) over 1500 minutes. .... 78

**Figure 36.** Heat flow curves of the hydration of OPC with 25 (green) and 50 ppm (red) modified polylysine (6% histidine) with reference (black) over 1500 minutes. .... 79

<b>Figure 37.</b> Heat flow curves of the hydration of OPC with 25 (green) and 50 ppm (red) cathepsin B with reference (black) over 1500 minutes. ....	80
<b>Figure 38.</b> Heat flow curves of the hydration of OPC with 50 (red), 150 (green), and 450 (blue) ppm trypsin with reference (black) over 1500 minutes. ....	81
<b>Figure 39.</b> Heat flow curves of the hydration of OPC with 50 (red), 150 (green) and 450 ppm (blue) bromelain with reference (black) over 1500 minutes. ....	82
<b>Figure 40.</b> Absorbance spectra of coomassie blue from 400 to 700 nm at 5 (black), 3.75 (red), 2.5 (green) and 1.25 mg/mL (blue) of the substrate Casein with reference (light blue). ....	85
<b>Figure 41.</b> Absorbance at 595 nm versus different concentrations of Casein at 595 nm. ....	85
<b>Figure 42. (A).</b> The absorbance difference versus different concentrations of activated papain. <b>(B).</b> The absorbance difference versus different concentrations of inactivated papain at 595 nm. ....	86
<b>Figure 43.</b> Absorbance difference at 595 nm versus time with 0.7 mg/mL of papain after incubation in a basic solution of pH 12. ....	87
<b>Figure 44.</b> Absorbance difference of coomassie assay with basic substrate solution versus different concentrations of papain at 595 nm. ....	88
<b>Figure 45.</b> SDS-PAGE photograph of the Casein substrate solution. The photograph was taken by a Kodak <i>Gel-Dokumentation</i> instrument (EDAS 290) after destaining the gel in a standard fixing solution. ....	88
<b>Figure 46.</b> SDS-PAGE photograph of the papain protease solution. The photograph was taken by a Kodak <i>Gel-Dokumentation</i> instrument (EDAS 290) after destaining the gel in a standard fixing solution. K is the control without papain, C1 contains 0.1mg/mL, C2 contains 0.2 mg/mL, and C3 contains 7 mg/mL. ....	89
<b>Figure 47</b> SDS-PAGE photograph of the papain protease solution after the coomassie assay. The photograph was taken by a Kodak Gel-Dokumentation instrument (EDAS 290) after destaining the gel in a standard fixing solution. K is the control without papain, C1 contains 0.1 mg/mL, C2 contains 0.2 mg/mL, and C3 contains 0.7 mg/mL. ....	90
<b>Figure 48.</b> Heat flow curves of the hydration of OPC with 450 (blue) and 675 ppm (green) inhibited papain with reference (red) over 1500 minutes. ....	91

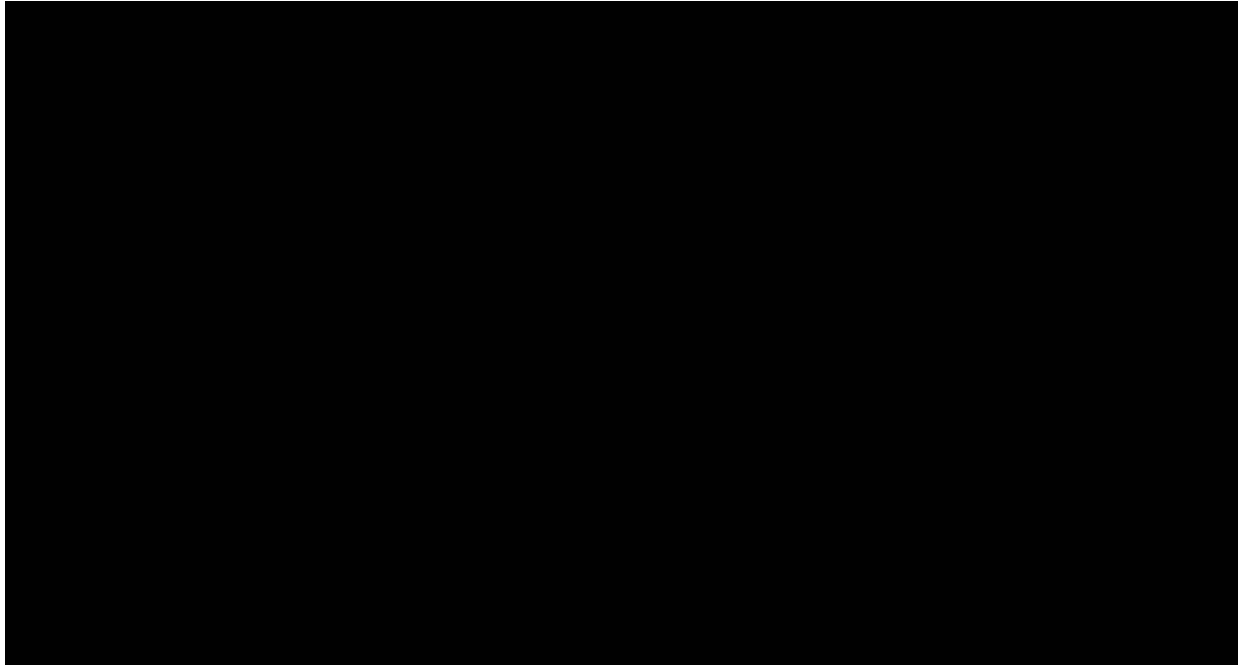
# List of Tables

<b>Table 1:</b> Comparison of the effect of lactose and galactose on the nucleation of C-S-H. ....	69
<b>Table 2:</b> Comparison of the effect of FC 370 on the nucleation of C-S-H. ....	70
<b>Table 3:</b> Comparison of the effect of FC 550 on the nucleation of C-S-H. ....	72
<b>Table 4:</b> Comparison of the effect of L1 on the nucleation of C-S-H. ....	73
<b>Table 5:</b> Comparison of the effect of FC 370, FC 550, and L1 on the nucleation of C-S-H. ....	73
<b>Table 6:</b> Comparison of the effect of L3 on the nucleation of C-S-H. ....	74
<b>Table 7:</b> Comparison of the effect of L1 and L3 on the nucleation of C-S-H. ....	74
<b>Table 8:</b> Degree of acceleration of the hydration of OPC caused by 225 and 450 ppm papain. ....	78
<b>Table 9:</b> Degree of acceleration of the hydration of OPC caused by 625 and 1350 ppm papain. ....	79
<b>Table 10:</b> Acceleration of the hydration of OPC caused by cathepsin B at different concentrations. ..	80
<b>Table 11:</b> Degree of acceleration of the hydration of OPC caused by 50, 150, and 450 ppm trypsin. .	81
<b>Table 12:</b> Degree of acceleration of the hydration of OPC caused by bromelain. ....	82
<b>Table 13:</b> Acceleration of the hydration of OPC caused by inhibited papain. ....	91
<b>TableA 1.</b> Chemicals. ....	112
<b>TableA 2.</b> Concentration of all supersaturated solutions used in this study. ....	112
<b>TableA 3.</b> The particle morphology and the structure factor. (59).....	113
<b>TableA 4.</b> The phase assemblage for solution 1.....	114
<b>TableA 5.</b> The surface composition for solution 1 for the external and internal surface. ....	114
<b>TableA 6.</b> Equilibriums in solution or solubility equilibriums. ....	115
<b>TableA 7.</b> Chemicals used for the turbidimetric measurements (S5). ....	115
<b>TableA 8.</b> Calculations of the possible Ca and Si speciation resulting from different hypotheses. ....	116
<b>TableA 9.</b> Slope $m$ , the linear correlation coefficient ( $R^2$ ) and the gyration radius ( $R_g$ ) (330 min). ....	117
<b>TableA 10.</b> Slope $m$ , the linear correlation coefficient ( $R^2$ ) and the gyration radius ( $R_g$ ). ....	117
<b>TableA 11.</b> Chemicals used for titration experiments. ....	117
<b>TableA 12.</b> Utilized copolymers of poly [(3-methyl-1-vinylimidazoliumchloride)-co- ....	117
<b>TableA 13.</b> Weight of the samples of OPC with 450 and 225 ppm papain. ....	118
<b>TableA 14.</b> Weight of the samples of OPC with 1350 and 675 ppm papain. ....	118
<b>TableA 15.</b> Weight of the samples of OPC with cathepsin B. ....	118
<b>TableA 16.</b> Weight of the samples of OPC with modified polylysine (6% histidine). ....	119
<b>TableA 17.</b> Weight of the samples of OPC with 50, 150, and 450 trypsin. ....	119
<b>TableA 18.</b> Weight of the samples of OPC with 50, 150, and 450 ppm bromelain. ....	119
<b>TableA 19.</b> Stock solutions for SDS-PAGE. ....	119
<b>TableA 20.</b> Composition of separating, “spacer”, and stacking gels. ....	120
<b>TableA 21.</b> Weight of the samples of OPC with inactivated* papain. ....	120



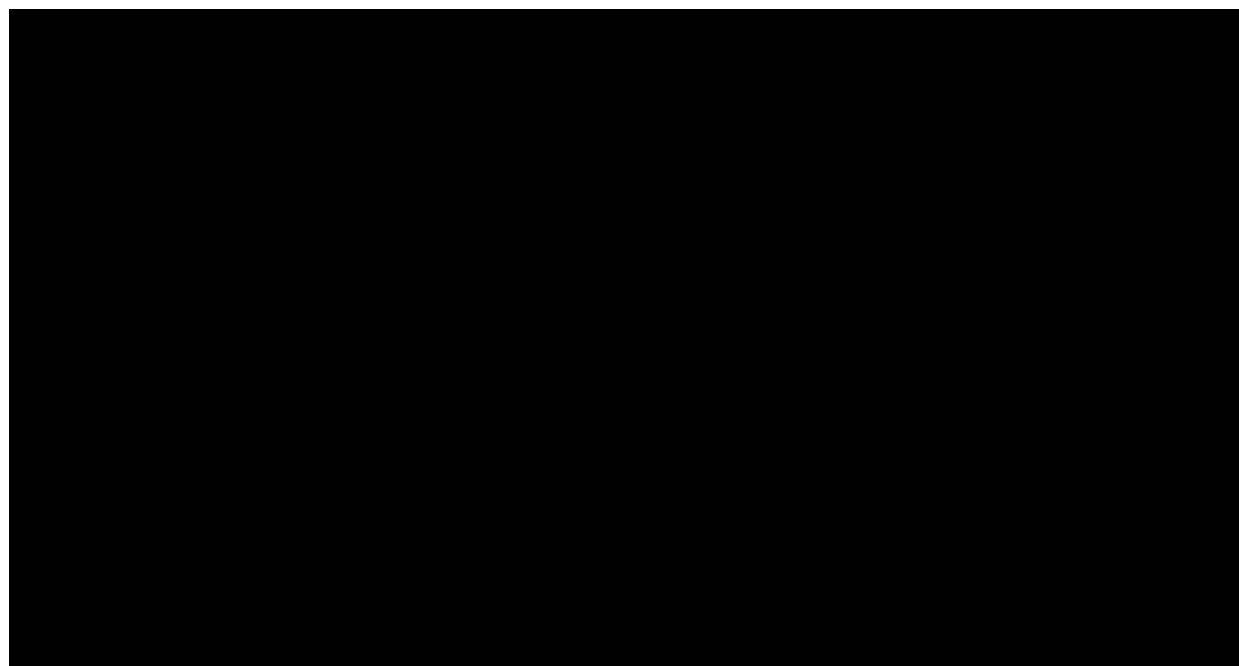
# Curriculum Vitae

## Promotion



- Betreuung der Abschlussarbeit von Bachelorkandidaten und Modulanten
- Betreuung des Grundpraktikums Chemie für Mediziner (Tutorium und Klausurbetreuung für 140 Studenten, Moderation und Austausch zwischen Lehrkräften, wissenschaftlichen Mitarbeitern und Studenten)

## Studium



10/2012 - 02/2013	Stipendium des Fachbereich Chemie, Pharmazie und Geowissenschaften Johannes-Gutenberg-Universität Mainz
07/2011 - 10/2011 & 08/2012 - 10/2012	Wissenschaftliche Hilfskraft, Abteilung physikalische Chemie von Polymeren, Max-Planck Institute für Polymere, Mainz Forschungsschwerpunkt: Kolloide Systeme für die Kristallisation aus Flüssigphasen

## Schulbildung

09/1998 - 03/2007	Gymnasium Nieder-Olm Abschluss: <b>Allgemeine Hochschulreife</b>
-------------------	---

## Auslandsaufenthalte

### Forschungsreisen

10/2016 - 11/2016	European Radiation Synchrotron Center, Grenoble, Frankreich Forschungsschwerpunkt: Small-angle X-ray scattering der Keimbildung von C-S-H
06/2016	Diamond Light Source, Didcot, England Forschungsschwerpunkt: Kristallstrukturanalyse von amorphen, anorganischen Verbindungen
09/2015	University of York, England Forschungsschwerpunkt: Atmospheric scanning electron microscopy der Keimbildung von C-S-H

### Auslandssemester

10/2012 - 02/2013

